# Study of Near and Far Field Measurements for Underwater Ship Noise


Master's Thesis
Marine Measurement Systems
Acoustics
Department of Physics and Technology
University of Bergen

**Matias Helleve**

June 1, 2023

# Acknowledgements

I would like to express my gratitude to all those who have contributed to the successful completion of this collaborative project between the University of Bergen and Det Norske Veritas (DNV).

First and foremost, I would like to thank Assoc Prof. Audun Oppedal Pedersen from the Department of Physics and Technology for accepting me as a master student. I am grateful for his guidance, patience, and unwavering support throughout this journey. His open-door policy and encouraging words have been instrumental in shaping my research and writing my thesis.

I extend my appreciation to my co-supervisors, Tormod Gjestland and Øystein Solheim Pettersen from DNV, for their valuable insights and expertise in the field of underwater noise. Tormod Gjestland, I am grateful for your extensive knowledge and for sharing your insights into propeller cavitation. Your guidance has been valuable to this project. Øystein S. Pedersen, thank you for your prompt responses and willingness to engage in video calls whenever needed. Your support has been greatly appreciated.

I would also like to thank my fellow students for their camaraderie and for all the good memories. Thank you for inspiring me, providing entertainment, and being a source of knowledge throughout the past five years.

Finally, I would like to thank my family and friends for being my pillars of strength throughout this entire journey. Your unwavering support, encouragement, and care have meant a lot to me. To my family, thank you for always believing in me. To my friends, thank you for the cherished memories, laughter, and for standing by my side during both the highs and lows.

Matias Helleve
Bergen, 1.6.2023

# Abstract

The increasing noise levels in the ocean necessitate accurate methods for describing underwater radiated noise from ships. Typically, ship noise is measured using bottom mounted hydrophones to assess the noise generated by the ship itself passing a observation point. This thesis presents a new model to predict the underwater radiated noise, inspired by DNV's simplified method is based on near field measurements performed with transducers on the ships hull. Additionally, a study of far field measurements is included, followed by a comparison of different methods that are in use for measuring underwater radiated noise.

The methodology employed in this thesis focused on accurately processing the signals. It was observed that ideal signal processing techniques varied depending on the purpose, such as comparing single tonal components or analysing the overall sound field. The proposed model was developed to calculate sound propagation by considering factors such as sound absorption, spherical spreading, and the Lloyd mirror effect.

The far field hydrophone data analysis revealed its higher sensitivity to time variations compared to the near field pressure sensors measurements performed on the ship. In addition, a Doppler effect was discovered to be useful in determining the position of different sources and time synchronising. While on-ship measurements were made close to the propellers, the far-field hydrophone measurements showed noise from several other sources on the ship.

Neither the final proposed model nor the alternative methods presented offered complete one-to-one correspondence between far field hydrophone measurements and measurements taken on the ship.

These findings highlight challenges and complexities in accurately modelling and predicting underwater radiated noise from ships.

# Contents

# List of Figures

# Chapter 1

# Introduction

Sound in the Ocean plays a vital role in the ocean ecosystem, benefiting a significant portion of marine wildlife. For example, Cetaceans, Pinnipeds, and Sirenians depend on sound for communication and localisation. The relevant frequency domains span from 0.001 Hz up to around 100 kHz. Following the development from the industrial revolution, the ocean sound level has rapidly been increasing [4]. New technology and globalisation have increased international trade, thus increasing the shipping of goods. Shipping, seismic and new infrastructure are manufactured noise sources in the Ocean. These contributors emit noise in the same frequency domain as marine wildlife mentioned above [4]. According to J.Torunadre [5], the shipping industry has increased drastically in the last few decades, experiencing a fourfold increase only from the 1990s to 2014. Furthermore, ocean acidification caused by increasing atmospheric carbon dioxide levels, will decrease acoustic absorption for low frequencies [6], which again will increase the ship induced low frequencies noise propagation. This impacts marine wildlife in several ways. Finding mates, navigation, and avoiding predators are some of the reduced potentially negative impacts for marine species[4][7] [8]. There are also studies that show signs of avoidance and increased stress[9][10]. Some studies even discuss the possibility of physical harm in hearing and non-auditory tissues [11].
There are ongoing projects aiming to minimise the underwater sound pollution coming from the ships. In 2014, the International Maritime Organization released guidance for reducing noise from ships [12]. The European Union's Marine Strategy Framework also mandates the European Union to mitigate and monitor noise pollution [13]. Several ship classification societies have different methods to monitor underwater radiated noise (URN). ISO 17208-1 provides a standard for measuring underwater noise. However, many existing methods are cumbersome, and DNV (Det Norske Veritas) have proposed a near-field measurement with far-field propagation modelling to determine ship-emitted underwater noise (URN) inexpensively and practically. The following work explore the potential of a similar method of modelling far-field sound propagation with a hull-mounted pressure sensor directly above the ship propeller by comparing the propagation model with sea bottom-mounted hydrophone data. The project aims to create a far-field sound propagation model of sound emitted from a ship propeller. In addition, a thorough examination of the far field measurements is conducted. Furthermore, the already existing models will be compared and discussed.

# Chapter 2

# Theory

## 2.1 Underwater Noise

The following will first describe the different types of noise and how to characterise them. After that, different underwater acoustics will be explained, followed by a brief overview of existing URN measurement methods. There are multiple sources of underwater noise. This thesis covers ships as underwater radiated noise (URN) contributors, producing noise in the 10-10000 Hz domain [4]. The highest noise levels are usually between 5 Hz up tp 1 kHz [14]. Seismic background noise, surface agitation, and ice cracking also make URN in the same frequency domain [15]. Ships radiate noise from multiple noise sources. In this thessis the noise from one propeller is considered the primary noise source, but other structural and mechanical noise sources will also be relevant.

## 2.2 Fundamentals

A way of describing acoustic sources is by dividing them into monopoles, dipoles and quadrupoles. A monopole source is considered omnidirectional in this thesis. The radiation efficiency $\eta_{rad}$ is an important quantity in URN. It is described as *"...the ratio of acoustic power to the total power involved in the acoustic and hydrodynamic fluid motion"* [16] page 45. The radiation efficiency is defined as [16] page 45.

$$\eta_{rad} \sim \left(\frac{a}{\lambda}\right)^{2m+1} \sim (ka)^{2m+1}, \tag{2.1}$$

where $k$ is the wave number, $\lambda$ is the wavelength, $a$ is the source radius, and $m$ is the order of the pole. A monopole is of order 0, a dipole is one, and a quadrupole is 2. In other words, $\eta_{rad}$ in eq. 2.1 shows that a source has highest $\eta_{rad}$ for lower orders, since URN sources usually have small $ka$ numbers relative to unity

### 2.2.1 Cavitation

Cavitation is defined as a process where the liquid's static pressure is reduced to under the liquid's vapour points [17]. This boils the water by reducing the pressure instead of increasing the temperature. A phase transition diagram is shown in figure 2.1.

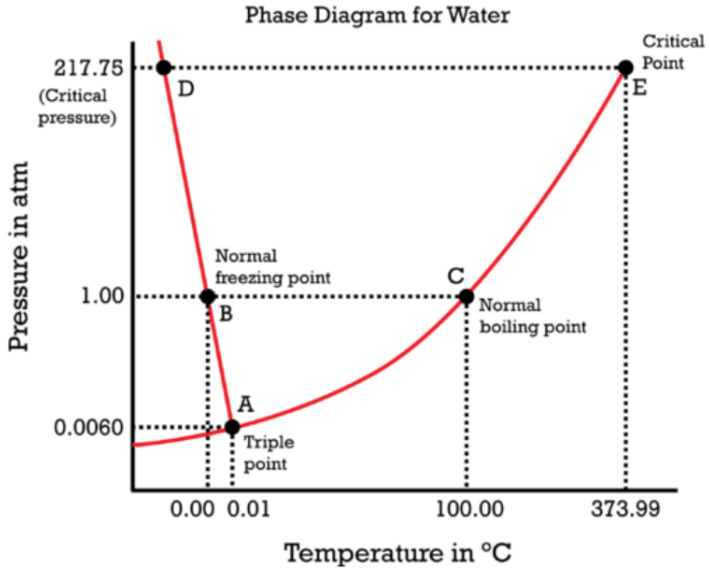


*Figure 2.1: Water Phase Transition Diagram taken from [1]. The area under the graphs is water vapour (gas), the area to the left is solid (ice), and the remaining area is liquid (water).*

Figure 2.1 illustrates the different temperature and pressure thresholds to make water transition between states, which is similar for salt water, and how the phase transitions are both temperature and pressure dependent. Marine propeller produces cavitation at certain rotations per minute (RPM), following Bernoulli's equation that state that an increase of velocity leads to a pressure decrease [17]. The pressure difference from the lift caused by the angle of attack and the fluid velocity past the blade section causes cavitation primarily on the suction side of the blade. When the bubbles from the cavitation collapse, it releases broadband noise [18]. This broadband noise is one of the main contributors to URN from ships..

A ship propeller produces mainly two types of cavitation, vortex cavitation and sheet cavitation on the blade surface. There are two types of sheet cavitation, and three for vortex cavitation. For vortex cavitation, there are tip-vortex, hub-vortex cavitation and leading edge vortex. For the blade surface, there is back and face surface cavitation [19].
Tip vortex cavitation is considered the main source of ship URN, even tough sheet cavitation normally results in the highest single peak pressure amplitudes. The single peak pressure amplitudes are lower for tip vortex cavitation, because the vortex cavitation voids are in the negative pressure area for longer, allowing vapour and gases to mix with the void, resulting in less sudden energy release [16].

By [20], blade surface cavitation is referred to as unsteady sheet cavity and can be treated as a monopole source. Further, given by the continuity equation and boundary conditions on the blade surface, there is also a macroscopic dipole. According to the boundary conditions, there is no flow passing through the blade surface (no transpiration velocity). To prevent the flow from penetrating the surface, an additional volume source is added at the leading edge. This source pushes the incoming flow away from the surface. At the trailing edge, negative velocities are present to seal the edge and prevent any leaks. As a result, there is a positive pressure at the leading edge and a negative pressure at the trailing edge, creating a "macroscopic dipole"[19]. A monopole source has no directivity, whilst a dipole has a directivity

[21]. Low-frequency noise from ship propellers is caused by the unsteady sheet cavitation and blade pressure fluctuations [20]. Remember that the sheet cavitation is considered a monopole, whereas the blade pressure fluctuations can be considered a dipole in close proximity. Further away, the blade dipole can also be considered as a monopole, because of the relative small distance between the poles. The sheet cavity collapses, produces high frequency noise [20].

The blade-pass frequency and multiples of this dominate tonal spectra of the cavitation. Usually, the strongest tonals range from 5 to 30 Hz depending on the ship type. Cruise ship's normally have a blade-pass frequency around 8 -15 Hz [19].

### 2.2.2 Magnetostriction

The internal realignment of the ferromagnetic domains due to the material being magnetised changes the materials dimension [16], is called Magnetostriction. The ferrite material used in a ship motor electromagnets is magnetostrictive. They grow in dimensions when exposed to a magnetic field, regardless of the field's orientation [22]. This dimensional change will happen in half a cycle of voltage, which makes the motor surface vibrate at twice the power-line frequency[16]. This vibration causes a noise called transformer hum.[16] The transformer hum radiates sound at harmonics of the power line, and if one of these hits a resonance to the casing of the motor, it will emit a strong sound. For a electromagnetic AC-motor, these frequencies will be at [16]

$$f = f_m \pm_0 2\tilde{f}, \tag{2.2}$$

Where f is the fundamental noise frequency from rotor slot noise, and

$$f_m = Rn \tag{2.3}$$

R is the number of electromagnets in the motor which [16] calls armature teeth. The n is rotation per second (RPS), $\pm_0$ is plus-minus and zero, and $\tilde{f}$ is the engines power line frequency. A electromagnetic DC-motor will vibrate depending on the both the product of R and n, but also the switching frequency. The switching frequency $f_{sw}$ is the rate at which a pulse-width-modulator (PWM) turns the voltage on and off. A PWM delivers a desired average voltage from a AC-current, by turning the voltage on and off. The average voltage depends on the duration of the duty cycles. The coils inside the PWM will vibrate at the

$$f = f_{sw} \pm_0 2\tilde{f} \tag{2.4}$$

A electromagnetic DC-motor will also emits tonals from the magnetostriction of the magnets inside the motor, given by $f_m$. The process for a electromagnetic DC-motor is shown in figure 2.2

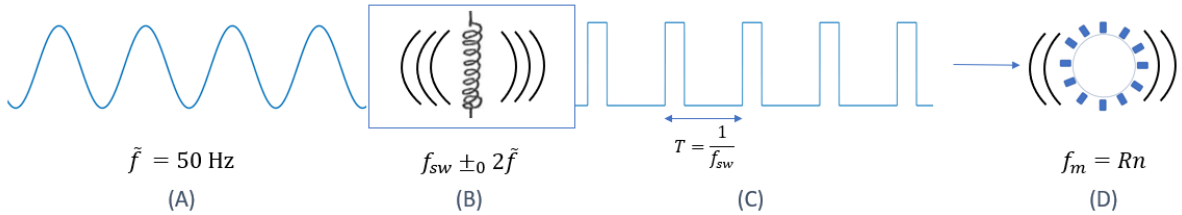


*Figure 2.2: (A) Power line frequency: This refers to the frequency of the alternating current (AC) power supplied to the electromotor. B) Coils in the Pulse Width Modulation (PWM): In a PWM-driven system, the coils within the PWM vibrate, emitting sound. (C) A rectangular pulse is utilised to provide an average direct current (DC) voltage to the electromotor. The duration between duty cycles, denoted as T, determines the switching frequency $f_{sw}$.(D) Magnetostriction-induced vibration: Magnets within the electromotor can vibrate due to magnetostriction.*

## 2.3 Lloyd's Mirror Effect

The Lloyd's Mirror effect is the name of the physical phenomenon of interference between two sound propagation's paths, namely direct and surface reflected. The simplest way of describing Lloyd's Mirror Effect is by a straightforward point source and one-point receiver. There is a deep water assumption for simplification, so only reflection from a flat sea surface is considered without considering the sea bottom. Further an assumption of straight ray tracing lines is applied. The concept is illustrated in 2.3.

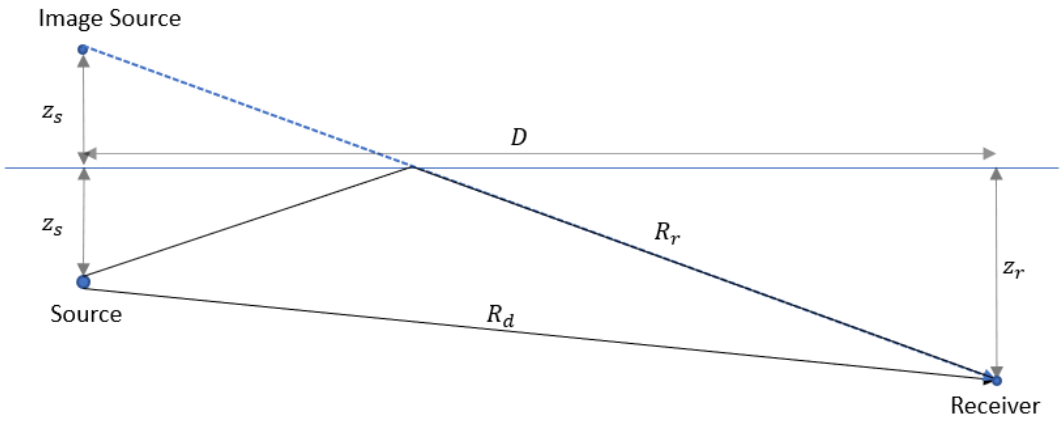


*Figure 2.3: Source, Mirror Source and Receiver with direct distance between Source and Receiver $R_d$, distance between the image source and the receiver $R_r$ and the horizontal distance between source and receiver D. The depths of the source and receiver are $z_s$ and $z_r$ respectfully.*

In this lossless, spherical case, the pressure $p_d$ from the direct path $R_d$ from the transmitter is given as [23]

$$p_d = \frac{p_0}{R_d} e^{j(\omega t - kR_d)}, \tag{2.5}$$

where $p_0$ is the pressure amplitude, $\omega$ is the angular frequency, $t$ is the time in seconds, and $k$ is the wavenumber. In this thesis, only $R_d$ will be known, which will equal the closest point of approach (CPA), which is described in 2.10. The remaining distances will be calculated

based on the CPA and calculated by Pythagoras theorem. There is also a reflected path $D_r$ where the spherical wave is reflected onto the point receiver from the sea surface. The ratio between the reflected pressure amplitude and incident pressure amplitude is defined, for the normal incident, as the reflection coefficient given as [23]

$$\mathbf{R} = \frac{\mathbf{P}_r}{\mathbf{P}_i} = \frac{\frac{r_2}{r_1} - 1}{\frac{r_2}{r_1} + 1}, \tag{2.6}$$

where the variables $r_1$ and $r_2$ are the specific acoustic impedance's for two fluids. The reflected wave's magnitude can be calculated using the following boundary conditions obtained from [24].

- Continuity of pressure, which means that there can be no net force separating the mediums on each side of the interface,

$$\mathbf{p}_\mathrm{i} + \mathbf{p}_\mathrm{r} = \mathbf{p}_\mathrm{t},\ x = 0, \tag{2.7}$$

  where x is a distance that implies the natural boundary between the two fluids.

- Continuity of the normal component of velocity is

$$\mathbf{u}_\mathrm{i} + \mathbf{u}_\mathrm{r} = \mathbf{u}_\mathrm{t},\ x = 0, \tag{2.8}$$

  where $\mathbf{u}_\mathrm{t}$, $\mathbf{u}_\mathrm{i}$ and $\mathbf{u}_\mathrm{r}$ is the complex total, incident and reflected normal particle velocity, respectfully.

As shown in Kinsler & Frey [24], the reflection coefficient $R$ as shown in 2.6 can be deducted from the boundary condition 2.7 and 2.8 to where r is the acoustic impedance of the medium. Fluid 1 is, in this case, seawater and fluid 2 is air. Since $r_2 << r_1$, equation 2.6 gives $R \approx -1$ and $T \approx 0$. The reflected wave will have the same phase shift of $\pi$ but maintain its amplitude. An imaginary source is introduced to describe the reflected wave and will be similar to equation 2.5 with a phase shift of $\pi$, given as

$$p_r = -\frac{p_0}{R_r} e^{j(\omega t - kR_r)}. \tag{2.9}$$

The distance $R_r$ is defined as

$$R_r = \sqrt{D^2 + (z_r + z_s)^2}, \tag{2.10}$$

which is the reflected wave path length, calculated using the Pythagorean theorem with D as the horizontal path between the source at depth $z_s$ and the receiver at depth $r_s$. The total pressure amplitude at the receiver is then given as the sum of 2.5 and 2.9, given as 2.11 in Lurton [25] .

$$\mathbf{p} = \frac{\mathbf{p}_0}{R_d} e^{j(\omega t - kR_d)} [1 - e^{-jk\frac{2z_r z_s}{D}}] \tag{2.11}$$

Equation 2.11 only describes a case where the seabed can be ignored. By including the seabed, multiple paths will arrive at the point source.
In this case, the total sound pressure will be the sum of an infinite number of propagation paths, described by Lurton [25]

$$\mathbf{p}(t) = \sum_{i=1}^{\infty} \sum_{j=1}^{4} \mathbf{p}_{ji}(t). \tag{2.12}$$

The phase difference between the reflected wave and the direct wave depends on the frequency and distance. In equation 2.5, it is observed that the phase difference is determined by the product of the wave number $k$ and the distance $R$. For relatively small frequencies and distances, the phase shift will be minimal because the wave number is much smaller than the distance $k << R$. In order to achieve destructive interference between the reflected and direct waves, the phase shift of the reflected wave needs to be at least $\frac{\pi}{2}$. Figure 2.4 plotted with LLoydexample.m in Appendix A, illustrates the phase difference between the waves propagated along the direct path and the surface-reflected path. This particular example considers a reflected distance $R_r$ of 139 m, while the direct distance is 132 m $R_d$.

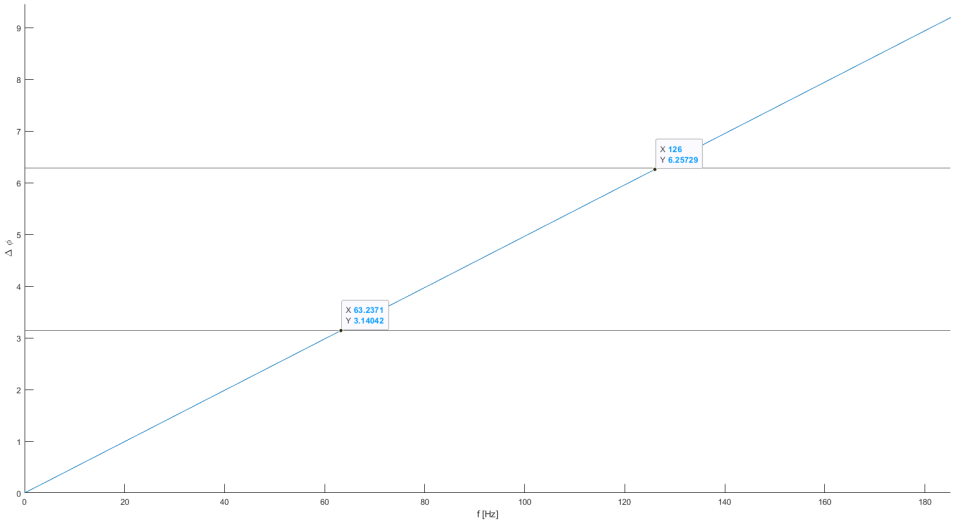


*Figure 2.4: Phase difference $\Delta\phi$ with respect to frequency. The direct distance $R_d$ 132 m, the source is at a depth of 5 m, and the receiver is at a depth of 40 m. The reflected distance is $R_r$ 139 m.*

Across figure 2.4, there are two lines, marking $\pi$ and $2\pi$. The prediction is that the frequencies with a phase shift

$$\Delta\phi = 2n\pi \ , \ n \ \in \mathbb{N} \tag{2.13}$$

will be where there is maximum destructive interference. Figure 2.5 shows the frequency of the expected first destructive Lloyd interference, calculated with Lloydexample.m in appendix A.

The first predicted minimum will be around 126 Hz according to figure 2.5. A moving source will change how the LLoyd mirror effect appears at the position of an observer, while recording an acoustic signal of a finite period of time. To showcase this, a lossless signal s with 1000 samples, $f_s$ of 24800 Hz, frequency of 2500 Hz, and sound speed $c$ of 1500 m/s is considered. The source is considered to be a moving ship, with a velocity of 5 m/s . The ship is moving in a straight line, with a stationary receiver at a depth of 40 m. The source is assumed to be at a depth of 5 m. A CPA of 132 m is used. The distance between the source and receiver will result from the Pythagorean theorem for the horizontal distance and then the depth distance. The horizontal distance changes while the ship moves in a straight line for 82 s, covering a distance of 410 m. The velocity is constant, so the horizontal distance development is linear, and the direct distance with depth included is non-linear. The resulting plot is in figure 2.6 with Lloydeffectdistvar.m in Appendix A.

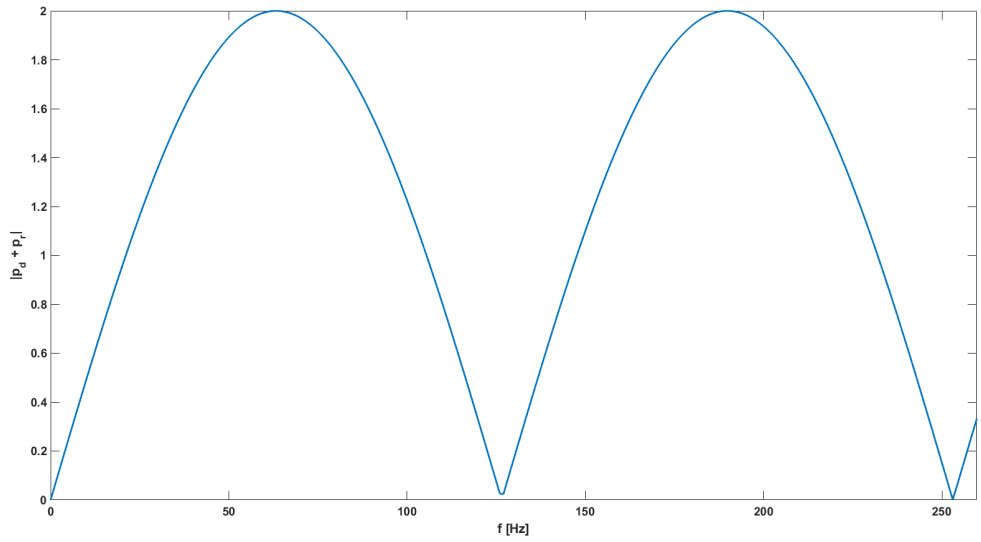


*Figure 2.5: Expected LLoyd Effect for a direct distance $R_d$ 132 m, the source is at a depth of 5 m, and the receiver is at a depth of 40 m. The reflected distance is $R_r$ 139 m.*

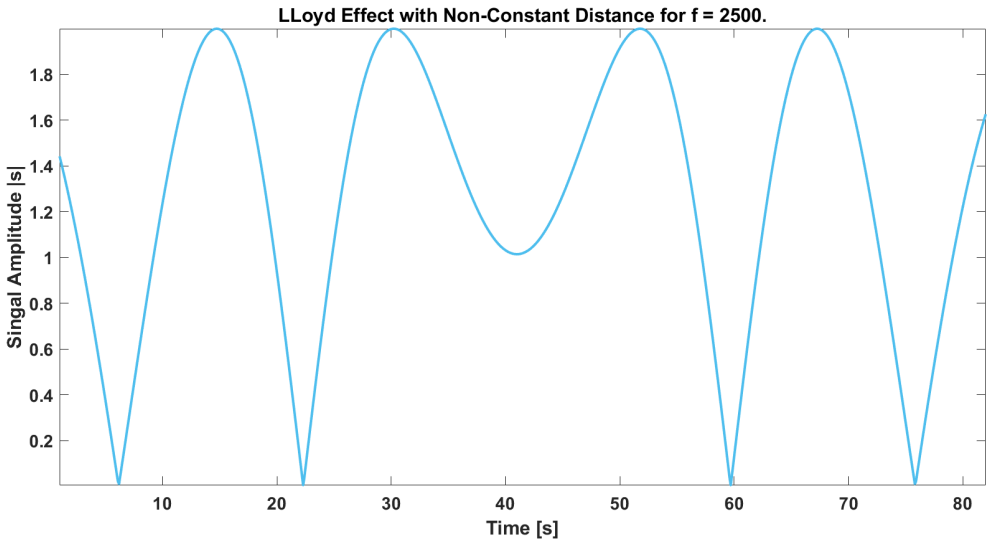


*Figure 2.6: Signal amplitude $|s|$ time development for $f = 2500$ Hz,*

As seen in figure 2.6, the Lloyd mirror effect will not only be different for different frequencies, but will also change for different distances.

## 2.4 Spherical Loss

Two spherical surfaces, $S_1$ and $S_2$ , with different radius, $r_1$ and $r_2$, and monopole sound source located in the centre of the circle, is illustrated in figure 2.7.
The intensity $I$ is defined as

$$I = \frac{\Pi}{A}, \tag{2.14}$$

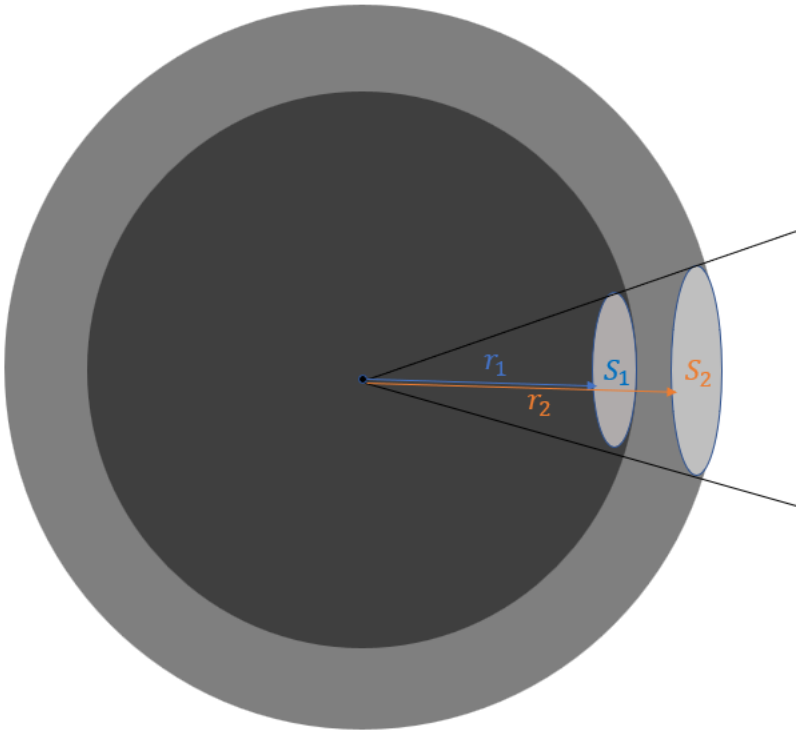


*Figure 2.7: Two surfaces $S_1$ and $S_2$ with sound source in the middle. $r_1$ and $r_2$ is the distance from the sound source to the respective surfaces.*

where $\Pi$ is the power and A is the area. The total power radiating through two surfaces in figure 2.7 at constant radii form a source is invariant with respect to radius but the intensity is inversely proportional to the radius squared caused by the area ratios. If the areas of the spheres are defined as $S_1$ and $S_2$, the resulting power relation is described by

$$\Pi = I_1 S_1 = I_2 S_2. \tag{2.15}$$

The relative intensity, i.e. the intensity loss, is

$$\frac{I_1}{I_2} = \frac{S_2}{S_1} = \frac{4\pi r_2^2}{4\pi r_1^2} = \frac{r_2^2}{r_1^2}, \tag{2.16}$$

where $r_1$ and $r_2$ are the sphere radius, respectfully. Thus, the intensity of an outward-propagating lossless spherical wave is proportional to $\frac{1}{r^2}$. The spherical transmission loss is described in equation 2.17

$$\mathrm{TL} = 20\log_{10}\frac{r}{r_0} \tag{2.17}$$

In the following, the reference value of $r_0$ = 1 m will be used.

## 2.5 Backtracking

The propeller is constantly rotating, experiencing a load fluctuation around a revolution and even a propeller in uniform flow has a rather complex set of acoustic modes in the near field. The dipole resulting from the non-cavitating effects, the pressure from sheet cavitation, the

interference between the pressure emitted by the individual blades as well as the oscillating tip vortices among other sources is incomprehensibly complex. Therefore, to simplify, a monopole source is assumed, and the source level SL is estimated from the pressure sensor at the boat's hull. By assuming a monopole, the SL can be assumed by

$$\mathrm{SPL} = \mathrm{SL} - \mathrm{TL} \rightarrow \mathrm{SL} = \mathrm{SPL} + \mathrm{TL}, \tag{2.18}$$

where the SPL is the sound pressure level and TL is the transmission loss. Only spherical loss is included in the transmission loss for simplification. The absorption is assumed to be neglected between the source and the pressure sensor. The distance $r_{\mathrm{dc}}$ is used to calculate the TL with eq. 2.17. The distance $r_{\mathrm{DC}}$ is the distance between the flush mounted pressure sensor and the tip of the nearest propeller when at top dead centre and is shown in figure 3.2. Then by using the measure data from the hull pressure sensor as the SPL, then calculate TL based on the above distance assumption, the SL can be estimated.

## 2.6 Sound Velocity

The speed of sound is a function of salinity, pressure and temperature. In other words, the sound speed,c, is location dependent. An approximation of Leroy's [26] equation of the speed of sound in sea waters is given as [24]

$$\begin{aligned} c(T,S,P) = 1449.08 + 4.57Te^{-\frac{T}{86.9}+\frac{T}{360}^2} + 1.33(S-35)e^{\frac{-T}{120}} \\ + 0.1522Pe^{\frac{T}{1200}+\frac{S-35}{400}} + 1.46\times 10^{-5}P^2e^{-\frac{T}{20}+\frac{S-35}{10}}. \end{aligned} \tag{2.19}$$

The speed of sound is, in other words, dependent on the temperature, salinity and pressure. $T$ is the temperature measured in degrees Celsius, $S$ is the salinity in units of part per thousand (ppt) and $P$ is the gauge pressure in atmospheres. The pressure $P$ is gives as [24]

$$P = 99.5(1 - 0.00263\cos 2\phi)Z + 0.239Z^2, \tag{2.20}$$

where $\phi$ is the latitude and Z is the depth in kilometres. A common way of measuring ocean characteristics is by performing for example conductivity, temperature and density (CTD) measurements in situ. One of the goal of this thesis ,however, is to simplify the measurement procedure. Therefore instead of depending CTD-measurement, a constant speed profile is assumed based on GPS and weather data.. To account for inaccuracy for the constant speed profile, a threshold based on a high and low constant sound speed will be shown in Appendix C. Furthermore, a constant sound speed profile simplifies the Lloyd mirror effect calculation by allowing straight ray tracing lines.

## 2.7 Sound Absorption

When sound travels through a medium, it experiences absorption. This is because some acoustic wave energy is converted into thermal energy. According to [24] there are three mechanics that drive the absorption.

- Chemical Relaxation
- Viscosity

- Thermal Conduction

This absorption is included in equation 2.5 as a negative contribution $\gamma$ in

$$p(x,t) = p_0 e^{-\gamma x} e^{j(\omega t - kx)}. \tag{2.21}$$

The units for $\gamma$ are Neper pr. meter. This equivalent dB per meter value is $\alpha$ and is described as

$$\alpha = 20\log_{10} e^{\gamma} \approx 8.686\gamma. \tag{2.22}$$

The general form for $\gamma$ is given as [27]

$$\gamma = C_1 \frac{f_1 f^2}{f_1^2 + f_2^2} + C_2 \frac{f_2 f^2}{f_2^2 + f^2} + C_3 f^2. \tag{2.23}$$

The first and second terms of 2.23 accounts for the chemical relaxation due to boric acid $B(OH)_3$ and magnesium sulphate $MgSO_4$, which are salts. The last part accounts for the viscosity. The model for $\alpha$ chosen in this thesis is Francois & Garrison [27]. It is clear from the model that absorption is frequency-dependent, but also salinity, temperature and depth are important factors. As conducting a CTD measurement is impractical, the medium is assumed to be homogeneous, and the ocean characteristics are estimated based on GPS coordinates and date, as described in Section 2.6.

## 2.8 Sensors in a Baffle

The measurement done close to the propeller is done by a broad band pressure sensor. The pressure sensor is flush mounted in the hull. Therefore it can be approximated by a hydrophone in a rigid baffle. What one measures while using a rigid baffled hydrophone is the sum of the incident pressure wave and the reflected pressure wave, as described in [24]

$$\mathbf{p}_\mathrm{t} = \mathbf{p_i} + \mathbf{p_r}, \tag{2.24}$$

where $\mathbf{p}_\mathrm{t}$, $\mathbf{p}_\mathrm{i}$ and $\mathbf{p}_\mathrm{r}$ is the complex total, incident and reflected pressure wave.
From using equation 2.6, the total pressure wave can be defined as

$$\mathbf{p}_\mathrm{tot} = \mathbf{p}_\mathrm{i} + \mathbf{R}\mathbf{p}_\mathrm{i}. \tag{2.25}$$

For perfect reflection the, where **R** = 1, the total pressure becomes

$$\mathbf{p}_\mathrm{tot} = 2\mathbf{p_i}. \tag{2.26}$$

## 2.9 Doppler Shift

The harmonic wave function 2.5 is a function of distance. In a stationary case, the distance $D$ is considered stationary. By a non-stationary case, the distance is a function of time $D(t)$ and the speed $v_r$ relative to the direct distance component given as [23]

$$D = D(t) = D_0 + v_r t, \tag{2.27}$$

where $t$ is the time, and $v_r$ is the change direct distance , relative to time $t$ between source and receiver.
By inserting 2.27 into 2.5, an expression of the perceived frequency for the receiver is given as [23]

$$\mathbf{p}_r(D(t),t) = \mathbf{p}_0 e^{j(\omega_0 t - k(D_0 - v_r t))} = \mathbf{p}_0 e^{j((\omega_0 + \Delta\omega)t - kD_0)}. \tag{2.28}$$

The attenuation is not included here, and there is an assumption that the wave is a simple plane wave. The frequency shift can then be calculated as [23]

$$\Delta\omega = kv_r = \omega_0 \cdot \frac{v_r}{c}. \tag{2.29}$$

## 2.10 Existing Vessel URN Methods

There are many different methods of measuring the underwater radiated noise (URN). In the following, the URN be used as the sound pressure level (SPL) at the closest point of approach between the source and receiver,

$$\text{URN} = \text{SPL}(\text{CPA}) \tag{2.30}$$

This section will cover some of these, mainly based on ship classification societies, together with an independent research project. The definitions of the different symbols are different from each other. In this section, to stay true to the source, the originals symbols are used. At the end of this section, a summary table is shown in 2.10.6.

### 2.10.1 ISO 17208-1

ISO 17208-1 is a standard for measuring URN from ships and quantities. It includes smoothing of the curve with an Lloyd mirror effect but does not include absorption and bottom-surface reflections. The reason why it does not include sea bottom reflection is that a deep water assumption. This standard requires three hydrophones with an upper-frequency range of at least 20000 Hz and four runs in total. A run describes a measured passing of the ship. The distance between the ship and the hydrophone is defined as the closest point of approach (CPA). The CPA is the horizontal distance between the ship and a reference point. This applies to both surface hydrophones and sea-bottom mounted hydrophones. The distance between the ship and hydrophone $d_{total}$ is corrected with the Pythagoras theorem. Another requirement is that the ocean depth shall exceed 150 m or 1.5 times the ship distances, decided by which length is longer.
The sea surface condition shall be as calm as possible since rough sea induces broadband background noise (BGN) and makes the measurement conditions unstable. A wind speed limitation of $\leq 20$ knots $\approx 5$ in Beaufort scale given in Appendix C in [28], for ships longer than 100 m is defined. Ships with a lesser length than 100 m should have a calmer sea to prevent a situation where the propulsion breaks the sea surface, which causes instability. The background noise is corrected for if the difference between the signal-plus-noise and the noise $\Delta L$, is between 3-10 dB, where $\Delta L$ is

$$\Delta L = L_{p_{s+n}} - L_{p_n} = 10\log_{10}\left(\frac{p_{s+n}^2}{p_n^2}\right), \tag{2.31}$$

where $L_{p_{s+n}}$ is the RMS SPL measured during test in decibels, $L_{p_n}$ is the RMS SPL without ship precent. BGN adjusted RMS SPL $L'_p$ during the test is defined as

$$L'_p = 10\log_{10}\left[10^{\frac{L_{p_{s+n}}}{10\text{dB}}} - 10^{\frac{L_{p_n}}{10\text{dB}}}\right]. \tag{2.32}$$

If the background noise is less than 3 dB, the measurments are noted or discarded. $L'_p$ is then adjusted to the unweighted RMS after BGN adjustment, $L''_p$ by

$$L''_p = L'_p + A_{\text{SEN}}, \tag{2.33}$$

where $A_{SEN}$ is an adjustment for hydrophone characteristics like sensitivity. The URN for each hydrophone $L_{RN}$ is distance corrected with geometrical spreading by

$$L_{RN}(r,h) = L''_p + 20\log_{10}\left(\frac{d_{\text{Total}}}{d_{\text{ref}}}\right)\text{dB}, \tag{2.34}$$

where r is the run number, h is the hydrophone location, and $d_{ref}$ is the reference distance of 1 m. The average power per hydrophone are then averaged as

$$L_{RN}(r) = 10\log_{10}\left[\frac{10^{\frac{L_{RN}(r,h_1)}{10\text{dB}}} + 10^{\frac{L_{RN}(r,h_2)}{10\text{dB}}} + 10^{\frac{L_{RN}(r,h_3)}{10\text{dB}}}}{3}\right]\text{dB} \tag{2.35}$$

and the total URN is the average of the power-averaged underwater radiated noise $L_{RN}(r)$ for every run.

$$L_{\text{RN}} = \frac{\sum_{r=1}^{r=k} L_{\text{RN}(r)}}{k}, \tag{2.36}$$

where k is the total number of runs. $L_{RN}$ is then used to calculate source level $L_s$ by using

$$L_{\text{s}} = L_{\text{RN}} + \Delta L, \tag{2.37}$$

where $\Delta L + 20\log_{10} CPA$ is the difference between the URN and the source level. $\Delta L$ is the Lloyd mirror effect, called dipole source correction in ISO 17208-1. By assuming that the source depth $d_s << r_1$ and $d_s << r_2$, where $r_1$ is monopole source distance and $r_2$ is mirror monopole source distance, a fitted solution for the correction factor $\Delta L$ is described in terms of a rational function, by

$$\Delta L = -10\log_{10}\left(\frac{2(kd_s)^4 + 14(kd_s)^2}{(kd_s)^4 + 2(kd_s)^2 + 14}\right)\text{dB}, \tag{2.38}$$

where $d_s$ is the source depth.

### 2.10.2 DNV Silent Class Notation

A full description of DNV's Silent Class can be found in [2]. DNV divides between deep water (>150 ) and shallow water (30-150 m) testing. The deep water testing follows the ISO 17208-1 and uses $18\log_{10}(\frac{r}{r_{1m}})$ as a transmission loss factor.
The shallow water testing is based on a single bottom-mounted hydrophone. The CPA should be 100-200 m. The minimum depth under the vessel keel is 30 m or the draught length thrice. The distance used for distance correction should be assumed to be the CPA the whole time.

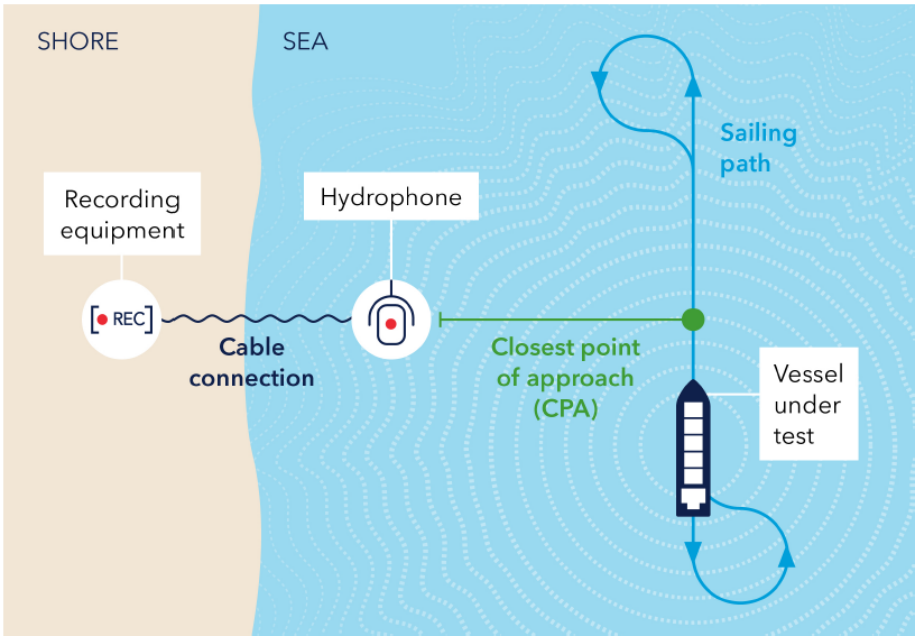


*Figure 2.8: Schematic for DNV's Silent Class notation measurement procedure taken from [2]*

The ship passes two full ship lengths. An illustrative figure is shown in Figure 2.8. This figure is taken from [2] with permission.
The shallow water method uses either + $18\log_{10}(\frac{r}{r_0})$ or actual measured transmission loss in addition to a - 5 dB sea bottom reflection factor. Two sets of measurements should always be taken under free sailing conditions. The power of these measurements is average to basis to establish the noise.

DNV also includes a simplified measurement approach. This method is the origin of the proposed solution presented in this thesis. It is based on hull mounted pressure sensor directly above the propeller. An illustration is shown in figure 2.9 is taken [2] with permission

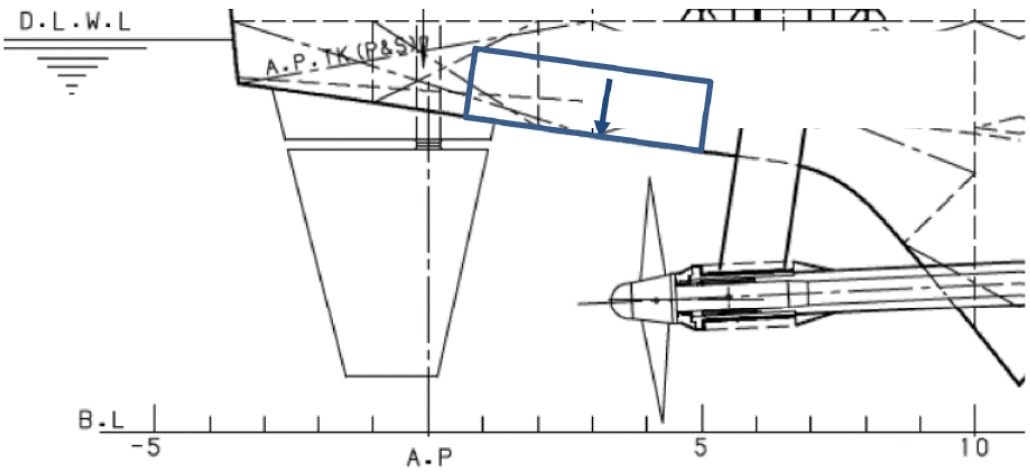


*Figure 2.9: Preffered DNV placement of pressure sensor, indicated with blue arrow taken from [2]*

The pressure sensor data $L_p$ models the far-field sound propagation. $L_p$ is considered as the source level. The far field is modelled by assuming a point source located at the propeller tip

of the nearest propeller when at top dead centre . With an assumed monopole, DNV corrects for spherical spreading with a distance correction $C_d$ of

$$C_d = 20\log_{10}(\frac{r}{r_{1m}}), \tag{2.39}$$

where r is the distance from the point source to the receiver, and $r_{1m}$ is the reference distance. A pressure reflection correction of -6 dB because of the effect of having a sensor in a baffle as described in 2.8. Furthermore, a Lloyd mirror correction factor is added to adjust for interference between surface-reflected and direct wave. The Lloyd correction factor is defined as

$$C_r = \begin{cases} 29 \text{ dB} - 16 \times \log_{10}(f) & \text{for } f \leq 100 \text{ Hz} \\ -3 \text{ dB} & \text{for } f > 100 \text{ Hz}. \end{cases} \tag{2.40}$$

$C_r$ is estimated by using a nominal length of a 100 m and a source depth of 5 m as a basis for the Lloyd mirror effect. DNV describes the radiated noise levels $L_{RN}$ as

$$L_{RN} = L_p + C_d - C_r - 6 \text{ dB}. \tag{2.41}$$

and is a radiated noise prediction. This method is only allowed for ships where the prominent noise is assumed to be from cavitation and engine noise in the lower frequency domains. As for the deep and shallow water, the data is presented in a 1/3 octave band. The data shall be supplemented with measured narrow band data, for information. Eq. 2.41 is applied pr octave band.

### 2.10.3 Bureau Veritas Underwater Radiated Noise

Bureau Veritas(BV) provides a method that covers deep and shallow water. The method is described in [29], and the following are based on BV rules [29]. A monopole source is assumed, and the source level is estimate by TL from a measured value to a reference distance of 1 m. This method only cares about continuous noise from vessels. The assessment instrumentation includes three omnidirectional hydrophones. Beforehand a single frequency component is used to calibrate the acoustic measurement system. The difference between shallow and deep water assessment is that for deep water, the hydrophones are floating and for shallow water assessment, the hydrophones are anchored to the sea bottom. BV's model differs from other methods because it is rather extensive. It includes live distance measurement, multiple hydrophones, parabolic wave equation, sound speed profile and ray tracing. The underwater corrected sound pressure level for propagation is

$$L_s(r_k, w_k, h_i) = L'_s(r_k, w_k, h_i) + TL[D_H(r_k, w_k, h_i), D_v(r_k, w_k, h_i)] \tag{2.42}$$

where $L'_s$ is the calibrated source level, TL is BV's defined transmission loss, $r_k$ is the run number, $h_i$ is the specific hydrophone, $D_H$ is the horizontal distance between the reference acoustical source and hydrophone, $D_V$ is the vertical distance from the source to the hydrophones, and $w_j$ is the data window j . The data window is the time signal that the spectrum is calculated from.

BV also proposes a more straightforward method when the extensive one is impossible, with a stated stated accuracy decrease of 0.5 dB, as stated in [29]. The spherical loss is divided into

$$TL[D(r_k, w_k, h_i)] = \begin{cases} 19\log_{10}[D(r_k, w_k, h_i)] & \text{for water depth} < 100 \text{ m} \\ 20\log_{10}[D(r_k, w_k, h_i)] & \text{for water depth} \geq 100 \text{ m}, \end{cases} \tag{2.43}$$

D is the distance between the reference acoustical source and hydrophone, and $w_j$ is the data window j [29]. The acoustic reference centre is between the main engines and the propeller and is 2/3 of the distance from the keel to the sea level. The only exception is for specially designed ships. The corrected source level $L_s(r_k, w_k, h_i)$ is backtracked with assume TL to

$$L_s(r_k, w_k, h_i) = L'_s(r_k, w_j, h_i) + TL[D((r_k, w_k, h_i))]. \tag{2.44}$$

All the hydrophones receive different signals. The measured average source level is average over the hydrophones as the following,

$$L_s(r_k, w_j) = 10\log_{10}\left(\frac{1}{3}\sum_{h_i=1}^{3} 10^{\frac{L_s((r_k, w_k, h_i))}{10}}\right) \tag{2.45}$$

Further, $L_s(r_k, w_k, h_i)$ is linearly averaged for all the windows $w_j$, described in 4.6.1 in [29] and then a linear average of all runs described in 4.7.1 in [29]. Finally, the power spectral density is defined as 1/3-octave bands.

### 2.10.4 The Hydropod

Hydropod is the name of a similar approach as this thesis proposed method. It is a "*on-board deployed acoustic-visual device for propeller cavitation and noise investigations*" [30]. This method uses a foil applied from the ship hull and behind the propeller. With a similar trial approach as DNV Silent Class, with a ship passing a hydrophone multiple times, the Hydropod pro compares their propagation model with actual far-field measurements. Background noise is accounted for with [30]

$$L'_p = 10\log\left(10^{(\frac{L_{p+n}}{10})} - 10^{\frac{L_n}{10}}\right), \tag{2.46}$$

where $L'_p$ is the BGN corrected SPL, $L_{p+n}$ is the measured SPL during, and $L_n$ is the ambient BGN. This method only uses spherical loss for spherical spreading from a monopole source with [30]

$$L_{s(r)} = L'_p + 20\log(\frac{d_{Total}}{d_{ref}}) = L'_p + TL_{HP}, \tag{2.47}$$

where $L_{s(r)}$ is the estimated propagated SPL in dB @ 1 m, $d_{\text{total}}$ is the distance between the assumed acoustical centre at the propeller and the hydrophone, and $d_{\text{ref}}$ is the reference distance 1 m.

### 2.10.5 Proposed Model

One of the primary challenges associated with existing underwater radiated noise (URN) measurements is that they tend to be either overly comprehensive or lacking in precision. In order to address this issue, the proposed model aims to achieve both precision and ease of execution. The method is based on DNV's simplified method using a hull mounted pressure sensors.
The assumed pressure wave is described in 2.11. This wave description pertains to a monochromatic wave with a constant sound velocity. Additionally, the measured pressure

is assumed to be the sum of various pressure waves. Although these assumptions do not hold true for a "real" stochastic signal, they are utilised to facilitate the calculation of frequency-dependent mechanics.
The transmission loss TL is assumed to arise from spherical spreading from a monopole source, absorption, and the Lloyd mirror effect. The spherical spreading is described in 2.7, absorption is described in 2.7, and the Lloyd mirror effect is outlined in 2.3.
DNV 2.41 and BV 2.45 simplified models incorporate the Lloyd mirror effect by utilising nominal distances to approximate flat correction factors for specific frequency or depth ranges. In contrast, this model includes the calculated Lloyd mirror effect using an assumed mirror surface. The mirror surface assumption is considered valid for Beaufort scale $\leq 4$.
A comprehensive description of both surface and bottom-reflected waves, calculated using 2.12, is extensive and necessitates a description of the seabed. However, since the hydrophone is positioned on a sloped seabed, sea bottom reflection is assumed to be negligible. The sound pressure is calculated by

$$p = \frac{p_0}{R_d} e^{-\gamma R_d} e^{-i(-kR_d)} - \frac{p_0}{R_r} e^{-\gamma R_r} e^{-i(-kR_r)}, \tag{2.48}$$

where $p_0$ is the backtracked amplitude from the hull mounted pressure sensors signal. The resulting URN will then be

$$\text{URN} = \text{SPL}(R_d) = 20 \log_{10} \text{p in dB re } \mu\text{Pa} \tag{2.49}$$

### 2.10.6 Summary of the Different Methods

As mentioned in the introduction to this section, a summary table is presented in table 2.10.6.

*Table 2.1: Overview of Different Methods Discussed in Section 2.10*

| Parameter | ISO-170208 | DNV Silent - E | DNV Silent - E (Simplified) | BV URN | Hydropod | Proposed Model |
|---|---|---|---|---|---|---|
| **Amount of Hydrophones** | 3 | 1 | Hull Mounted (1-3) | 3 | Stern Mounted (1) | Hull Mounted (1-3) |
| **Closest Point of Approach (CPA)** | 100 m or one overall ship length, whichever is the greater | 100-200 m | NA | Longer than 200 m, 400 m and 500 m. (100 m) | NA | NA |
| **Acoustic centre of vessel (Based on CPA)** | Located transversely at the ship centreline, longitudinally a quarter-length forward of the stern and vertically at the height of the sea surface. | transversely at the ship centerline, longitudinally a quarter-length forward of the stern and vertically at the height of the sea surface | Propeller Tip | Halfway between engine and propeller longitudinal, 2/3 of vessel draught from water line | The hub of the subject propeller | Ship Propeller. |
| **Spherical Distance Correction and Lloyd Mirror Correction (TL)** | 20 log r + $\Delta L$ | 18 log r | 20 log r + $C_r$ | 19 logr/20log r | 20 log r | 20 log r + Lloyd mirror correction + Absorption |

# Chapter 3

# Measurement Setup and Methods

This chapter provides a detailed description of the measurement setup and methods employed in this study. Section 3.1 outlines the measurement setup and the equipment. Subsequently, Section 3.2 describes the signal processing techniques employed in this thesis.

## 3.1 Measurement Setup

Figure 3.1 shows a figure of the complete setup, supplied by [2] with permission. This thesis will utilise the terms "near field" and "far field" to describe the sound field in different regions. It is important to note that all transducers in this study are positioned in the far field relative to the sound source. However, in this thesis, the near field term will specifically refer to the sound field in close proximity to the ship, while the far field term will describe the sound field located at a considerable distance, relative to near field distances, from the source. The main difference between the fields is that the measurement in the near field do not need account for long distance propagation mechanisms like the Lloyd mirror effect and absorption, as opposed to the far field, where these mechanisms are important.
The data is collected by a hydrophone, 50 m deep and 50 meters off the coast. From there, the ship passes with constant speed. The ship moves in a straight line, with stationary a stationary hydrophone, as seen in figure 2.8. It passes three times, with the first 80 % maximum continuous rating and 11 knots. At the same time, the near field is measured by three hull-mounted pressure sensors. Two of these are directly mounted over the ship propeller as illustrated in 3.1. The ship itself is 205 m long. Table 3.1 is an overview of the equipment used.

*Table 3.1: Near Field Instrumentation*

| Instrumentation | Manufacturer | Model | Serial Number | Sensitivity |
|---|---|---|---|---|
| Pressure sensor ($P_1$) | Kistler | 601CA | 5673501 | 7.341 [mV/kPa] |
| Pressure sensor ($P_2$) | Kistler | 601CA | 5673502 | 7.341[mV/kPa] |
| Pressure sensor ($P_3$) | PCB Piezotronics | ICP | 18129 | 43.51[mV/kPa] |
| Noise Sensor | Norsonic | Nor150 | - | - |
| Hydrophone | Ocean Sonics | TC4059-1 | 3319022 | -178.8 [dB V re $\mu$Pa] |
| Computer | - | - | - | - |

The measurement was done 5.nov 2021 in the coastal areas of western Norway. According to [31], the sea temperature outside the city of Ålesund, located at the coast of western Norway, was on average 11°C. A salinity approximation of 33.11 ppt, based on average coastal salinity

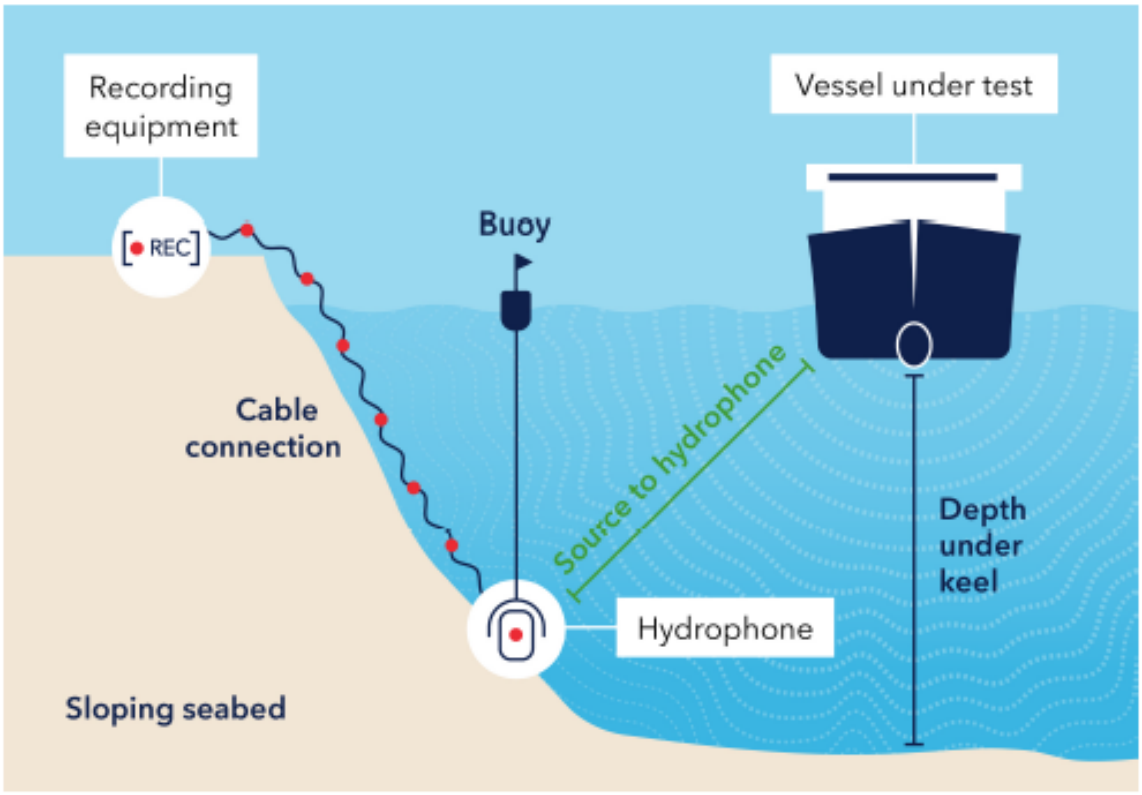


*Figure 3.1: Measurement Setup. The figure is supplied from [2]*

measurement in Hardangerfjorden in 8.sept 2017 displayed at page 86 in [32]. By inserting this into 2.19, the speed of sound is calculated, by using SpeedOfSound.m in Appendix A

$$c_{d=50\text{m}} = 1.4918 \cdot 10^3 \text{ m/s} \tag{3.1}$$

for a depth of 50 m, and

$$c_{d=5\text{m}} = 1.4911 \cdot 10^3 \text{ m/s} \tag{3.2}$$

for a depth of 5 m.

### 3.1.1 Near Field

The setup in the near field is shown in 3.2.
The instrumentation used in the near field, is shown in table 3.1. For $P_1$ and $P_2$, the calibration sheet can be found in [33]. The sensitivity of these sensors is

$$M_{P_1 \& P_2} = 7.341 \frac{\text{mV}}{\text{kPa}} \tag{3.3}$$

For $P_3$, the calibration sheet can be found in [34], where the sensitivity can be found to be

$$M_{P_3} = 43.51 \frac{\text{mV}}{\text{kPa}} \tag{3.4}$$

A pressure sensor is connected to a analog-to-digital converter (ADC) connected to a computer through a cable. This data is acquired as a wav-file. The propeller makes the near-field

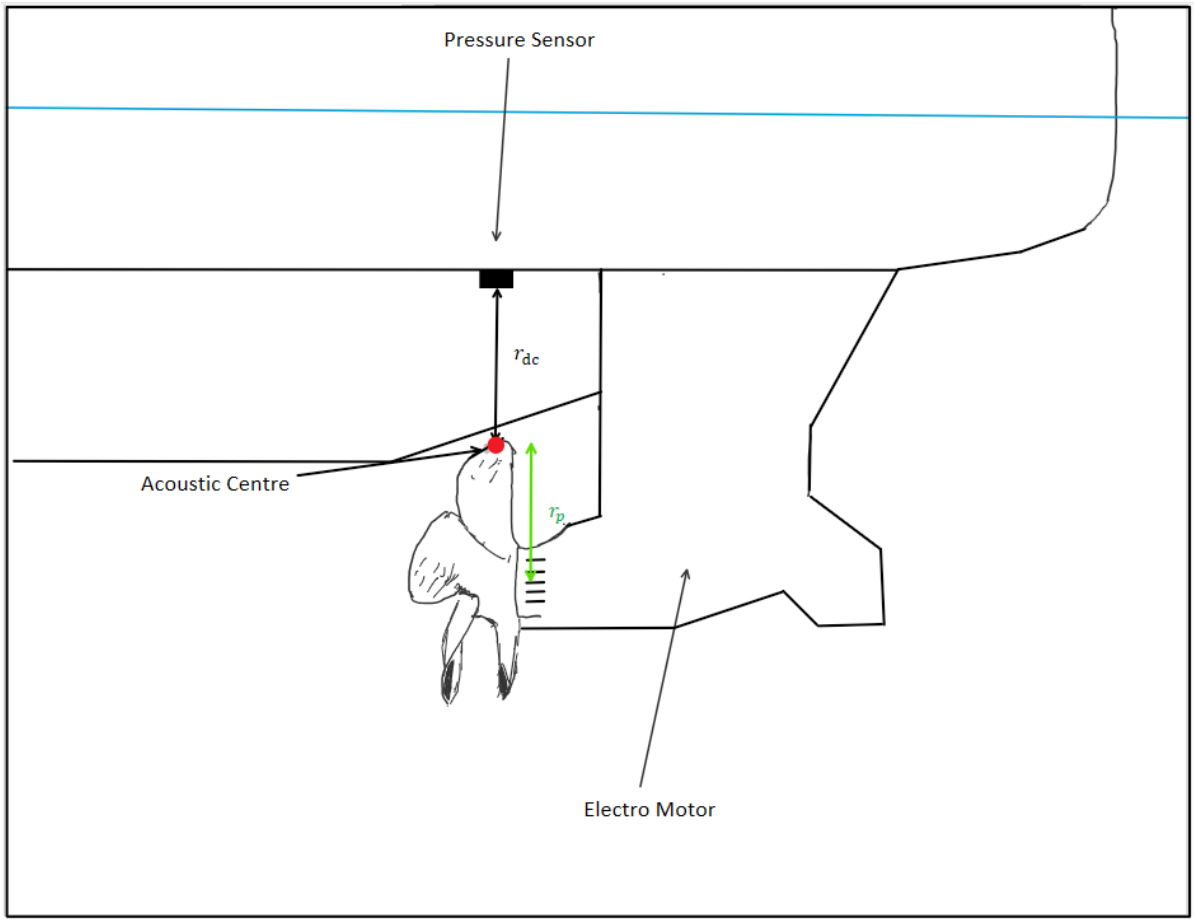


*Figure 3.2: Near Field Setup*

measurement complex. Due to multiple propeller blades, the sound field calculation is extensive and expensive. In addition, all of the blades produce cavitation. Therefore a simplification of a monopole source is used in this thesis. In the far field, the monopole source approximation is accurate[19]. The propeller diameter is 3.9 m. The propeller centre is approximately 4 m. The approximate distance between the ship propeller tip and the pressure sensor $r_{dc}$ is 1.206 m. The distance $r_{dc}$ is used for the distance correction described in section 2.18.

### 3.1.2 Far Field

The far-field setup consists of a sea bed-mounted hydrophone. The measurement was done by DNV officials and is described thoroughly in DNV's rules for classification [2]. The hydrophone is mounted in a cage, similar to one shown in figure 3.3 taken with permission [2] In figure 3.4 the sensitivity for hydrophone is plotted.
As seen in figure 3.3 and figure 3.4 the hydrophone could be sensitive to the direction of the hydrophone. Therefore it must be noted, that for higher frequencies, the directive of the hydrophone or the source could affect the results. However, because of long wave lengths for low frequencies, compared to the hydrophone dimensions, the hydrophone will interpret low frequencies sound waves, as a pressure which changes at almost the same time surrounding the hydrophone, which means that the hydrophone can be considered omnidirectional for low frequencies.

*Figure 3.3: Hydrophone mounted to a cage, taken from [2].*

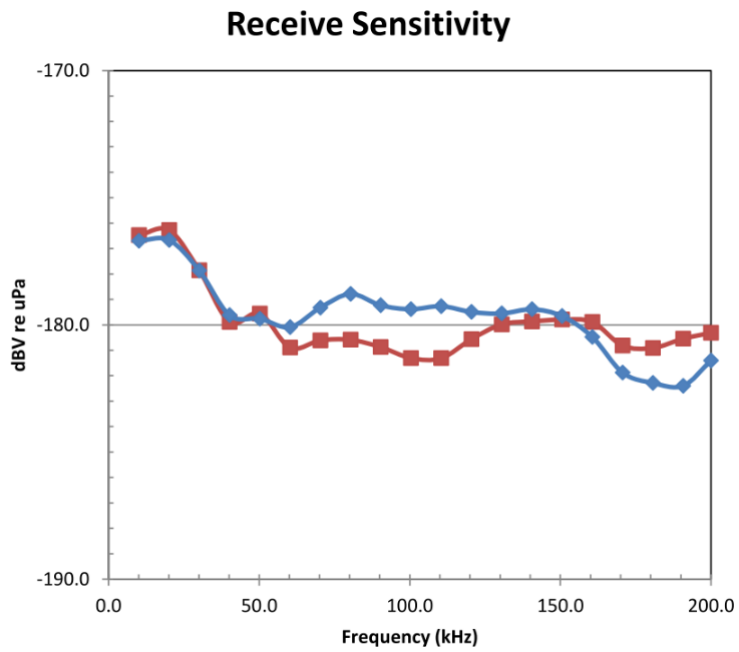


*Figure 3.4: Hydrophone Sensitivity taken from [3], where the red graph shows for 0 °and red graphs shows for 90 °*

The seabed is sloped to minimise bottom reflections. Further, the ship minimised thruster use because thrusters are not used in regular operation. The weather is assumed to have calm conditions (below Beaufort 4). This is needed to apply a perfect sea surface reflection approximation. The closest point of approach (CPA) is measured with GPS distance between the observer and ship, adjusted for the distance between the observer and the hydrophone. Hydrophone and recording equipment are connected through a cable. The recording equipment is situated with the observer.

Prior to conducting the measurements for various runs, the background noise (BGN) is mea-

sured. The BGN has an impact on the recorded signals, but no correction is applied. Instead, the BGN is plotted alongside the first 1/3- octave band comparison to assess its magnitude.

### 3.1.3 The Data

The data was given as wav-files. A wav-file is an audio file for storing digital audio on a PC. The voltage was converted to pressure by using the open circuit voltage response (OCVR), which gives the free field receiver sensitivity $M_{vp}$ shown as

$$OCVR = 20\log_{10}\frac{M_{vp}}{1\frac{V}{\mu Pa}}. \tag{3.5}$$

Then, using $M_{vp}$, the voltage is converted to pressure values by eq. 3.6 as described in [35].

$$p_n = \frac{V_n}{M_{vp}} = \frac{V[n]}{1\frac{V}{\mu Pa}10^{\frac{OCVR}{20}}}. \tag{3.6}$$

The near field pressure sensor data is gathered with Norsonic 150. This will include an flat wav-correction factor $C_{wav}$ of 111.3 dB. The $C_{wav}$ is needed because of the way the Nor150 stores wav-files. Furthermore, because of the baffle effect on the hull-mounted transducer, as described in the theory section 2.26, will give a contribution of 6 dB. This is accounted for with a -6 dB correction factor. The formula for the dB sound pressure values for the near field sensor is given as

$$\mathrm{SPL_n} = 20\log_{10}\frac{p_n}{1\mu\mathrm{Pa}} + C_{wav} \tag{3.7}$$

The OCVR value for the far field hydrophone are given in the calibration sheet [3]. OCVR values are frequency dependent. The difference between the OCVR , a constant OCVR value is assumed sufficient for the frequency range 0 - 24000 Hz. The calibration sheet [3] gives a constant value of

$$\mathrm{OCVR_{HYD}} = -178.8 \pm 2.5 \ \text{dBV re } \mu\text{Pa} \tag{3.8}$$

Both the pressure sensor and the hydrophone began measurements when the ship bow passed the CPA and recorded until the ship had passed and the stern passed the CPA. Ideally, the pressure signal and hydrophones was synchronised and the time length was the same. This would be ideal because then one could easily compare source and receiver, for example, by using only the time signals where the assumed acoustical centre of the ship is closest to the hydrophone, i.e. near the middle of both the time signals. Then the CPA would be an accurate measurement of the distance, which again could be used for precise Lloyd mirror effect calculations. An overview of the length of the time signals for different runs and sensors is displayed in table 3.2. Sensors P1, P2 and P3 are three different flush mounted pressure sensors, and the hydrophone is the far field hydrophone.
The signal's time lengths are not the same, which makes the time stamp independent of each other and cannot be used to compare the receivers, since they are not synchronised.

## 3.2 Methods

The data has been processed in multiple ways. Generally, one can use the built-in MATLAB-function fft.m to do a fast Fourier transform, which returns the two-sided discrete Fourier

*Table 3.2: Overview of Length of Time Signals [S]*

| Run | Hydrophone [s] | P1 [s] | P2 [s] | P3[s] |
|---|---|---|---|---|
| 8 | 56.000 | 43.652 | 52.603 | 59.107 |
| 9 | 85.000 | 54.903 | 56.053 | 54.653 |
| 10 | 41.000 | 55.103 | 60.304 | 58.353 |
| 11 | 57.000 | 56.903 | 57.560 | 48.954 |

transform (DFT). The fft.m applies the fast Fourier transform to a discrete signal [36]. The range of the frequency spectrum is $\frac{f_s}{2}$, and the resolution $\Delta f$ is given as

$$\Delta f = \frac{f_s}{N}, \tag{3.9}$$

where $f_s$ is the sampling frequency, and N is the total amount of samples. To get a higher frequency resolution, it is possible to zero pad the signal, with a computational expense as a trade-off. The hydrophone sample frequency is $f_{sf} = 256000$, and the near field sample frequency is $f_{sn} = 48000$. Applying fft.m to these two signals returns the frequency spectrum with different frequency bands and resolutions if the time length differs. This is not ideal for single component frequency comparison since the number of samples is different. The DFT points would then be different, the resolution would be arbitrary, which would make amplitude comparison meaningless. To prevent the Fourier spectrum to be sample rate dependent, a discrete-time Fourier transform is designed. The MATLAB-code DTFT.m in appendix A applies the discrete-time Fourier transform. A discrete time Fourier transform is defined in eq. 3.10.

$$S(f) = \sum_{n=-\infty}^{\infty} x(n)e^{j2\pi fn} \tag{3.10}$$

The difference between a DTFT and DFT is that the DTFT return a continuous frequency output from a discrete-time input, while the DFT returns a discrete frequency output. In other words, the DTFT has infinite resolution, but the DFT resolution depends on the number of samples and sampling frequency.

### 3.2.1 Windowing

A window is a signal processing tool. Perhaps best explained with the use of a constructed sinusoid. The first concept is windowing. A sinusoid consists of an amplitude A, a time t, a frequency $f_1$, and a phase $\phi$, shown in eq. 3.11.

$$s(t) = A\sin 2\pi f_1 t + \phi \tag{3.11}$$

For simplicity, the phase $\phi$ = 0 in the following. Signal s(t) must be discrete for a PC to handle the signal eq. 3.12.

$$s(t) = A\sin 2\pi f_1 nT \tag{3.12}$$

T is the sampling period, and n is the sample number. The total length of the signal is $N$. The variable n is all the natural numbers less or equal to $N$.

$$n \in \mathbb{N},\ n \leq N \tag{3.13}$$

The constructed signal will have frequency $f_1$ = 2000 Hz and amplitude A = 1. The sampling frequency is decided to be 4000 Hz.

$$f_s = 4000 \text{ Hz} \tag{3.14}$$

to avoid aliasing, following the Nyquist rate [37]. What causes spectral smearing is that the fft interpret a signal to only contain perfect multiples of the frequency periods to deal with the infinitely long definition of Fourier transform. The definition holds if the signal repeats itself, so during a fft, only a part of the actual signal is captured and then repeated [38]. Real life signal are not periodic which will result in high broad band frequency component's. Figure 3.5 showcases the non periodic effects, by first having only the first 140 samples of s(n) plotted in the upper figure, and then repeated by itself four times. The MATLAB script spectralsmearing.m in Appendix A is utilised to generate the corresponding plot.

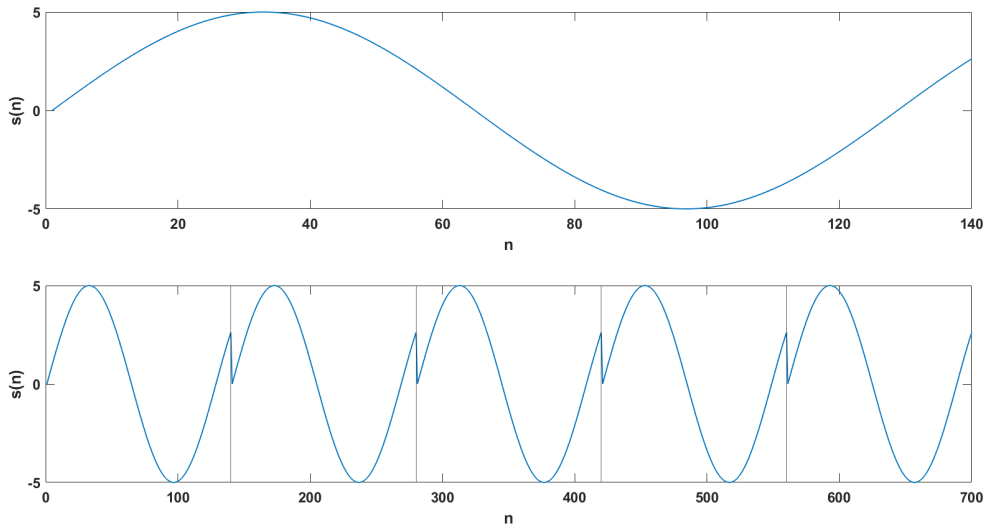


*Figure 3.5: The first 140 samples of s(n) plotted in the upper figure, and then repeated by itself four times in the lower figure.*

Spectral smearing makes the central frequency leak out to side lobes of the sinc- function, being the Fourier transform of a rectangular envelope [39]. This could potentially lead small amplitudes to be buried in the side lobes of a more significant frequency amplitude. One way to deal with this is by applying a window to the signal. By nature, a signal divided by a time limit is subject to a rectangular window, the simplest form of a window. The resulting frequency response of a rectangular window is shown in figure 3.6. The sudden cracks in Figure 3.5 is what causes spectral smearing. The result of using the fft and thus using a rectangular window, is shown in 3.6.
Sperctral smearing can be seen in the frequency amplitude response shown in figure 3.6. A way to lower the side lobes, is by introducing a Hanning window, which is a window with broad applications [39]. The Hanning window minimises the amplitude at the conjunction points, which is what causes the spectral smearing, shown in figure 3.7.
The Hanning window is described in eq. 3.15 and applied to the signal in figure 3.8. It greatly reduces the side lobes but makes the main lobe twice as wide as the rectangular window [40].

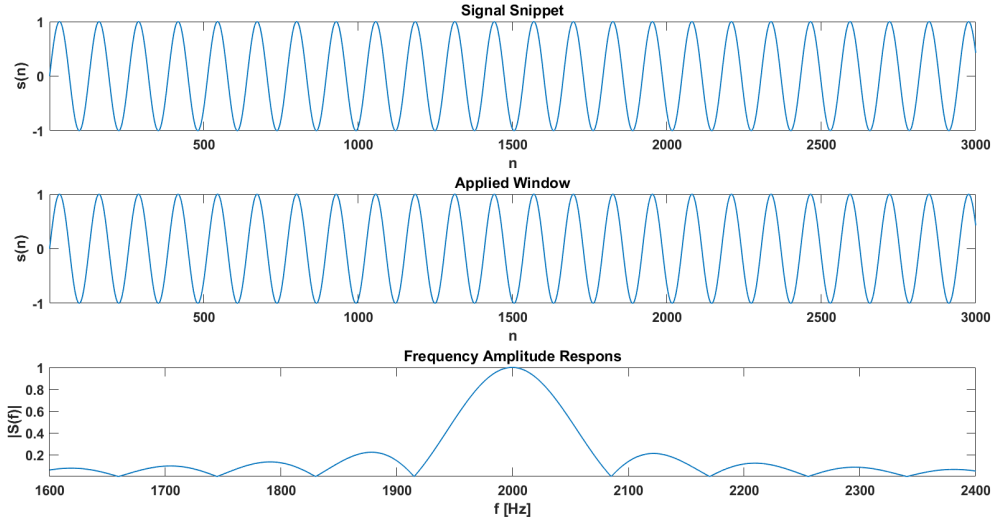


*Figure 3.6: Rectangular Window*

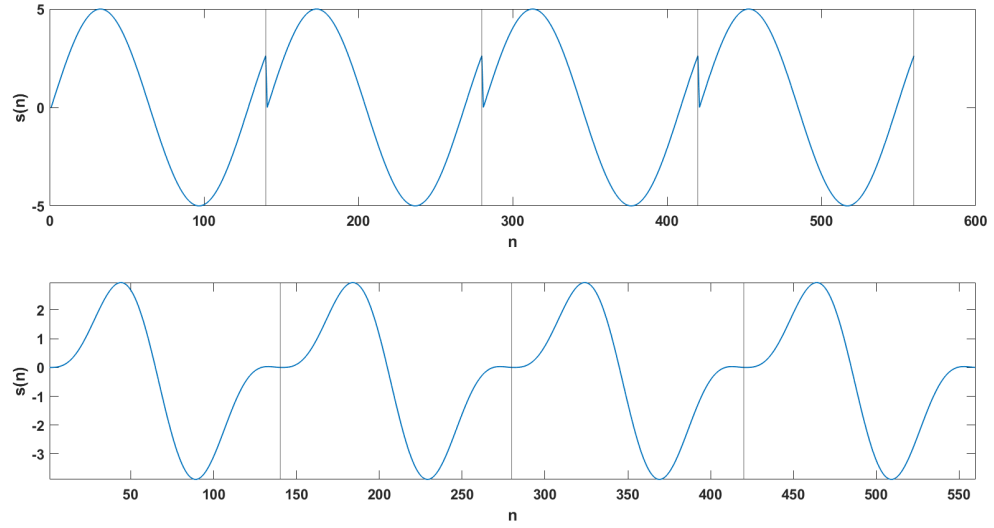


*Figure 3.7: Effect of Windowing*

$$w(t) = \begin{cases} 0.5 + 0.5\cos\frac{\pi t}{\tau} & \text{if } |t| \leq \tau \\ 0 & \text{elsewhere} \end{cases} \tag{3.15}$$

Where $t$ is the time, and $\tau$ is the length of the window.
By adding a Hanning window, the side lobes are decreased as seen in figure 3.8. One can increase the number of samples to obtain a narrower main love and a high-frequency resolution is achieved.

Another problem with using a window function is that it lowers the amplitude if the time series does not contain an integer number of cycles according to [41]. In nature, a integer number of cycles , an amplitude loss is inevitable, as shown in 3.5. As suggested in [42][43], an approximate correction factor of 2 at the amplitude leads to a correct amplitude. Furthermore,

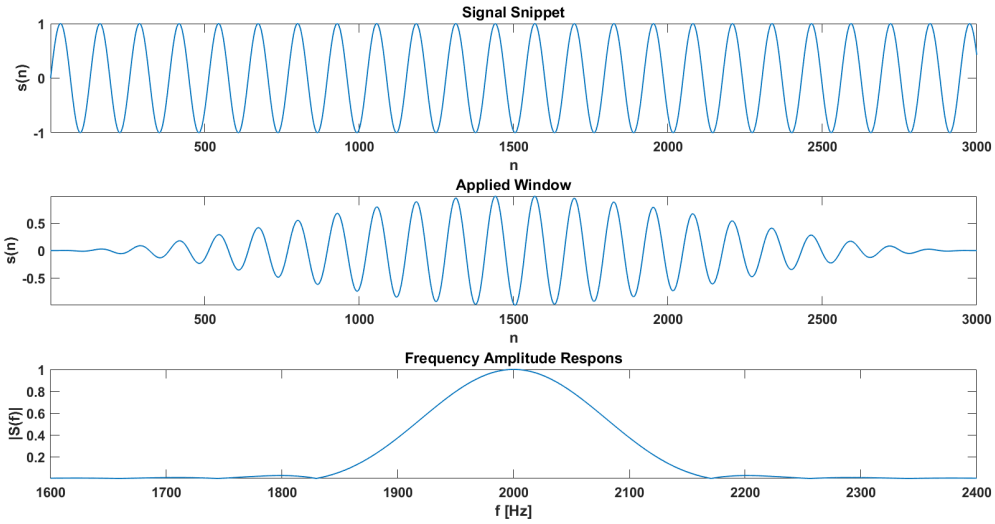


*Figure 3.8: Applied Hanning Window*

the window function also decrease the inherent signal energy. The window lowers some of the values, which leads to an energy loss.
The energy is defined as the integral of the squared signal as in eq. 3.16.

$$E_s = \int_{-\infty}^{\infty} |x(t)|^2 dt \tag{3.16}$$

The Hanning window is multiplied with the signal $x(t)$, in the time domain. The Hanning window function $w \leq 1$, which means that the time signal experiences an apparent energy loss as seen in eq. 3.16, since some of the signal $x(t)$ magnitudes are decreased. Therefore, to get precise amplitude or energy in the frequency domain, correction factor is needed, as explained in section 3.2.3.

### 3.2.2 Time Development

The Fourier Spectrum does not give any info on the time development of the signal. The frequency-time development is essential for precisely modelling the sound far field propagation. This is done by dividing the signal into shorter snippets and applying the signal processing to the different signal parts. Afterwards, the frequency amplitudes are plotted with respect to time and frequency. To illustrate the signal processing, another sinusoid is added to the signal in eq. 3.11, as shown in eq. 3.12. The amplitude to the second sinusoid is B = 2, and the frequency is $f_2 = 2200$ Hz.

$$s_n = \begin{cases} A\sin 2\pi f_1 nT + B\sin 2\pi f_2 nT & \text{if } \frac{\mathrm{N}}{2} \leq n \leq \mathrm{N} \\ A\sin 2\pi f_1 nT & n \leq N \text{ else} \end{cases} \tag{3.17}$$

Now $N$= 1 000 000, and the signal is divided into 30 parts. One of the snippets processing is illustrated in figure 3.9, where $|s(f)|$ is the frequency amplitude of signal s, calculated and plotted by MATLAB script SpectogramDTFT in Appendix A.
The frequency-time development is shown in the spectrogram in figure 3.10
As seen, the spectrogram correctly shows the time development and amplitude. In this example, the number of samples included in each part of the signal $n$ is the total amount of samples

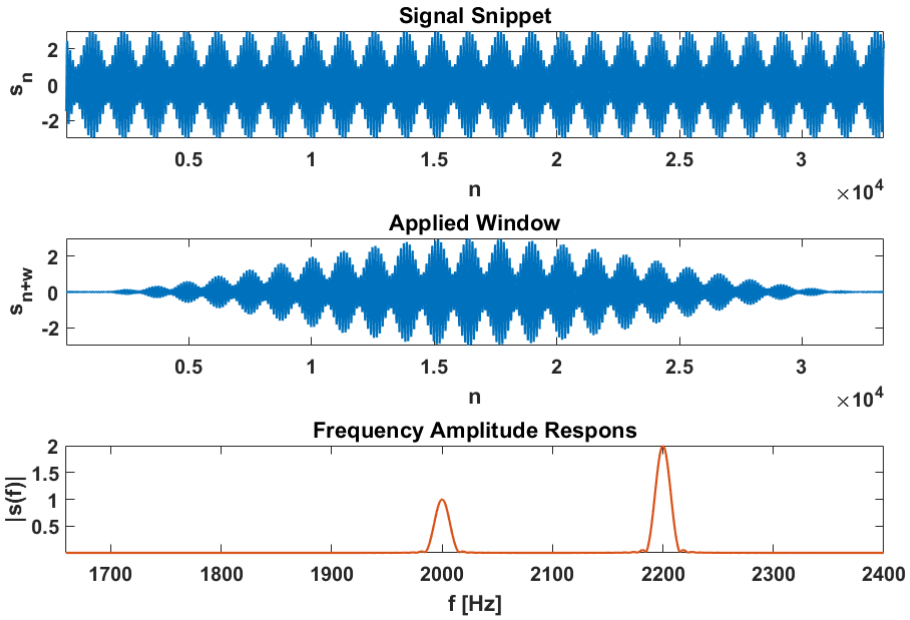


*Figure 3.9: Processing of Signal Snippet*

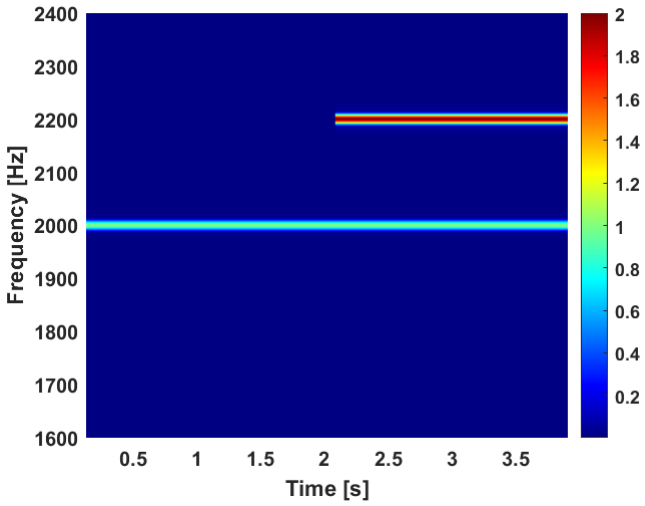


*Figure 3.10: Spectogram of Signal*

N divided by 30 snippet,

$$n = \frac{N}{30} = \frac{10^6}{30} = 3.33 \cdot 10^4, \tag{3.18}$$

which equals a time length t of

$$t = \frac{n}{f_s} = \frac{3.33 \cdot 10^4}{256000 \text{ Hz}} \approx 0.13s, \tag{3.19}$$

calcualted by The limitations of the time resolution lie in how many periods of a certain frequency are included in the signal snippet. This is shown by adding a new sinusoid with a $f_3$ = 5 Hz and amplitude C = 3 as described, as

$$s(t) = A\sin 2\pi f_1 nT + B\sin 2\pi f_2 nT + C\sin 2\pi f_3 nT. \tag{3.20}$$

The signal is now divided into 50 snippets. Figure 3.11 illustrates the resulting processing and spectrogram.

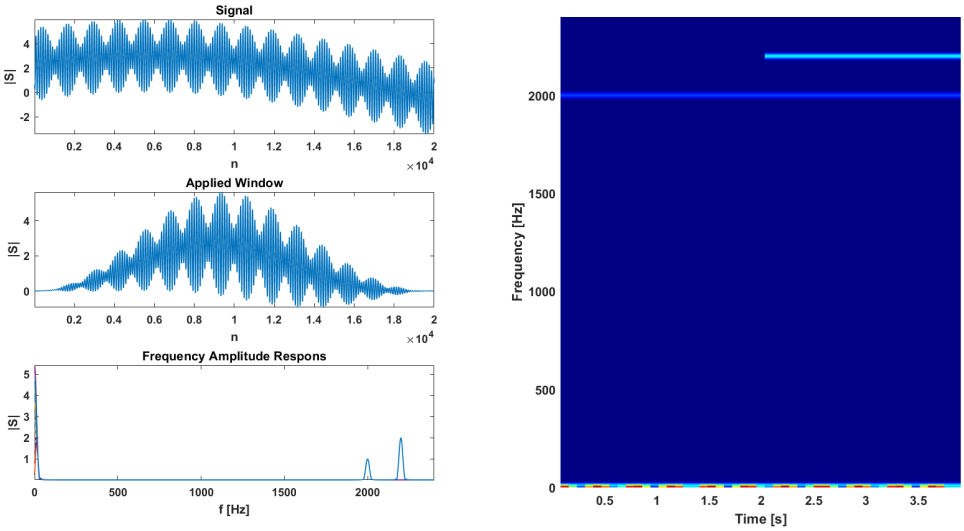


*Figure 3.11: DTFT and Spectogram*

By zooming in on the spectrogram around 2000 Hz and 5 Hz, the problem is apparent, shown in figure 3.12.

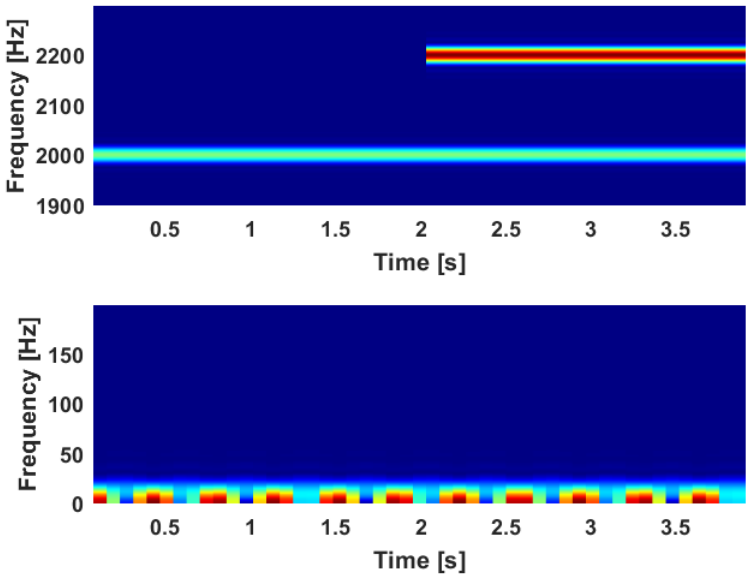


*Figure 3.12: Zoomed in Spectogram*

The 2000 Hz and 2200 Hz are constant, unlike the 5 Hz. The reason for this is that by dividing 1 000 000 sample signal into 50 snippets, the length of the snippets equals N = 20000, which equals approximately 0.08 s. The period of a 2000 Hz frequency is T = 0.0005 s, and the period of the 5 Hz frequency is 0.2 s. This means that in the 0.08 s-long snippets, there is not even a single period of the 5 Hz frequency. For the DTFT to give out a correct frequency, it needs at least one period of the frequency. The resulting DTFT makes the 5 Hz act like a

time-varying DC component. This can be seen in the top-left picture in figure 3.11, where the mid-line of the signal could be interpreted to be moved to 2 Hz. The mid-line frequency is usually the DC-component of a signal. However, the signal used in this test do not have any DC-component. A DC component like this would wrongfully result in high amplitude frequency components for low frequencies in a Fourier spectrum.

MATLAB also has a built-in function for making a spectrogram called spectrogram.m. This uses the DFT, which poses the same problems as the fft.m described in section 3.2. Therefore the pcolor.m function was used instead to plot the DTFT.m outputs, with respect to time and frequency.

### 3.2.3 Power Spectrum Density and Power Spectrum

There are several ways to present the result of a Fourier transform. The two ways this thesis covers are the power spectrum density (PSD) and power spectrum. The Fourier transform of a signal is defined as

$$S(f) = \mathcal{F}\{s(t)\}. \tag{3.21}$$

The power spectrum is defined as

$$P(f) = S_{\text{rms}}^2 = \frac{|S(f)|^2}{2}, \tag{3.22}$$

where $P(f)$ is the frequency dependent power and $S_{\text{rms}}$ is the rms-value of $|S(f)|$. The RMS value is only defined as this for sinusoids. The signals covered in this thesis are stochastic, so they contain no pure sinusoids. The following assumes that this is not the case and that the real signal comprises pure sinusoids. The power spectrum measures how much power each frequency component has.

The PSD, on the other hand, measures how much power there is pr frequency band,

$$\Pi_{band} = \int_{\Delta f} S_{PSD}(f)\, df = \int_{\Delta f} \frac{P(f)}{\Delta f}\, df, \tag{3.23}$$

where $\Delta f$ is $S(f)$ frequency resolution defined by

$$\Delta f = \frac{f_s}{N}, \tag{3.24}$$

where $f_s$ is the sampling frequency, and N is the number of samples in $s(t)$. The power spectrum will be used for narrow frequency bands or single frequency component analysis, where the PSD will be used for comparison. To showcase the importance of the difference between the power spectrum and PSD, the basic signal $s(t)$ from 3.12 with added Gaussian noise $n(t)$, defined as

$$s(t) = s(t) + n(t), \tag{3.25}$$

is used. The amplitudes of the two sinusoids in 3.12 are now A = 2 and B = 3, and the frequencies are now $f_1 = 2000$ Hz and $f_2 = 2006$ Hz. In figure 3.13, the Fourier amplitude $|S(f)|$ and the PSD are plotted for three signals. One of the signals has a number of samples n = $10^5$, one has n = $10^6$, and the last has n = $30^6$.

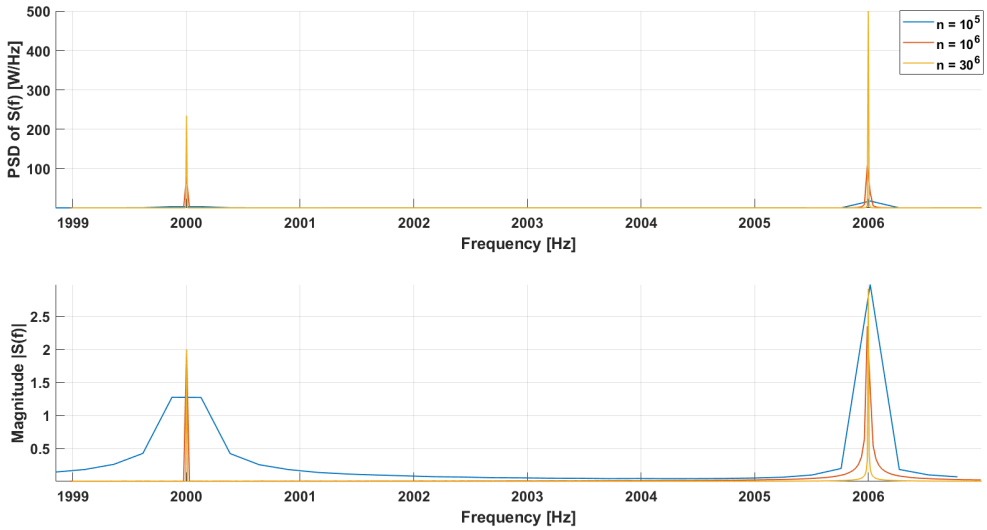


*Figure 3.13: Comparison of the power spectrum and PSD for signal s(t) with different signal lengths.*

As one can see, the length of the signal does not affect the amplitude in the power spectrum but the amplitude in the PSD. The signal processing is confirmed by using the Parsavels theorem. Parseval's theorem states that the energy is the same whether it is integrated over time or frequency 3.26.

$$\int_{-\infty}^{\infty} |x(t)|^2 dt = \int_{-\infty}^{\infty} |x(\omega)|^2 d\omega \tag{3.26}$$

Parasvel is defined by signal energy and thus holds for a stationary process's power. Using energy does not make sense since an infinite time sequence defines it. The power of a signal $\Pi$ in the time domain can be defined as the sum of all the instantaneous powers

$$\Pi_t = \lim_{N\to\infty} \frac{1}{N} \sum_{n=0}^{N} |s(n)|^2. \tag{3.27}$$

The power in the frequency domain was calculated by transforming eq. 3.23 into its discrete version

$$\Pi_f = \sum_{\Delta f} S(f)\, df, \tag{3.28}$$

By employing equation 3.28 to represent the Fourier transform and equation 3.27 to characterise the time signal, an attempt is being made to verify the conservation of power. The three signals as in figure 3.13 are also plotted as dB values in figure 3.14, calculated and plotted with MATLAB script PWRPSDtestfft.m in Appendix A.
Figure 3.14 illustrates the differential behaviour of the two frequency peaks. The peak at 2006 Hz exhibits a broader main lobe compared to the 2000 Hz peak. This discrepancy arises because $f_1$ is a precise multiple of N, whereas $f_2$ is not, resulting in spectral smearing for $f_2$. A window function is incorporated into the signal to deal with this issue, as detailed in section 3.2.2. The outcome of this modification is depicted in figures 3.15.
The time domain power $\Pi_t$ is calculated by 3.27 and was

$$\Pi_t = 7.5010. \tag{3.29}$$

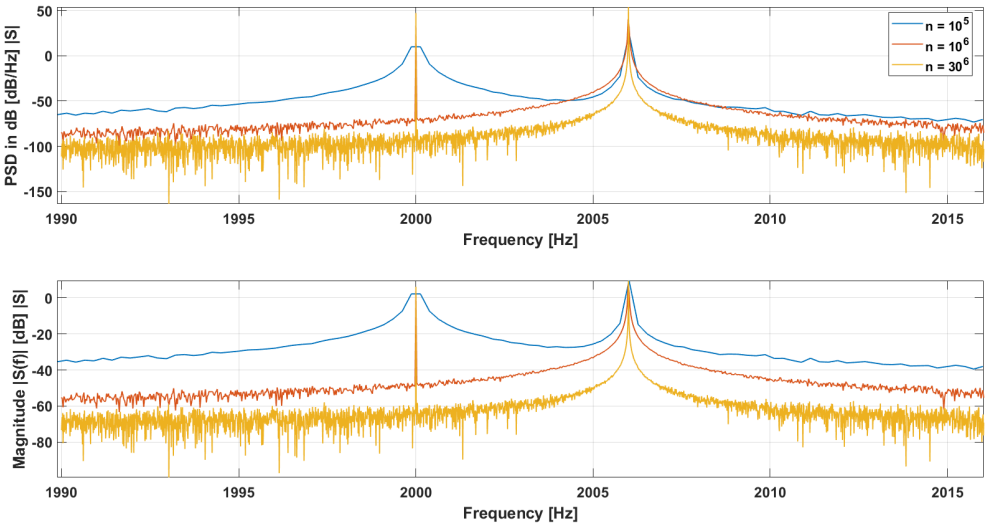


*Figure 3.14: Comparison of power spectrum and PSD for signal s(t) with different signal lengths in dB.*

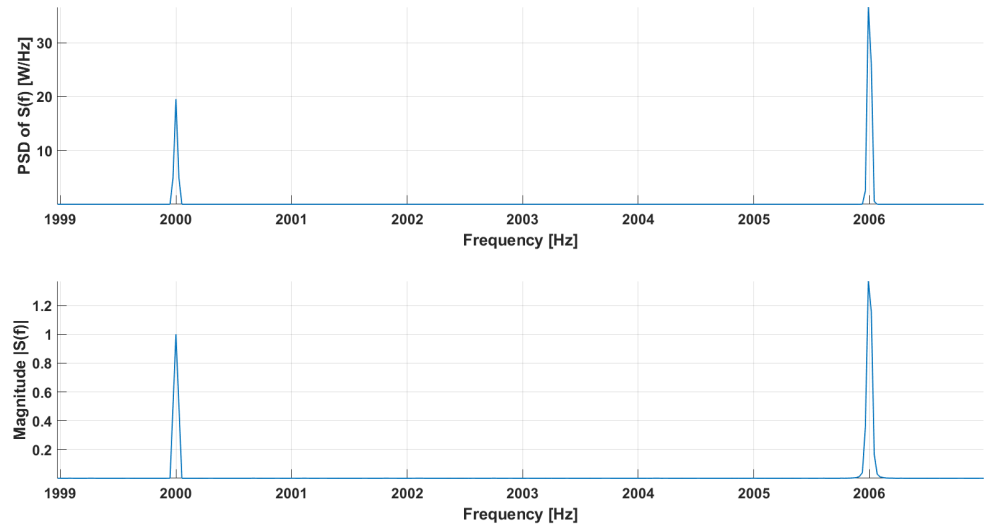


*Figure 3.15: Comparison of the power spectrum and PSD for signal s(t) with applied hann window. .*

The frequency domain power was calculated by 3.28 and was

$$\Pi_f = 2.8119, \tag{3.30}$$

which shows that $\Pi_t \neq \Pi_f$ and confirms the effects of windowing as described in 3.2.1. The amplitudes of the two sinusoids are also wrong. A signal cannot be both a power signal and an energy signal, according to [44]. The effect of a window can be fixed by applying correction factors. The correction factors differ depending on desired correct energy or correct power. According to [42], the correction factor for the Hanning window for the amplitude $C_a$ is 2 and for the energy $C_e$, it is 1.63 and is applied by

$$X(f)_c = X(f) \cdot C_i \ , \ i \in a, e. \tag{3.31}$$

Figure 3.16 and figure 3.17 shows the same plot as in 3.15 together with one signal with energy correction and one with power correction.

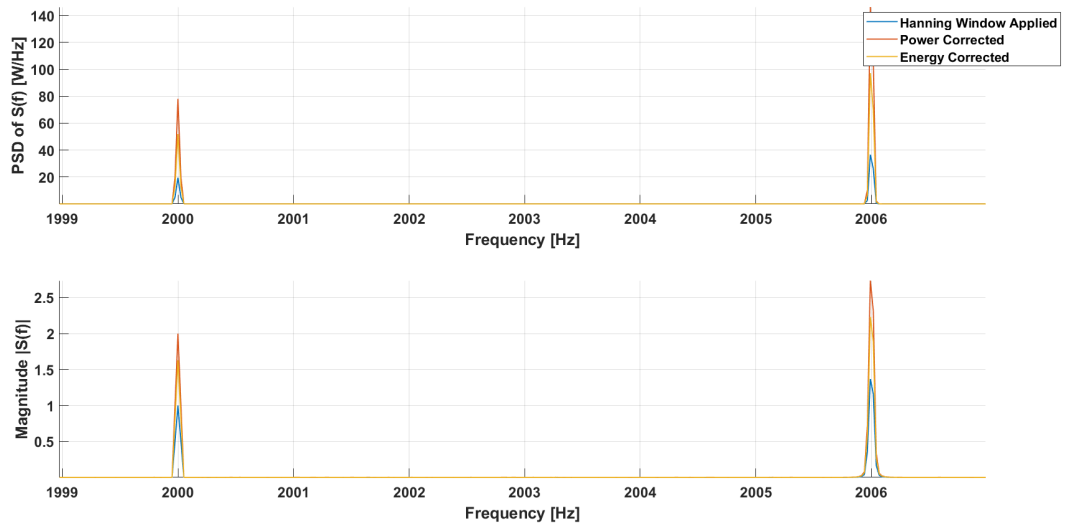


*Figure 3.16: Amplitude and PSD for s(t) with applied hanning window, plotted with no correction factors, with power correction and energy correction.*

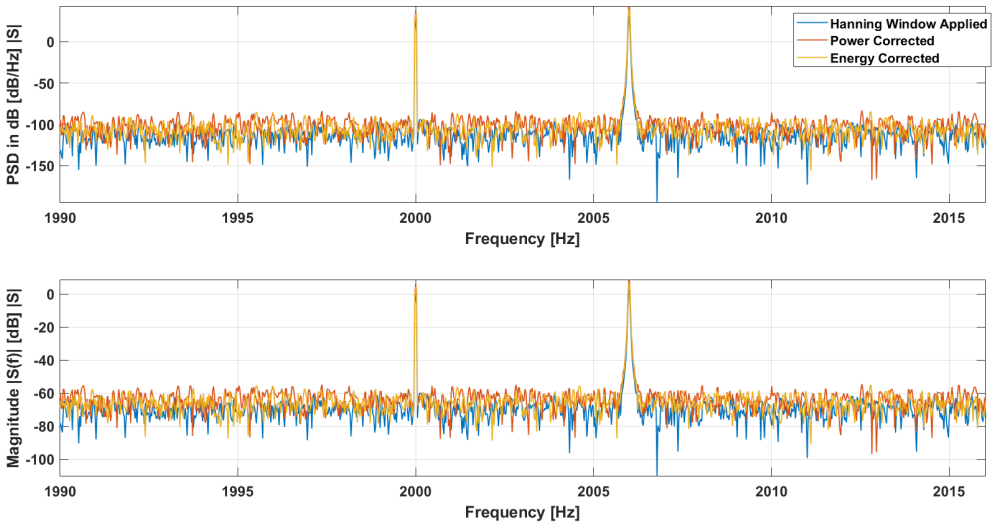


*Figure 3.17: Amplitude and PSD for s(t) with applied Hanning window, plotted with no correction factors, with power correction and energy correction in dB.*

Paravel's was tested for all the cases and is shown in table 3.3. The different $\Pi_t$ is due to the added noise in the signal.

*Table 3.3: result of no correction factor, amplitude correction and energy corrected.*

| Correction | $\Pi_t$ | $\Pi_f$ |
|---|---|---|
| No Correction | 7.5012 | 2.8120 |
| Amplitude Corrected | 7.5028 | 11.2490 |
| Energy Corrected | 7.4997 | 7.4714 |

Figure 3.16 shows that the amplitude is correct the signal is corrected with $C_A$ and table 3.3 shows that the energy is correct when $C_e$ is applied.

### 3.2.4 1/3 - Octave Band Average Power Representation

An octave band is a frequency band defined by a centre frequency $f_c$ , a lower frequency $f_l$ and a upper frequency $f_u$ . For 1/3- octave band, the centre frequencies can either a base 10 or base 2 system. In this thesis the base 10 system is used in accordance with ANSI S1.11 [45] section 3.2 which states that both can be used, but base 10 is preferred. The centre frequencies for a 1/3 - octave band is calculated by

$$f_c = 10^{0.1B},\ B \in \mathbb{Z}, \tag{3.32}$$

where $B$ is the band number. The lowest band considered in this thesis is $B = 11$ and $f_c = 5.0119$ Hz. The lower and upper frequencies is calculated by [45]

$$f_c = 2^{\frac{1}{6}} f_l = \frac{f_u}{2^{\frac{1}{6}}} \tag{3.33}$$

The signal s(t) from 3.17 is used to demonstrate the octave band calculation. The values inside the octave bands is decided to be the average power, which is given by 3.23. The reason for this is that it makes it possible to compare different data sets without concerning different length and sampling frequency. To ensure the correctness, the sum of all the average power inside each band, should equal the power of the signal in the time domain before the applied processing, following Parsavels theorem,

$$\Pi_t = \sum_B \Pi_f \tag{3.34}$$

where $\Pi_t$ is given in 3.27 and $\Pi_f$ from equation 3.28 for each octave band B. ParaThe 1/3 octave band of the average time power for signal 3.17 is plotted in figure 3.18. The frequencies in 3.17 is now $f_1 = 1000$ Hz and $f_2 = 2000$ Hz. The pwelch.m is used to calculate the window corrected PSD of s(t). The MATLAB script octavetestpwelch. in Appendix A returns the average power inside each 1/3 - Octave-band as described in 3.2.4 . The function has the power spectral density, DFT-points, sampling frequency , and amount of samples as inputs . The output is the average power of each octave band.

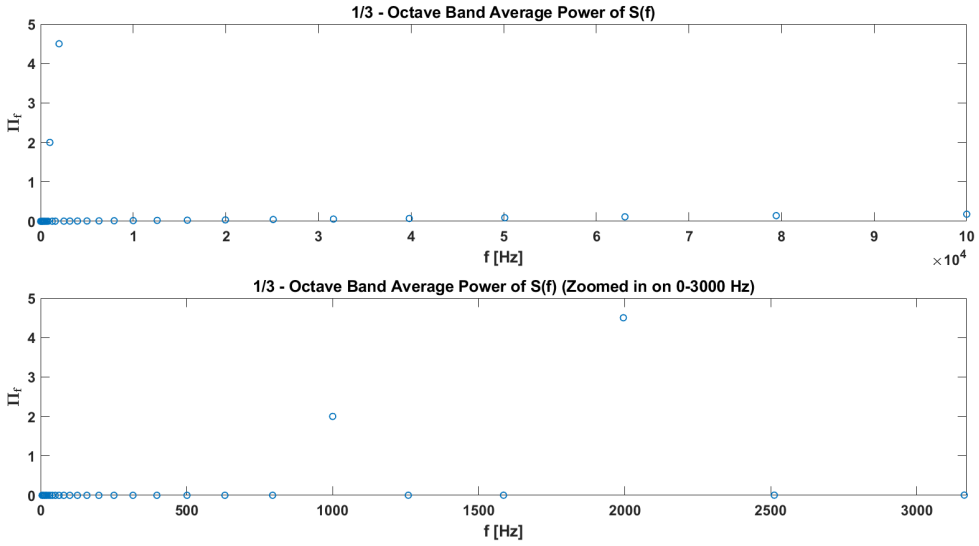


*Figure 3.18: 1/3 - Octave Band Test*

As seen in the lower subplot of figure 3.18, there are large power contributions in the correct bands, both in the bands containing $f_1$ and $f_2$. It is worth noticing that $\Pi_f$ is slightly increasing for higher frequencies. The reason why it is not zero for the other bands is because of the noise contribution which contributions to the average power for every 1/3 - octave band. The reason why the average power is increasing is because the average power is calculated by the sum of $\Pi_f$, such that the noise influence becomes larger for greater band width's. In table 3.4, Parsavels is checked with both PSD and the 1/3 octave band. $\Pi_{f_{\text{OCT}}}$ has a larger deviation from

*Table 3.4: Result of Power of Time Signal, PSD and 1/3 - Octave Band PSD*

| $\Pi_t$ | $\Pi_{f_{\text{PSD}}}$ | $\Pi_{f_{\text{OCT}}}$ |
|---|---|---|
| 7.5032 | 7.5035 | 7.3803 |

$\Pi_t$ than $\Pi_{f_{\text{PSD}}}$. The reason for this is that the fft only calculates the frequency up to half the sampling frequency $f_s$. In this example $f_s = 256000$ Hz, which makes the highest calculated PSD value to be

$$fs/2 = 128000 \text{ Hz}. \tag{3.35}$$

This is not a value of a edge in the 1/3 - octave bands. The last full 1/3 octave band which is possible to calculate is when $B = 50$ where the centre frequency is

$$f_{c_{B=50}} = 100000 \text{ Hz}, \tag{3.36}$$

which makes the last frequency included in the sum of $\Pi_f$ the upper frequency

$$f_{u_{B=50}} = 2^{\frac{1}{6}} f_{c_{B=50}} = 112246 \text{ Hz}. \tag{3.37}$$

For the next band B = 51, the upper frequency becomes

$$f_{u_{B=51}} = 2^{\frac{1}{6}} f_{c_{B=51}} = 141309 \text{ Hz}, \tag{3.38}$$

which makes the band include frequencies that there are no data on. To cope with this, the sum of the remaining frequencies from the remaining band $f_{u_{B=50}}$ is added to $\Pi_{f_{\text{OCT}}}$ by

$$\Pi_{f_{\text{OCT}_c}} = \Pi_{f_{\text{OCT}}} + \sum_{f_{u_{B=50}}}^{f_s/2} S_{\text{PSD}}(f)\, df \tag{3.39}$$

The result of this can be seen in table 3.5 As seen in table 3.5

*Table 3.5: Result of Power of Time Signal, PSD and Corrected 1/3 - Octave Band PSD*

| $\Pi_t$ | $\Pi_{f_{\text{PSD}}}$ | Corrected $\Pi_{f_{\text{OCT}_c}}$ |
|---|---|---|
| 7.5028 | 7.5036 | 7.5036 |

$$\Pi_{f_{\text{PSD}}} = \Pi_{f_{\text{OCT}_c}} \tag{3.40}$$

Note that

$$\Pi_t \neq \Pi_{f_{\text{PSD}}} \vee \Pi_{f_{\text{OCT}_c}}, \tag{3.41}$$

because of the added random noise in the signal.

### 3.2.5 MATLAB Built-In Functions

pwelch.m

The built in function pwelch.m was used which is based on the Welch method. The Welch method is based on the Bartlett method, which averages multiple different periodograms from non-overlapping parts of a signal to average out noise components [46]. The overlapping is used to prevent data loss. As defined in the MATLAB documentation, the function is called like in eq. 3.42.

$$[\text{pxx,f}] = \text{pwelch(x,window,noverlap,nfft,fs,spectrumtype)} \tag{3.42}$$

The output of this function is pxx and f, where pxx is either the one-sided power spectral density or the power spectrum, depending on the defined spectrum type. The inputs are also given in eq. 3.42. The first input x is the signal, and nfft is the amount of desired DFT points. The number of sample overlap between the snippets are defined as the noverlap input. Input fs is the sampling frequency, and spectrum type is either the power spectral density or the power spectrum. The correction factors for the Hanning window used in pwelch.m is found by using bias correction found in [47] according to [48]. It was confirmed that pwelch.m returns the power spectrum and PSD in accordance with 3.23 and 3.22, the amplitude response and PSD of the same signal as in 3.25 with A = 3 and B = 2, as plotted in figure 3.19 with a Hanning window applied and N = $10^7$.

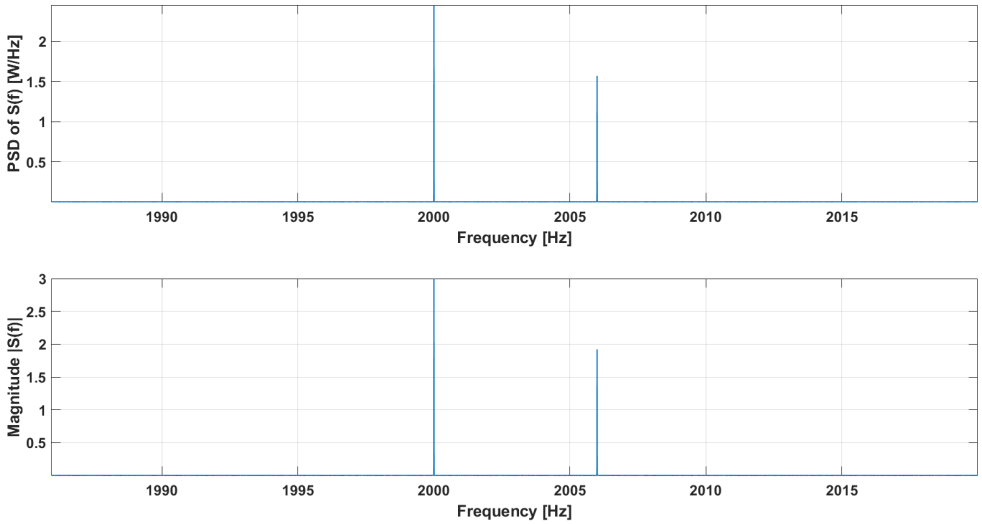


*Figure 3.19: Test of pwelch.m with same signal as in 3.25*

### 3.2.6 Flow Diagrams of The Signal Processing

A comparison will be made between different data sets with varying sampling frequencies ($f_s$) and total sample sizes ($N$). From now on the URN is defined as

$$\text{URN} = \text{SPL}(\text{cpa}) \tag{3.43}$$

When analyzing single frequency components, precise amplitude determination for each frequency component is crucial. However, comparing power spectra obtained from a Fast Fourier Transform (FFT) does not provide accurate results. The resolution of the FFT relies on the sampling frequency and signal length, which vary among the sensors used in this study. As a result, the Discrete Fourier Transform (DFT) points would differ for each sensor, making it impossible to compare tonal frequency amplitudes directly. Furthermore, in order to ensure that high-amplitude frequencies' side lobes do not overshadow smaller frequency amplitudes, it is necessary to apply a windowing function for correct comparison of tonal power amplitudes.
However, achieving the simultaneous preservation of both energy and power amplitudes, as described in section 3.2.3, is not feasible. Therefore, two different comparison methods need to be employed: one for tonal comparison, where accurate amplitudes are essential, and another for 1/3-octave band comparison, where the total energy within a band is of importance. These two methods are illustrated using flow charts in Figure 3.20 and Figure 3.21.

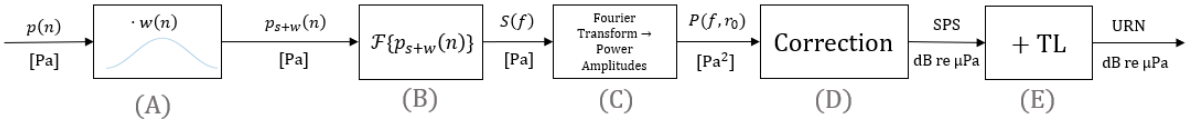


*Figure 3.20: Flow diagram illustrating the process of comparing different signals and propagation loss methods for tonal frequencies. (A) Windowing. (B) shows the applied window function $w(n)$ described in Section 3.2.1. (C) Displays the transformation from Fourier spectrum to power spectrum $P(f)$. (D) represents the corrections applied for windowing, baffled sensor, and backtrack, and returns the PSD at the source. (E) is where the transmission loss is added to the PSD from (D). Out from E comes the URN given by equation 3.43.*

In Figure 3.20, the signal $p(n)$ initiates the processing steps. The discrete pressure signal, which is pre-calibrated, undergoes the application of the wav-correction $c_{\text{wav}}$ if the measurements are conducted with near-field pressure sensors, as described in Section 3.1.1. In (A) a window $w(n)$ is applied to signal $p(n)$, which is described in 3.2.1. Out from (A) comes the window corrected pressure signal $p_{s+w}(n)$. The Fourier spectrum $S(f)$ is the calculated in (B) using either with the pwelch.m command described in 3.2.5 or the DTFT described in section 3.2. In (C) the Fourier spectrum is made into a power magnitude spectrum as described in 3.22. If the pwelch.m is used, with spectrum-type 'power', this is done automatically. Further in (D) the power spectrum $P(f, r_0)$ is corrected for applied for windowing , baffled sensor , and backtrack, described in section 3.2.1, 2.8 and 2.5 respectfully and returns the sound pressure spectrum (SPS). Finally in (E), the transmission loss TL is added to the SL, to obtain the URN as described in 3.43
In the case of 1/3-octave band processing, the procedure is similar to the tonal component processing. As depicted in Figure 3.21, it begins with the same signal (F) as in Figure 3.20 (A). In (F), the Fourier transform is calculated in the same manor as in (B). After that, (G) transforms the Fourier transform into a power spectral density (PSD) $S_{\text{PSD}}(f)$ as described in eq. 3.28.Then $S_{\text{PSD}}(f)$ is corrected for in (H) in the same way as (D), only without the

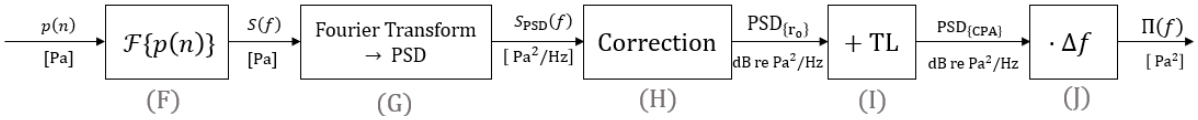


*Figure 3.21: Flow diagram of the process of comparing the different signals and propagation loss methods. (G) is the discrete calibrated pressure signal $x(n)$. (H) is the Fourier transform power spectral density $S(f)$ of $x(n)$. (I) is the distance correction described in eq. 2.18 and the baffled sensor correction. (J) is the source power level. (K) Propagation Loss is the power relative TL. (L) Underwater radiated power.*

window correction, since no window was applied. Then the TL is added to the $\text{PSD}_{r_0}$ to obtain the power pr frequency band at the hydrophone in (I). Then in (J) the length of the frequency band is multiplied to obtain the power at the hydrophone $\Pi(f)$. This value will be then be summed to obtain the average power in the 1/3 - octave band representation as shown in 3.34.

# Chapter 4

# Results

The aim of this thesis was to propose a sound propagation model for underwater noise emitted by a ship in the far field, investigate far field hydrophone measurements, and compare various methods for calculating radiated noise underwater. The results of these objectives are presented in this section.Section 4.1 introduces the proposed model, along with the near- and far-field measurements. The data is processed according to the procedure outlined in figure 3.20. In Section 4.2, an analysis of different abnormalities in the far field data set is conducted, employing the same signal processing approach as in section 4.1. Finally, Section 4.3 provides a comparison of the different models, with the data processed as depicted in figure 3.21.

## 4.1 Proposed Model

According to ISO, DNV, and BV standards, pressure values are presented using octave bands. In line with the DNV Silent-E protocol, a 1/3 octave band is utilized. The detailed explanation of the 1/3 octave representation can be found in section 3.2.4. However, employing octave bands entails sacrificing specific tone frequency information, particularly in higher frequency bands, where individual components become indistinguishable within the average.
The pwelch.m function was employed to determine the amplitudes of the single-frequency components. The outcome of this analysis is depicted in figure 4.1, where the MATLAB script FirstComparisonAllFreq.m in Appendix A was used for the calculation and plotting.
The Lloyd mirror effect cannot be discerned adequately when averaging over a longer time signal, as the effect fluctuates between constructive and destructive interference due to the boat's movement and changing distance. This outcome is described in detail in section 2.3 and depicted in figure 2.6. The proposed model perceives the frequencies as constant in time and position. Therefore, a shorter time signal is preferable, as it enables the use of a constant distance approximation to calculate the Lloyd mirror effect. Figure 4.1 shows all the single-frequency components. The Lloyd mirror effect is clear,seen as repeated amplitudes dips for the proposed model, but no sign of the Lloyd mirror effect on the far field measurement exists.

To make an accurate prediction and be able to compare a prediction with the hydrophone data, distance and time has to be precisely decided. The first proposal was to look for short single-frequency tonals in the near- and far-field data, to synchronise the far field hydrophone and the pressure sensor. By comparing when these frequency abnormalities occurred, one could synchronise the two data sets, and then more correctly use a constant distance approximation as discussed above. Then by the assumption that the amplitude of the ship's radiated noise would

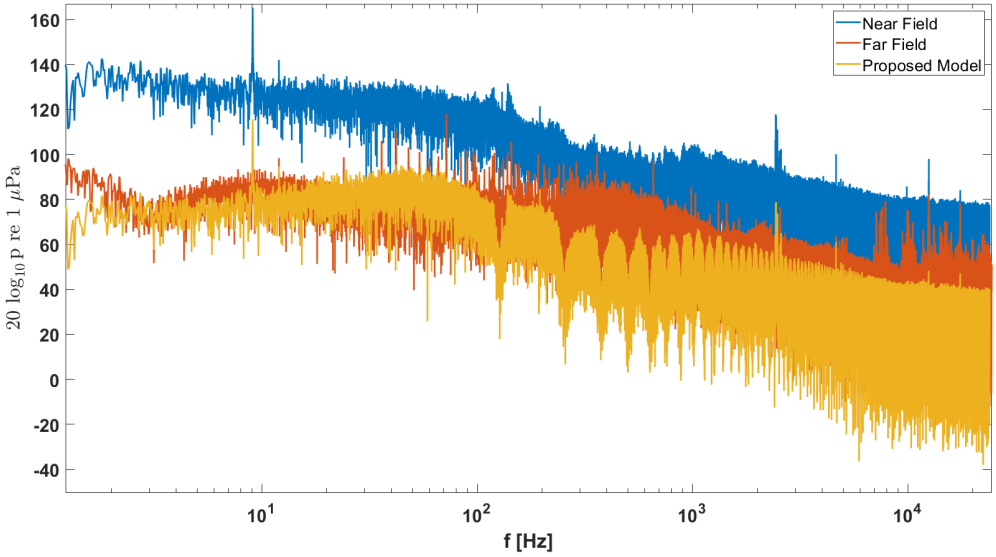


*Figure 4.1: pwelch.m function to determine the amplitudes of the single frequency components*

increase as the ship approached the hydrophone, one would find the closest point of approach time stamp by using the time when the hydrophone has the max amplitude from a single frequency radiated from the ship, firstly assumed to be the blade pass frequency.

The near field is measured directly above the propeller. The most prominent frequency is assumed to be the blade pass frequency,$f_{bp}$, which could be a good reference between the near field and the far field. The blade pass frequency is the frequency at which one of the propeller's blades passes the pressure transducer. The ship propeller has five blades. According to [19], a typically $f_{bp}$ is between 8 - 15 Hz. By applying a Fourier transform, finding the blade pass frequency in the power spectrum of the near and far field should be possible. Because the assumed frequency range is known, the frequency band can be minimised, and the resolution can be high. MATLAB's built-in function fft.m frequency resolution is defined by sample size and sample frequency desribed in eq. 3.9. The author considers a discrete time-frequency Fourier transformation (DTFT) better suited for this task because of the continuous frequency response contrary to the fft, which is discrete in the time domain. The DTFT is decribed in eq. 3.10.
A necessary high-frequency resolution is used to analyse single-frequency components precisely. The result of dividing the signal into 1-second snippets, applying the DTFT.m with a frequency resolution of 0.001 Hz and a Hanning window is shown in 4.2.
As seen in figure 4.2, there is a time constant peak at 9 Hz. Since this is constant, contrary to the other frequencies, this is assumed to be the blade pass frequency. Furthermore, measured as 9 Hz, it seems plausible that this is the $f_{bp}$ because of the time consistency and close to an expected $f_{bp}$
The evolution of $f_{bp}$ over time is illustrated by a spectrogram in figure 4.3. The spectrogram time resolution is defined by the number of DTFTs done on the signal, i.e., how many snippets the signal is divided into. The time resolution, or the amount of DTFTs, is decided by the lowest considered relevant frequency. Since the assumed lowest blade pass frequency is 9 Hz, the smallest relevant frequency is considered to be 4 Hz. A 4 Hz signal has four periods in a second. From table 3.2, the duration for run 9 at P1 is 54 s. This means that it would be four periods of the 4 Hz signal in every DTFT. Ideally, the time resolution would be as small as

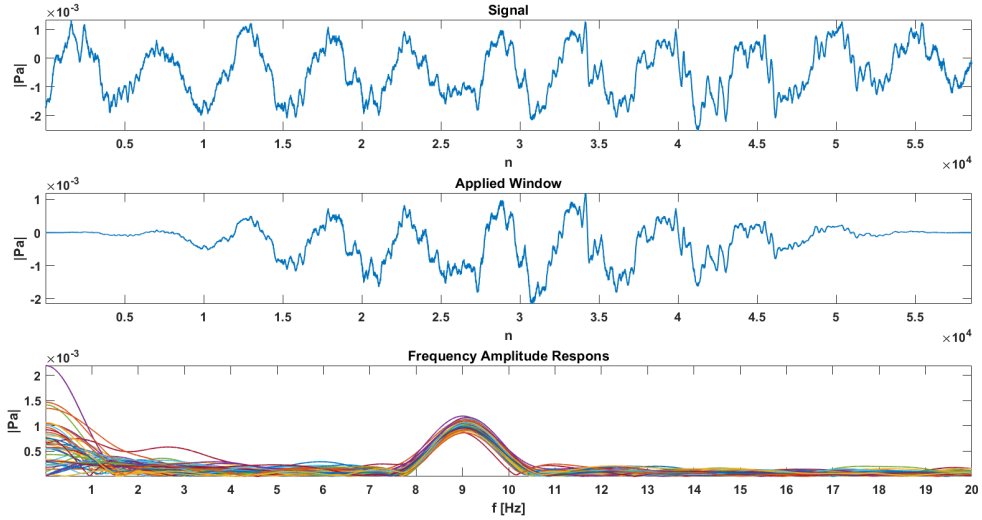


*Figure 4.2: Near Field Discrete Time Fourier Transform from 0 - 20 Hz on a 55 s long signal, with 1 s snippets.*

possible. However, if the time resolution, for example, would be 0.25 s, then only one period of the 4 Hz signal would be in every DTFT. This would be the absolute minimum for a distinct answer, and is described in section 3.2.2. When there is also an applied Hanning window on the signal, more than one period is needed since the Hanning window weights out the beginning and end of the signal. Therefore, at least 4 periods are decided as the minimum signal, and 1-seconds snippets will be enough to see the $f_{bp}$.

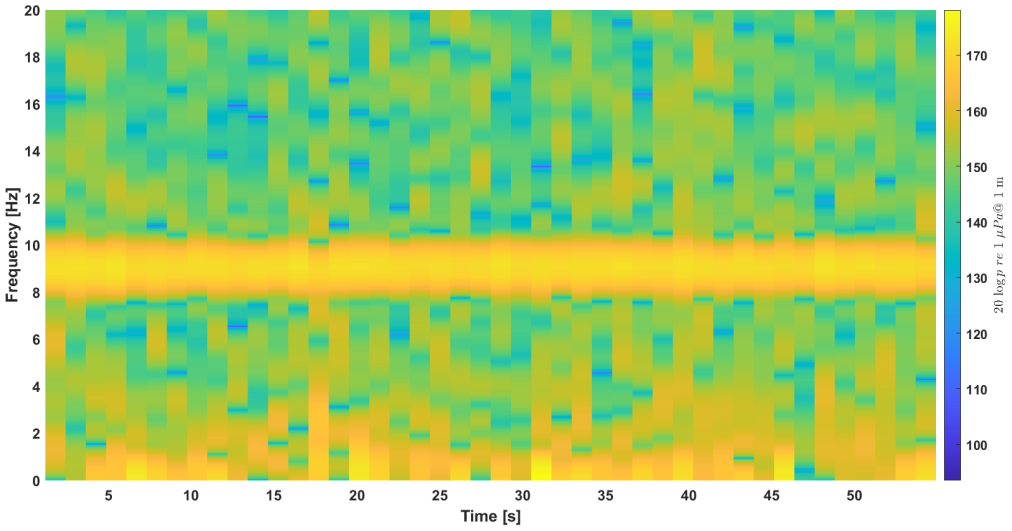


*Figure 4.3: Near Field Spectogram of amplitudes from figure 4.2*

figure 4.3 illustrates a noticeable and consistent amplitude at approximately 9 Hz. A similar signal processing is applied to the far field hydrophone to check if the $f_{bp}$ is as prominent as in the near field. The far-field signal in run 9, as shown in table 3.2, is 85 second long. The signal is divided into 45 snippets, and the frequency resolution is now 0.01 Hz. Far Field pro-

cessing and spectrogram is shown in figure 4.4 and 4.5.

It seems like the prominent $f_{bp}$ in the near field is not clearly visible around 9 Hz in the

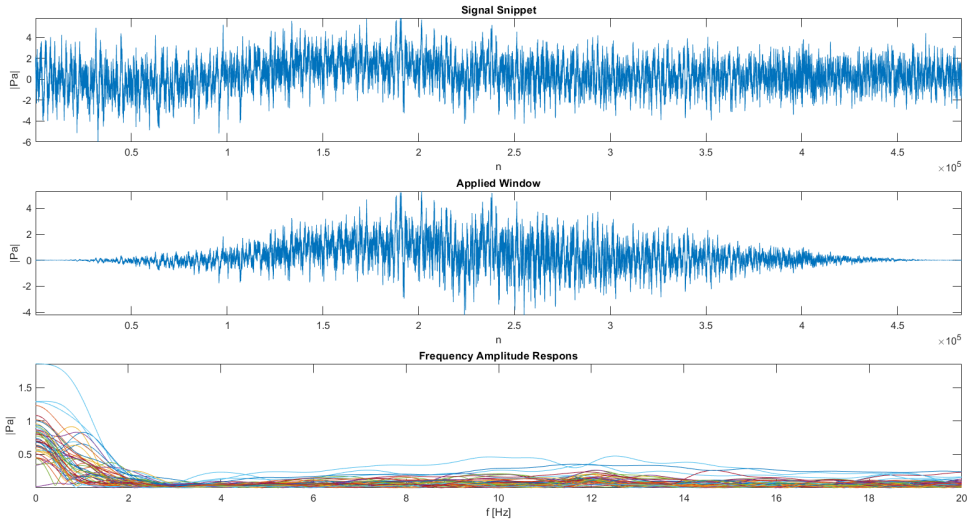


*Figure 4.4: Far Field Hydrophone signal with applied window and DTFT*

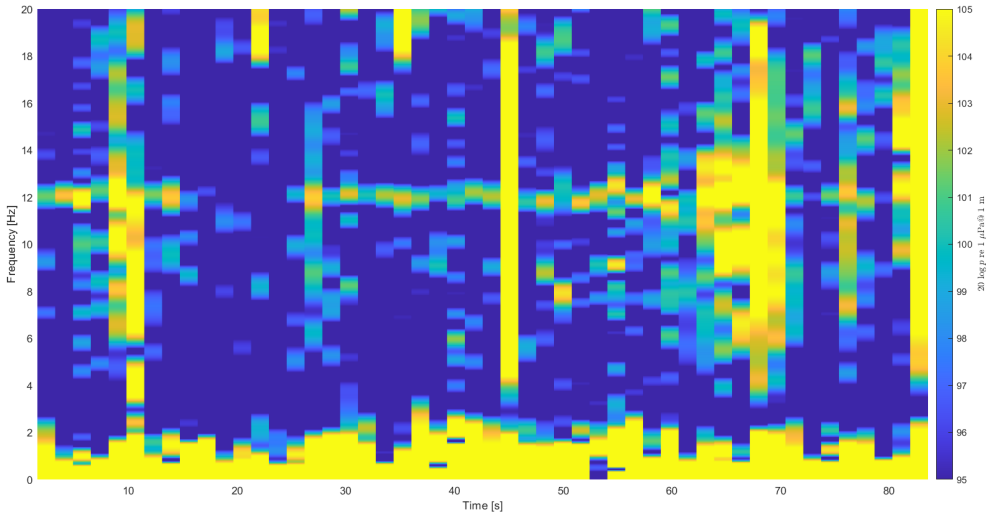


*Figure 4.5: Far Field Hydrophone Spectogram*

far field, which makes it impossible to use $f_{bp}$ amplitude time development to try to estimate the ship position. The second approach is to use another evident frequency to look at. The frequency up to 24000 Hz is plotted with a resolution of 5 Hz. There is no need for a high-frequency resolution of a broad frequency spectrum because the goal is only to find smaller frequency bands where there could be single-frequency tones. One of the benefits of the DTFT.m is that one can decide the resolution easily, and can first be found to use a target frequency band and then increase the resolution in this band to find single frequency tones. The DTFT frequency response is shown in figure 4.6 together with a zoomed-in version beneath. As expected, the highest amplitudes are in the low frequencies, and the band 0 - 3000 Hz is considered the most relevant. To look for time constant frequency component, a spectrum is

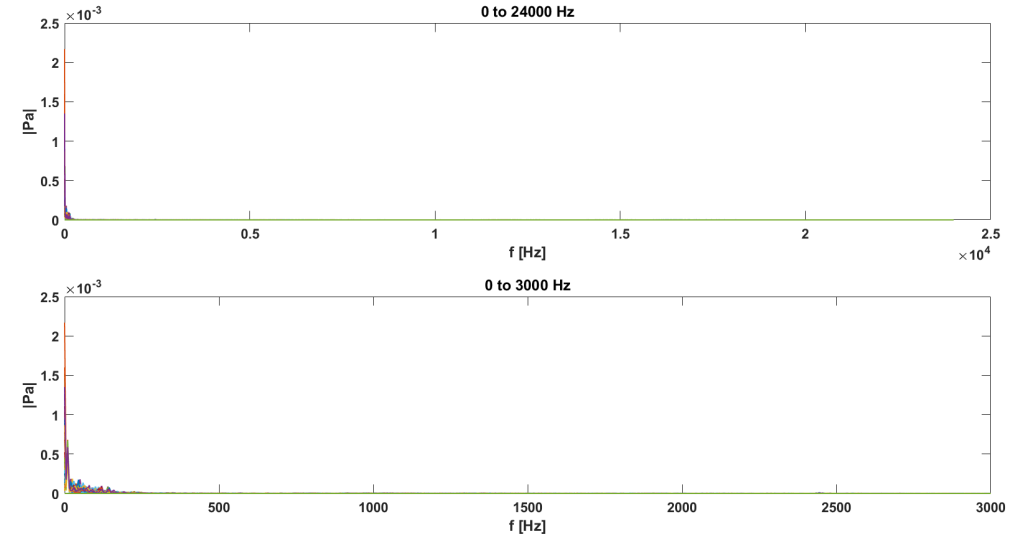


*Figure 4.6: Low-Resolution Frequency response for Near Field from 0 to 24000 Hz (Upper) and from 0 to 3000 Hz (Lower)*

plotted in figure 4.7 on the same signal with the same resolution and frequency band.

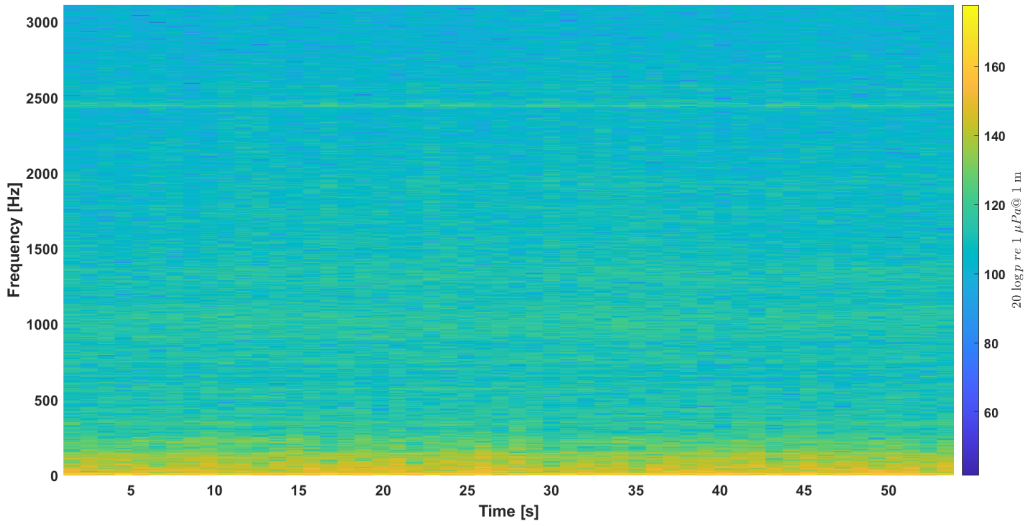


*Figure 4.7: Frequency Spectra from 0 to 3000 Hz for Near Field*

Figure 4.7 shows a low-frequency band (f < 200 Hz) with present noise , where finding a deterministic single frequency is hard. However, at around 2460 Hz, figure 4.7 shows a deterministic frequency. It has a lower amplitude than the frequencies in the lower band but is seemingly close to time constant. A frequency amplitude response and a spectrogram is plotted in figure 4.8 with frequency band 2420 to 2465 Hz with a resolution of 0.01 Hz.
In figure 4.8, prominent time-frequency components are observed at 2436 Hz, 2445 Hz, and 2454 Hz. Among them, 2445 Hz exhibits the highest mean amplitude. Consequently, the frequency band associated with 2445 Hz was further analyzed in the far field. The frequency range was narrowed down to 2430-2460 Hz due to its significance. Figure 4.9 displays the resulting frequency spectrum and spectrogram for this selected frequency band.

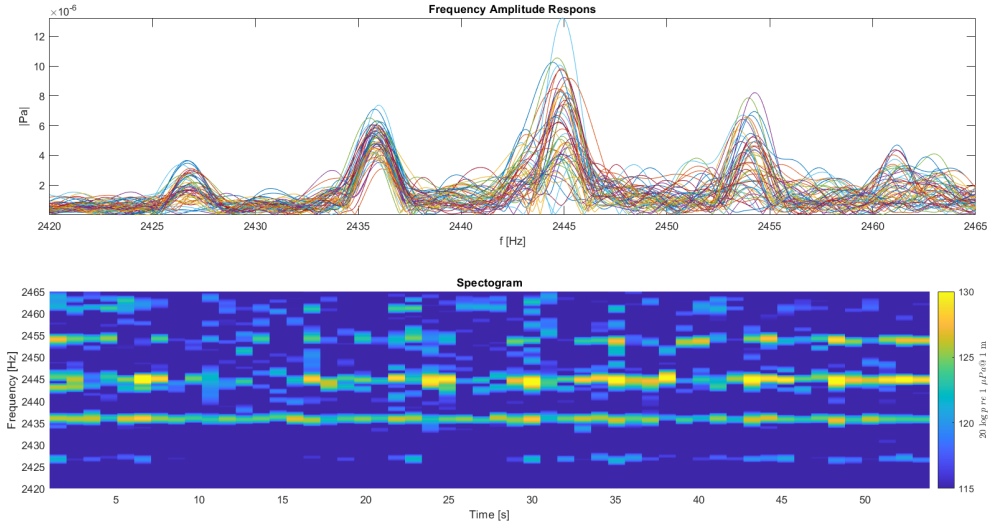


*Figure 4.8: Frequency Spectrum and Spectogram for Near Field from 2420-2465 Hz*

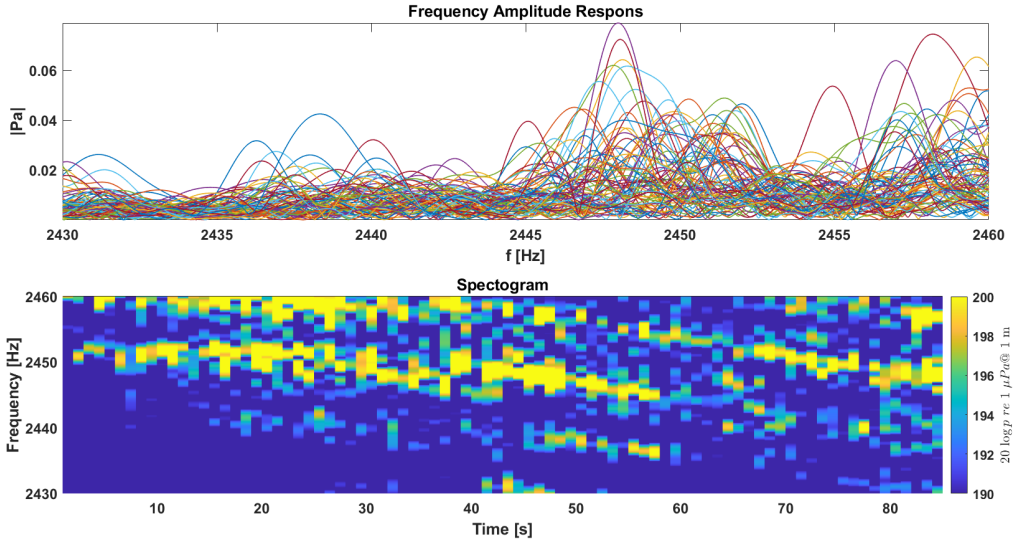


*Figure 4.9: Far Field Frequency Amplitude Response and Spectogram*

Interestingly, there are also some prominent frequencies in the far field in the same frequency domain. The difference, however, is that the frequencies seem subject to a frequency shift. The earlier proposal suggested examining the time progression and studying changes in amplitude by positing that an increase in amplitude would lead to a decrease in distance between the source and receiver. As seen in figure 4.9 it is hard to argue that there is a clear amplitude trend to describe the distance, because it shows that the amplitude changes does not follow any clear time dependency, even tough the distance is time dependent. The frequency shift, however, seems like a possible Doppler shift. The Doppler shift could give a relatively precise indication of when the signal source is closest to the receiver, which will be introduced in the next section.

### 4.1.1 Doppler Shift

Since there was no apparent correlation between amplitude and distance to the far-field hydrophone, the Doppler effect is considered. The Doppler frequency shift for a moving source with a stationary receiver will be positive while the source approaches the receiver and negative when the source has passed the receiver. For a brief moment, when the target is closest to the receiver, the Doppler shift $\Delta\omega$ is 0. This can be used to estimate when the ship is closest to the hydrophone.

The first idea was to look at the blade pass frequency. However, two reasons why the blade pass frequency was unsuitable was quickly discovered. Firstly and most importantly is that the relative speed $v_r$ the boat would need to have to obtain a visible frequency shift $\Delta\omega$ , for example 1 Hz, for a 9 Hz initial frequency

$$v_r = \frac{c\Delta\omega}{\omega_0} = \frac{1500 \text{ m/s} \cdot 1 \text{ .Hz}}{9 \text{ Hz}} = 166.667 \text{ m/s}, \tag{4.1}$$

which seems unlikely. Secondly, the blade pass frequency amplitude is not distinguishable, which makes it hard to determine where the frequency shift is 0. A constant frequency in the near field is desired to clearly observe the frequency shift in the far field. As discovered in section 4.1, a suitable frequency band is from 2400-2500 Hz. Using eq. 4.1, the approximate relative ship speed for an observable frequency shift, like 4 Hz, is $v_r = 2.4\ m/s$, which seems like a possible relative ship speed.

The relative speed of the boat was calculated. This is simplified to a one-dimensional situation where the distance D is the direct distance between the source and the hydrophone. The time relative change of this distance, $v_d$, is the velocity required to calculate the Doppler shift. Since the data does not contain any specific speed or position, it is assumed that the time signal on the hydrophone starts when the ship stern passes the Hydrophone. The ship length is 205 m, and it is assumed that the source that emits the 2445 Hz frequency is located at the stern, approximately 205 from 0 on the x-axis. Using the length of the time signals from table 3.2, the assumed speed in the x direction is calculated by simply dividing the length of two ship lengths by the duration of the recordings. For example, for run 1, the speed

$$v_x = \frac{410\ m}{56\ s} \approx 7.321 m/s \tag{4.2}$$

So it is possible to calculate $v_r$ by calculating D at different times using the CPA and x as shown in equation 4.3.

$$D(t) = \sqrt{CPA^2 + x(t)^2} \tag{4.3}$$

The time derivative of D equals the relative speed $v_r$. In figure 4.10, the distance D, relative speed $v_d$, and frequency shift $\Delta f$ as a function of time is plotted for a frequency of 2445 Hz with the use of the MATLAB script DopplerShift.m in Appendix A.

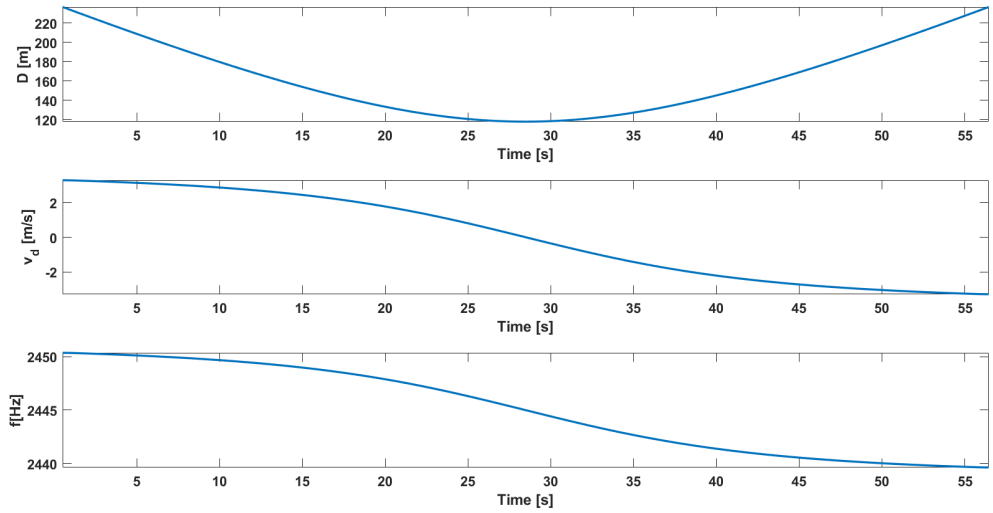


*Figure 4.10: Direct Distance D, Relative Speed $v_d$ and Frequency Shift*

The expected frequency shift is around $\pm$ 5 Hz. By using the DTFT.m script, the actual frequency shift can be determined. The frequency amplitude with the highest average amplitude in the near field is used. It is desired to have good frequency resolution and accurate time resolution. The frequency resolution can be high because of DTFT.m properties. The time resolution could be increased by dividing the signal into smaller sample intervals. To get high time resolution, a overlap of the different sample snippets was used. In figure 4.11, there is a spectrogram of the far field hydrophone with a 0.1 Hz resolution between the frequency band of 2420-2475 Hz. In addition to the spectogram, the Doppler shift is from figure 4.10 is plotted in red on top of the spectrogram. There is also a black line indicating the strongest frequency in the near field, which was 2445 Hz.

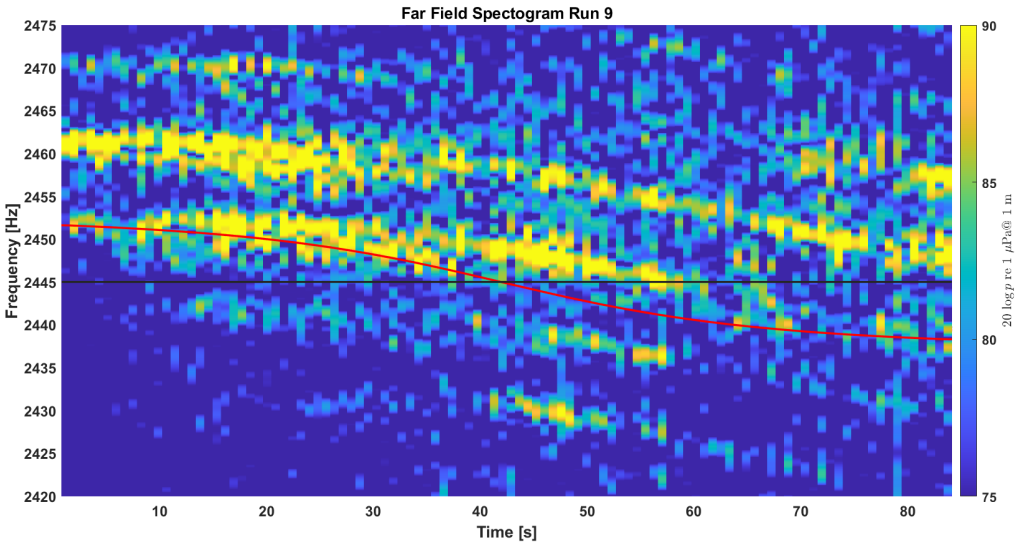


*Figure 4.11: Far Field Hydrophone Spectogram 2420-2475 Hz with theoretical Doppler shift in red. The black line is the 2445 Hz frequency indicator.*

The signal is still divided into 1-second snippets, but the number of snippets is increased because of the overlap. The total signal has the same time length. Every 1 second in figure 4.11 is

represented as 0.25 s in real time, defined by the actual overlap $\frac{f_{sf}}{4}$, since each new time snippet is shifted with 0.25 from the previous. Multiple samples are being used two times. Putting the samples in a spectrogram with a time development leads to a higher time resolution, but smeares the amplitudes. Therefore figure 4.11 must be considered as a time development illustration without concern for the actual amplitudes with respect to time, because the amplitude is smeared.
The gradient of the theoretical Doppler shift and the spectrogram is similar but it looks like the theoretical shift is not synchronised with the spectrogram in 4.11 . The calculation of the Doppler shift is based on an ideal case where the hydrophone has started measuring exactly when the bow is directly in front of the hydrophone and ended when the stern has passed. This might not necessarily be the case. The raw hydrophone data set consists of 7 hours of data, and the relevant time intervals are assumed to be correct. To test this assumption, the theoretical frequency shift was time delayed to check if it would match the spectrogram better. Different time delays were tested. The result of a 15-second delay on the theoretical Doppler shift is shown in figure 4.12.

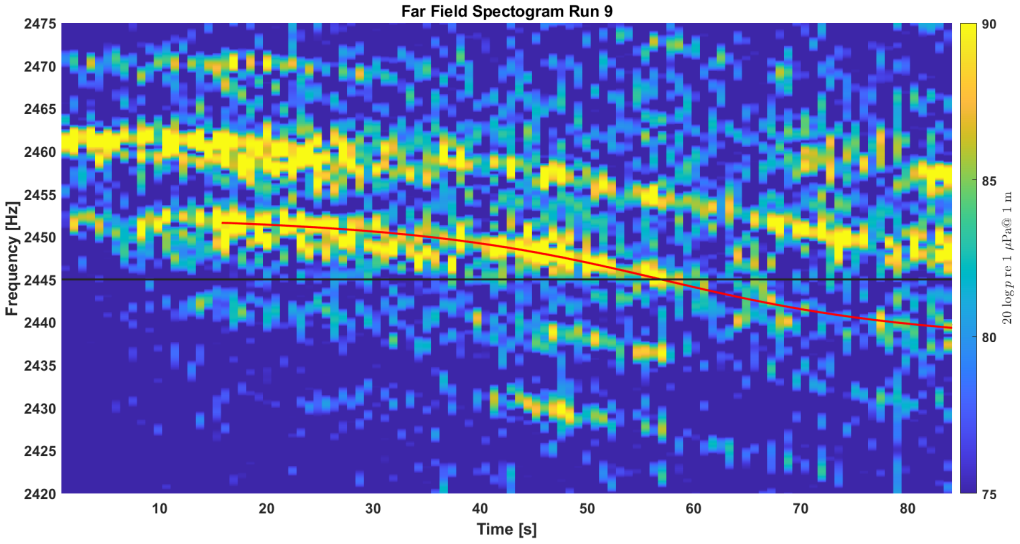


*Figure 4.12: Far Field Hydrophone Spectogram 2420-2475 Hz with delayed theoretical Doppler shift in red. The black line is the 2445 Hz frequency indicator*

The measured far field aligns closely with a delayed theoretical Doppler shift, indicating that the midpoint of the time signal does not coincide with the halfway point of the source's movement during the run. The gradient fits well, strengthening the assumption that the frequency variation observed in the hydrophone data is caused by the Doppler effect. The black line indicated the starting frequency of 2445 Hz. It cross the red graph and the yellow relative high amplitudes after 58 seconds, which would be the time source of the signal is closest to the hydrophone. With this, it is possible to relate the hydrophone time and distance, which was the goal for the single-frequency component analysis. Furthermore, figure 4.12 has some exciting amplitudes variations. After 58 seconds, the amplitudes seem to decay for the 2445 Hz and 2454 Hz components. These amplitudes decay could imply source directivity, challenging the averaging octave band method. A directive source could surpass allowed URN thresholds in the main-lobe direction but could be hidden in an averaged octave band.
The same Doppler analysis was done on another run to verify the results. The first run is chosen and is 30 s shorter than the previously investigated run 9. It is assumed that this run

will have a higher speed hence a greater distance gradient, because the duration is shorter. In the near field, the frequency with the highest average amplitude was found to be 2445 Hz. The same frequency domain is used as in run 9, and the results are shown in figure 4.13.

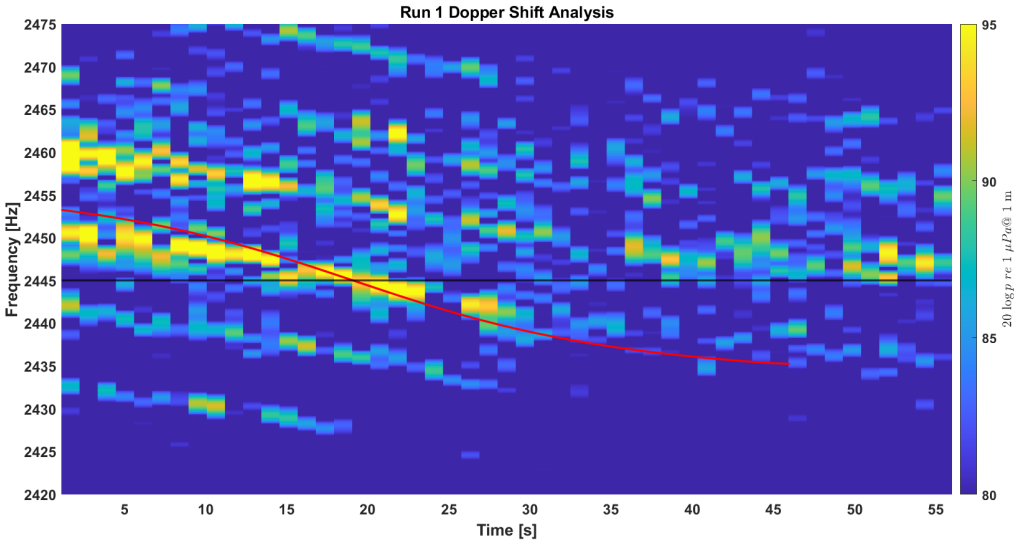


*Figure 4.13: First run Doppler analysis, with - 10 s time delay. Black lines indicate the highest average near field frequency amplitude, and the red slope indicates the Doppler frequency shift with 2445 Hz as the original frequency.*

As one can observe, the trend looks similar, but the gradient of the red line is too big, which indicates a wrong ship velocity approximation. This is most likely because of the assumption that the ship covers a full two ship lengths in the length of the time signal. Since the ship length is 205 meters, this means that the ship would have to travel at a velocity

$$v = \frac{410 \text{ m}}{56 \text{ s}} = 7.32 \text{ m/s} \approx 14 \text{ knots}, \tag{4.4}$$

A speed of 14 knots is plausible. A higher speed would lead to a steeper Doppler slope. It shows that there is no correlation between the ship speed and the duration of the hydrophone signal. The same analysis was done to check this, assuming the same speed as run 9. The speed in run 9 is

$$v_{r2} = 410/84 = 4.8214 \text{m/s}. \tag{4.5}$$

The resulting Doppler analysis is shown in figure 4.14, and the belonging spectrogram is shown in figure 4.15.
The fit also seems good for run 1. The amplitude decays after passing the hydrophone, which could again indicate a directivity of the source.

One can now use the correct distance time interval to increase the conformity of the model and far-field hydrophone. With a high time resolution, the amplitude changes of the signal can be better identified. It would be interesting if the signal amplitude is fluctuating.

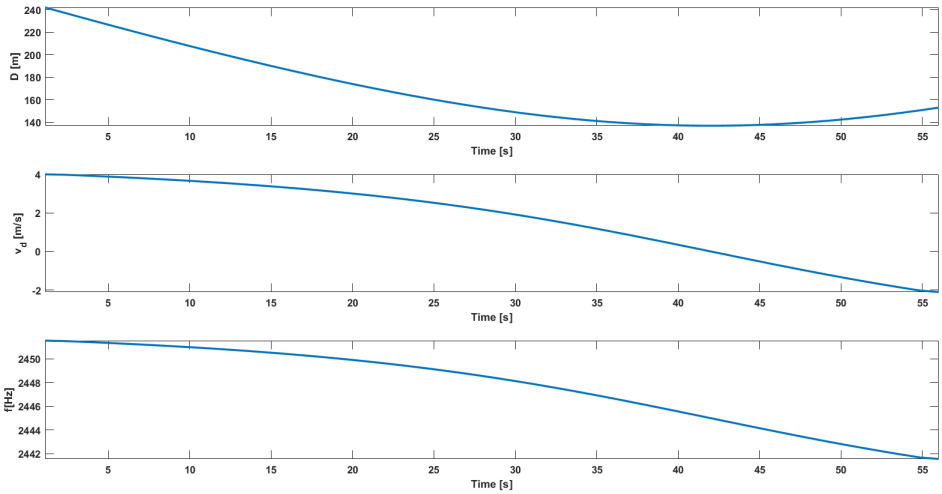


*Figure 4.14: Doppler Analysis with Direct Distance D, Relative velocity $v_r$ and frequency shift.*

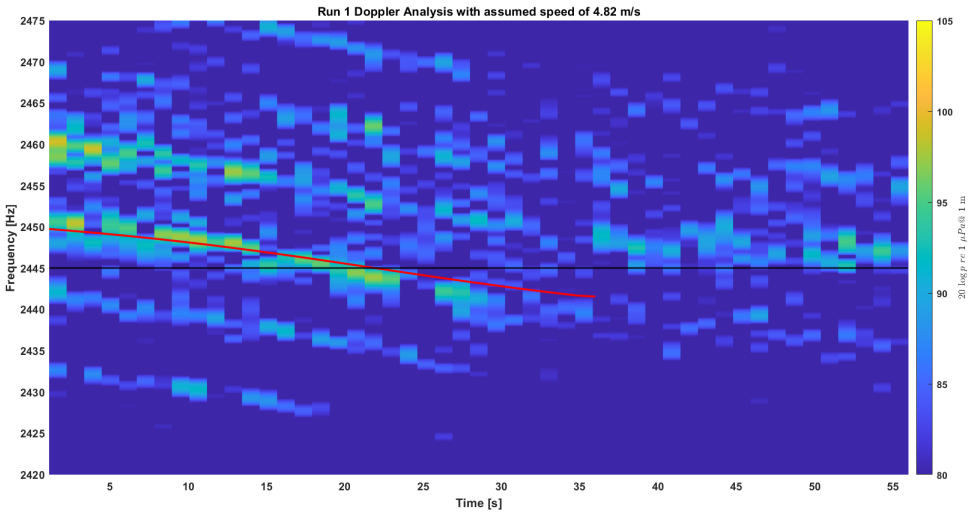


*Figure 4.15: First run Doppler analysis, with - 20 s time delay. Black lines indicate the highest average near field frequency amplitude, and the red slope indicates the Doppler frequency shift with 2445 Hz as the original frequency.*

## 4.1.2 First Lloyd Dip

The destructive interference's first occurrence will be when the reflected and direct waves have a phase difference $\Delta\phi = \frac{\pi}{2}$. As predicted in the same way as in section 2.3, with a $R_d$ of 132 m and $R_r$ of 143 m for run 9, the first expected dip will be at a frequency of

$$k(|R_d - R_r|) = 2\pi \rightarrow f = \frac{2\pi c}{(|R_d - R_r|)2\pi} \approx 127\text{Hz}, \tag{4.6}$$

where $R_d$ and $R_r$ are the direct and reflected distances. Figure 4.16 shows the SPL of the hydrophone for the 59Th second. This second is chosen by interpretation of figure 4.12. Multiple dips around the $f_{bp}$ are observed in the hydrophone measurements, whereas the far-field model shows its first dip at 127 Hz. These hydrophone dips cannot be easily identified

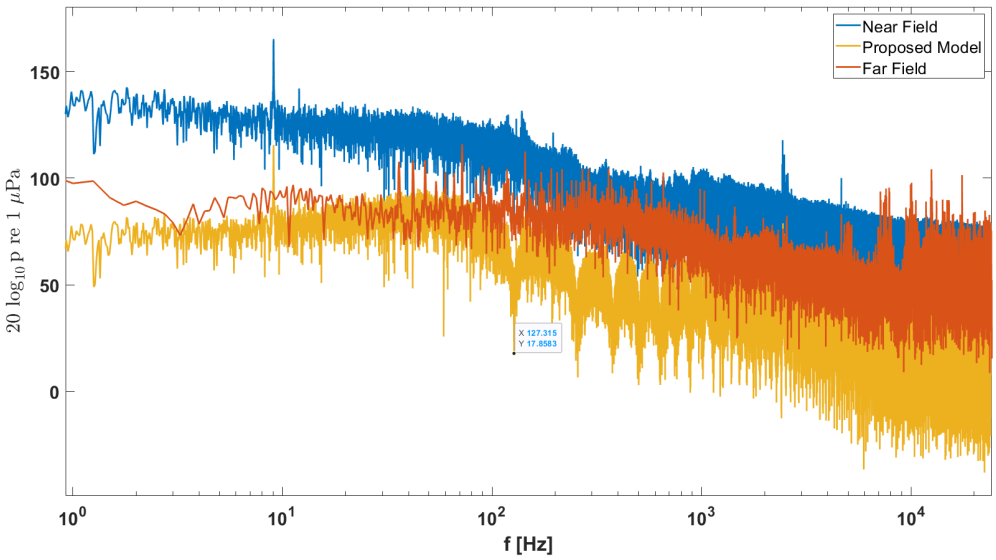


*Figure 4.16: Assumed Smallest Distance Between Near Field Pressure Sensor, Far Field Hydrophone, and Far Field Model Comparison. The 59-second interval is used for the hydrophone.*

as Lloyd mirror dips. To investigate possible sources of error, certain assumptions were examined, such as the sound speed. Equation 4.6 is dependent on the sound speed, and the first Lloyd dip frequency will increase with higher sound speed and vice versa. Therefore, a low ocean sound speed of 1450 m/s was used to calculate Eq. 4.6.

$$f = \frac{2\pi \cdot 1450 \text{ m/s}}{(|r_d - r_r|)2\pi} \approx 123\text{Hz}, \tag{4.7}$$

Equation 4.7 demonstrates that even with a very low sound speed, the frequency is still not close to the low-frequency dips observed in figure 4.16. Another possible factor contributing to the discrepancy could be imprecise distance measurements. In general, it is conceivable that the first Lloyd dip may not be observable in practice since the Lloyd mirror effect is a theoretical concept and does not account for time dependence. In a time-dependent environment, a Lloyd mirror dip would be smeared out due to non-constant distances, as shown in figure 2.6.

## 4.2 Far Field Study

One of the apparent deviations between the model and the far-field hydrophone is that the hydrophone signal contains a more significant amount of single-frequency components. To study these components, the SPL of the far field is plotted in figure 4.17. Earlier, the hydrophone data has only been plotted up until 24000 Hz, which is the near field Nyquist frequency [49]. However, the sampling frequency of the far field hydrophone is 256 kHz, which means that one could analyse up to the anti-aliasing filter. The cutoff frequency for the anti-aliasing filter looks to be around 10 kHz.

Around 50 kHz and 61 kHz, two frequency peaks are present. These peaks are not present in the figures with a max frequency of 24 kHz. To closely examine these frequencies, the DTFT.m is applied with a spectrogram. The frequency resolution is firstly 100 Hz to look for more specific frequencies. Then, the number of signal parts was increased because the relevant frequencies were as high as they were. The resulting amplitude and spectrogram are shown in

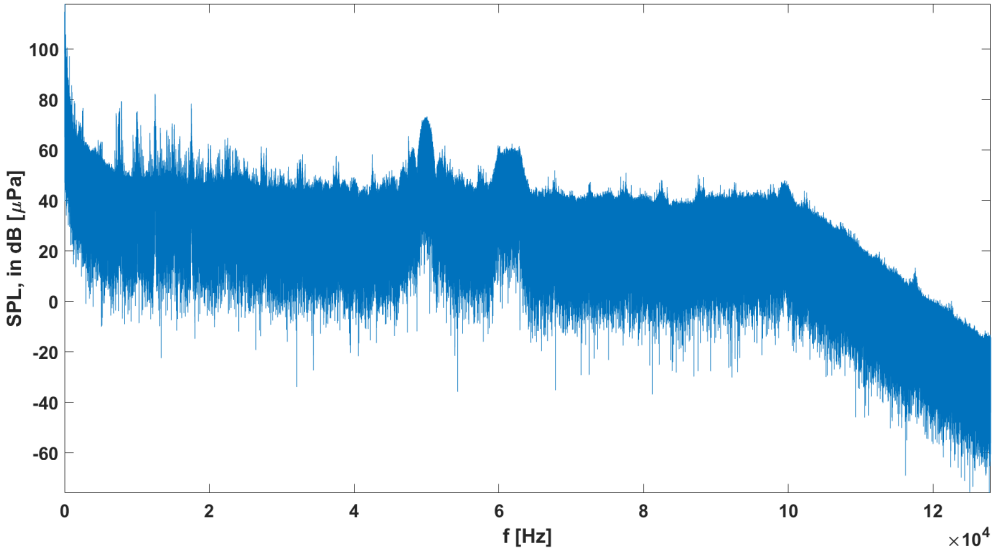


*Figure 4.17: Far Field Hydrophone PSD for run 9 for the frequency range 0-128 kHz.*

figure 4.18 and figure 4.19, respectively.

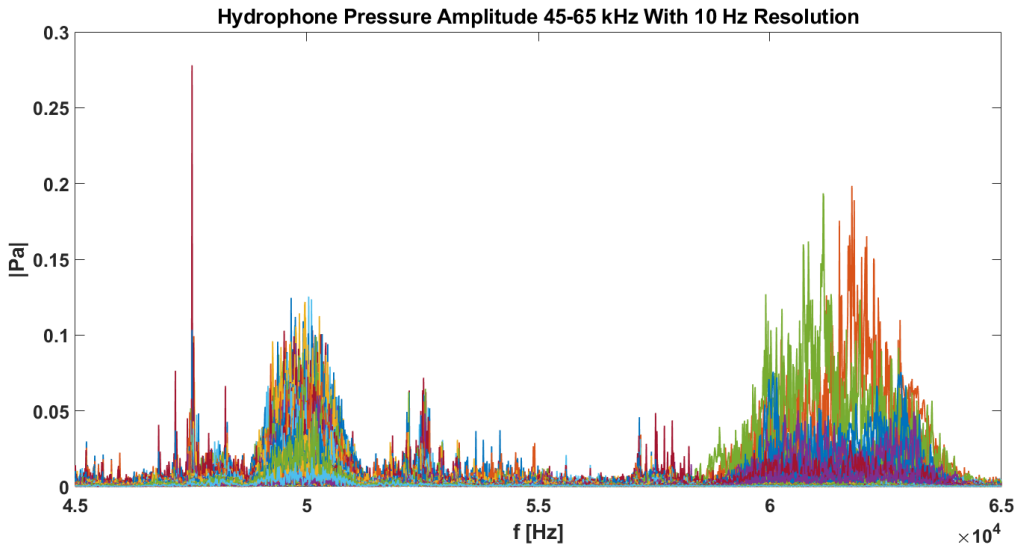


*Figure 4.18: Pressure amplitude of frequencies for run 9 in range 45-65 kHz with a resolution of 10 Hz*

As shown in figure 4.18, two areas have higher amplitude. There is also a peak at around 47.5 kHz after the 60Th second as seen in figure 4.19. figure 4.19 shows that the signal around 60 kHz looks like pings. It is assumed that the source of these pings is a SONAR. According to [22] high, frequency SONARs are within these frequency ranges. It could also look like the frequencies around 50 kHz also fluctuate concerning time. Therefore, the resolution is increased to 1 Hz to find a more explicit frequency peak, and an overlap of half the sampling frequency is also included to increase time resolution without data loss. Firstly, the frequency range of 48.5 - 51.5 kHz is analysed. The resulting spectrogram is shown in figure 4.20.
It seems like there is no explicit single frequency component, and there are slight signs of amplitude fluctuation.
Another interesting frequency is a mentioned the 47.5 kHz single peak. To look at this, a DTFT

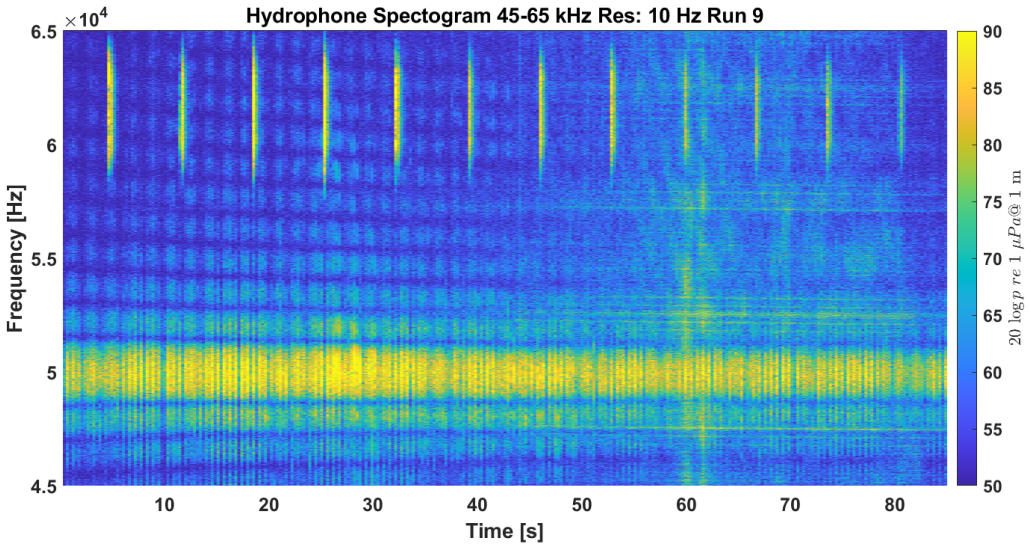


*Figure 4.19: Spectogram for frequencies for run 9 in the range 45-65 kHz with a resolution of 10 Hz*

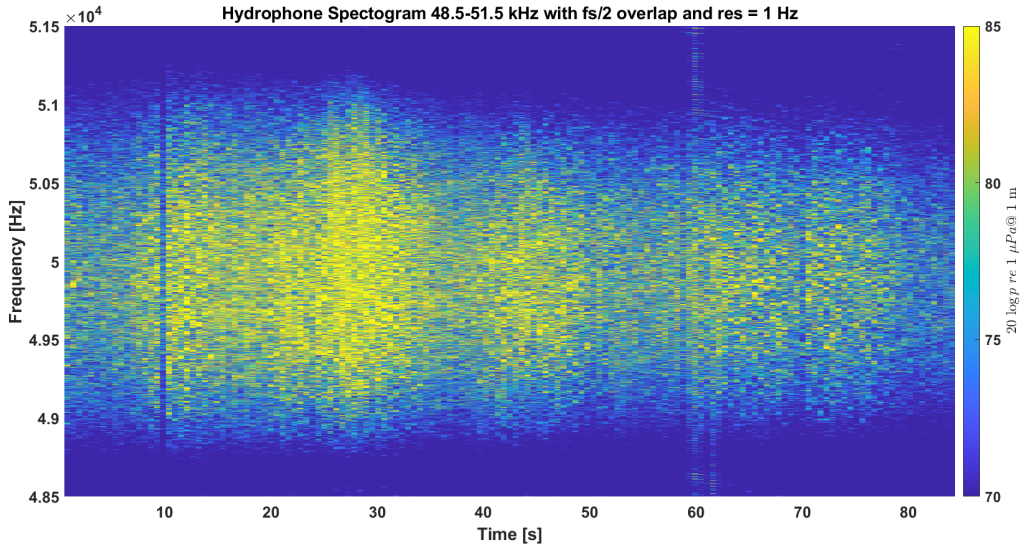


*Figure 4.20: Spectogram for frequencies for run 9 in the range 48.5-51.5 kHz with a resolution of 1 Hz with noverlap = 128000*

was done on the frequency band 47.4-47.8 kHz. The amount of signal parts was increased to 160, and the number of overlap samples was 128 samples given by $f_s/2$ which is a good overlap length to avoid data loss [50]. Resulting spectrogram is shown in figure 4.21

Figure 4.21 shows a similar effect as figure 4.12. A starting frequency of 47520 Hz was assumed to calculate a theoretical Doppler shift. The calculated Doppler shift fits well. This could confirm that the source of these frequencies is also the ship. An interesting result is that the moment when the assumed black line starting frequency of 47520 kHz crosses the assumed Doppler shift, is later than for earlier examined Doppler shift as in figure 4.12 even though it is the same run. The red line Doppler shift is delayed by 20 s, 5 seconds later than the 2454 Hz frequency studied in figure 4.12. It seems like the source is directive since the amplitudes are constantly higher after passing the hydrophone, relative to the earlier part of the signal.

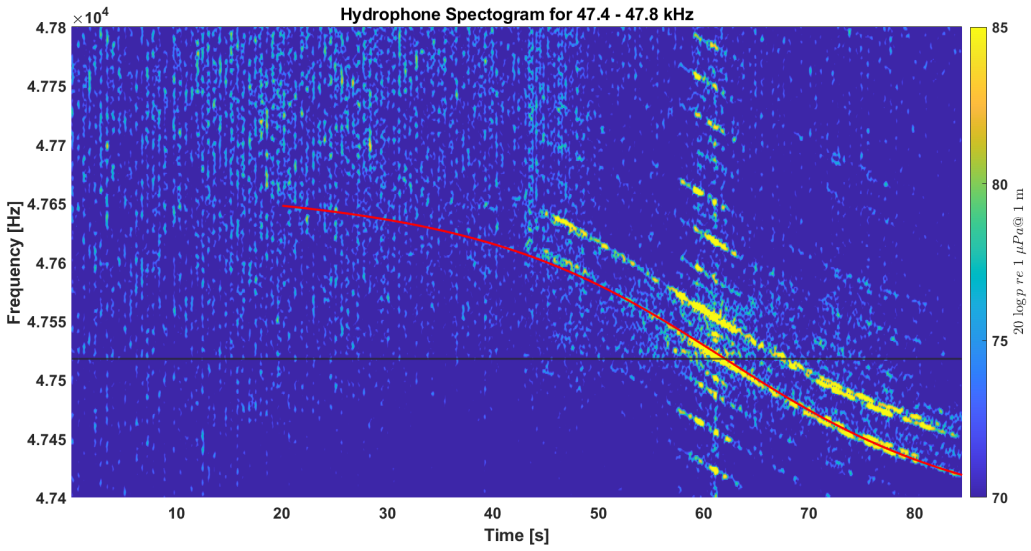


*Figure 4.21: Hydrophone Spectogram for frequency range 47.4 - 47.8 kHz. The number of overlap samples was 128 kHz (fs/2), and the number of DTFT was 160. Time resolution* $\approx 0.03s$

The last frequency band from figure 4.18 is between 57 - 65 kHz. There is clearly a fluctuating signal in this frequency band, with a time interval of around 5 s. Therefore, a spectrogram is made with no overlap but divided into 160 snippets. The frequency resolution is 1 Hz. The resulting spectrogram is shown in figure 4.22.

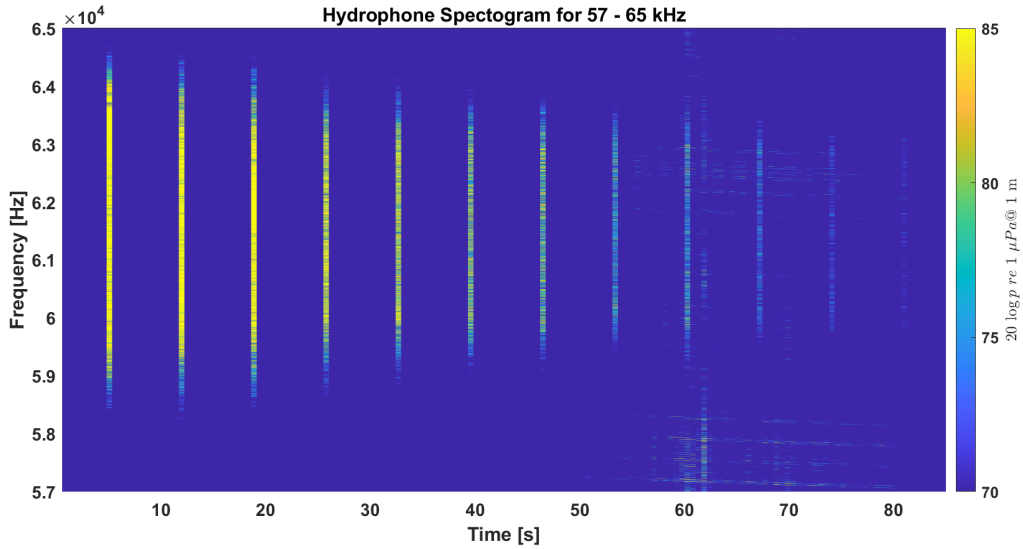


*Figure 4.22: Hydrophone Spectogram for the frequency range 57 - 65 kHz. The number of parts overlap samples was 0.53 s, and the number of DTFT was 160. Time resolution* $\approx 0.53s$

figure 4.22 shows clear pings with a length of 0.53 s. The pings at the beginning of the time signal seem to cover a larger frequency band, slowly decreasing towards the end of the signal. This is coherent with the amplitude also seeming to decrease as the frequency band is shortened. Therefore, higher frequencies have greater absorption than lower frequencies. This could indicate that the assumed SONAR is closer to the hydrophone in the beginning because the time amplitude decrease. To investigate the pulses, the time interval 4.5 - 5.5 s is analysed,

which was done by applying a high time resolution (0.01 s) spectrogram with a resolution of 1 Hz in the same frequency range as in figure 4.22. The result can be found in figure 4.23.

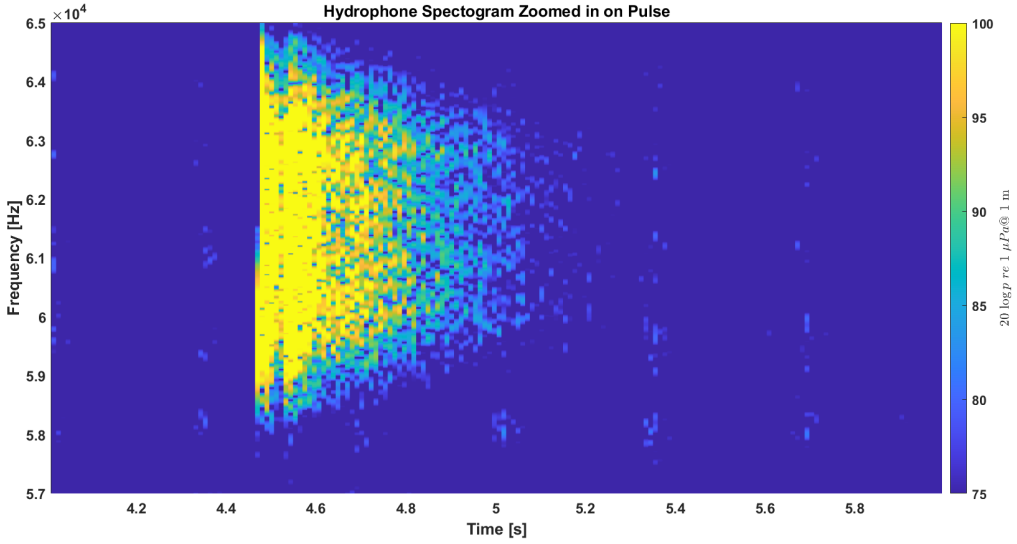


*Figure 4.23: Zoomed in spectrogram on the pulse. Time interval 4.5 - 5.5 s with high time resolution (0.01 s) with frequency range 57-65 kHz*

The pulse in figure 4.23 is approximately 0.5 s long and expresses a frequency bandwidth narrowing during that time. The amplitude is also strongest in the beginning before it slowly decays. One observation from figures 4.19, 4.21, and 4.23 is that there appears to be a notable rise in amplitude across a wide frequency range around the 60-second mark.

### 4.2.1 Far Field Harmonics

In figure 4.17, some spikes occur with a continuing distance. This is assumed to be some harmonic for a fundamental frequency. The frequency band 5-20 kHz has some relatively high tonal components. The pressure amplitude values in this frequency band are plotted in figure 4.24. This was done by using pwelch.m to find the pressure amplitude, with a frequency resolution of 1 Hz, over the whole time signal of run 9. Harmonics of the 2454 Hz were also plotted, which is the same frequency analysed in figure 4.12.
To highlight the difference between theory and practise, the assumed $f_0$ and 3rd, fifth and seventh harmonic is zoomed in on in figure 4.25
The harmonics in figure 4.24 do not match the frequency peaks, but the distance between the plotted harmonics and the peaks looks similar. Typically, harmonics are perfect multiples of a fundamental frequency. The harmonics will be perceived as all the frequencies within the Doppler shift if the whole time signal is used. For example, looking at figure 4.25, in the interval between 2200 - 2700 Hz, there are two peaks around the harmonic and a dip where the harmonic is expected. A Doppler shift is asymptotic, so a long-time signal relative to the Doppler shift will be perceived as two frequency peaks which large amplitude near each asymptote, whilst the original frequency will be in the middle between the two peaks with lower amplitudes. The frequency amplitude is a result of the power of the signal, which again is a function of time as described in 3.23. That's why the frequency near the asymptotes have larger amplitudes since they last longer relative to the frequency with $\Delta f = 0$.

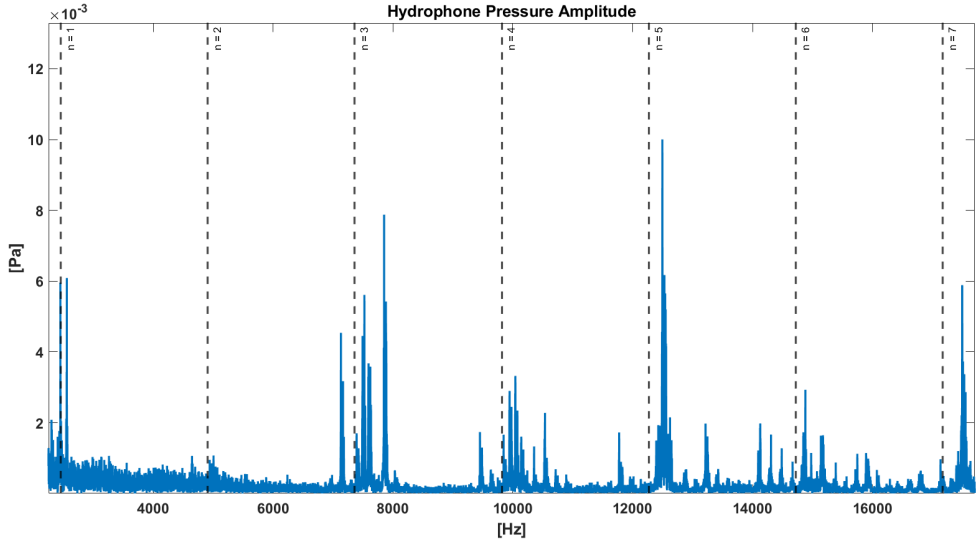


*Figure 4.24: Hydrophone Pressure amplitude with vertical n'th harmonics of fundamental frequency $f_0$ of 2454 Hz.*

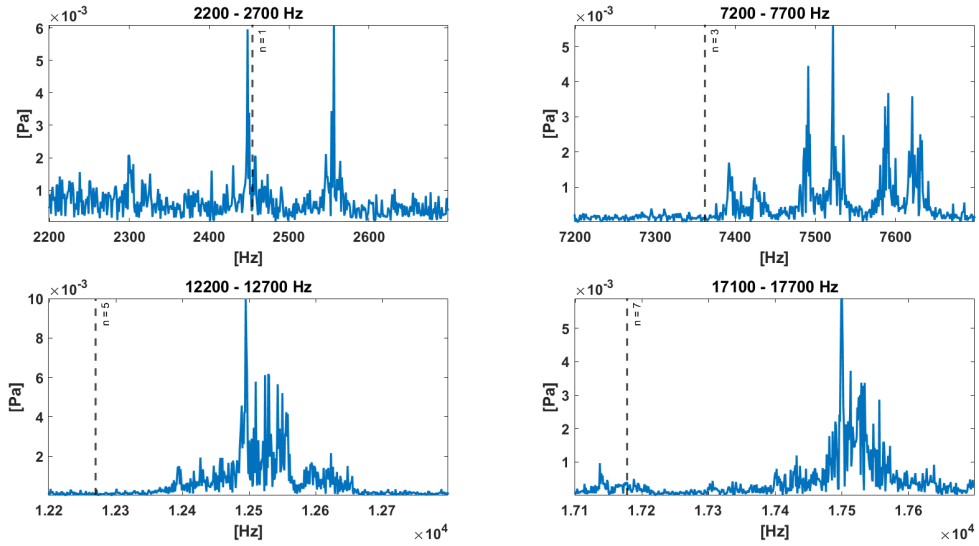


*Figure 4.25: Hydrophone SPL, zoomed in on $f_0$ and three n'Th harmonics.*

It is worth noticing that the frequency difference between the peaks increases with higher frequencies. To increase conformity, only a short time signal was used to narrow the frequency peaks. . Different frequencies that originate from the same source, has $\Delta f = 0$ at the same moment. Therefore the part of time signal where the frequency shift is zero, found to be 58Th second in figure 4.12, is plotted in the same frequency domain as in figure 4.24. The resulting plot is shown in figure 4.26.

By comparing figure 4.25 and figure 4.26, it is clear that figure 4.26 has lower SNR compared to figure 4.25. This could be because random noise averages out, increasing with the averaging time. As used in 4.25, a long-time signal will have enough time to average some of the noise out, while figure 4.26 is only based on one second, which will decrease noise averaging. The noise in figure 4.26 makes it hard to deduct or confirm any previous claims. Only the first fundamental frequency is slightly more correct than in figure 4.25.

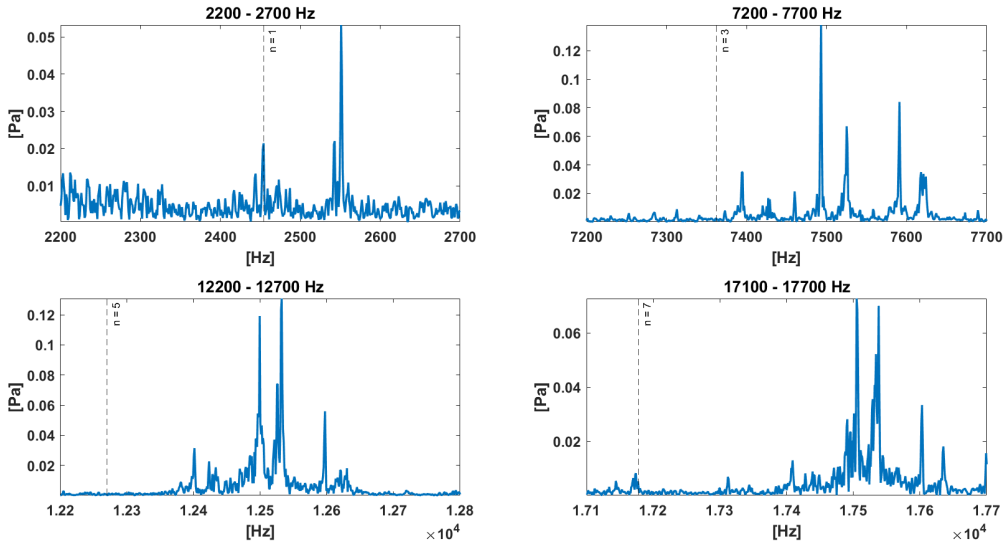


*Figure 4.26: Hydrophone SPL, zoomed in on $f_0$ and three n'Th harmonics, with only 58Th second*

To confirm that frequency spike pairs originate from Doppler shift asymptotes, $f_0$ and the fifth harmonic is plotted for the first 5 s, 56-62 s and the last 5 s. The expected result is that the highest frequency will be shown clearly for the first 5 s, the middle time window will have a slight peak on both spikes, and the low frequency will be prominent at the end of the signal. The absolute pressure amplitude is plotted instead of the SPL to minimise ripples. The resulting plot is plotted in figure 4.27.

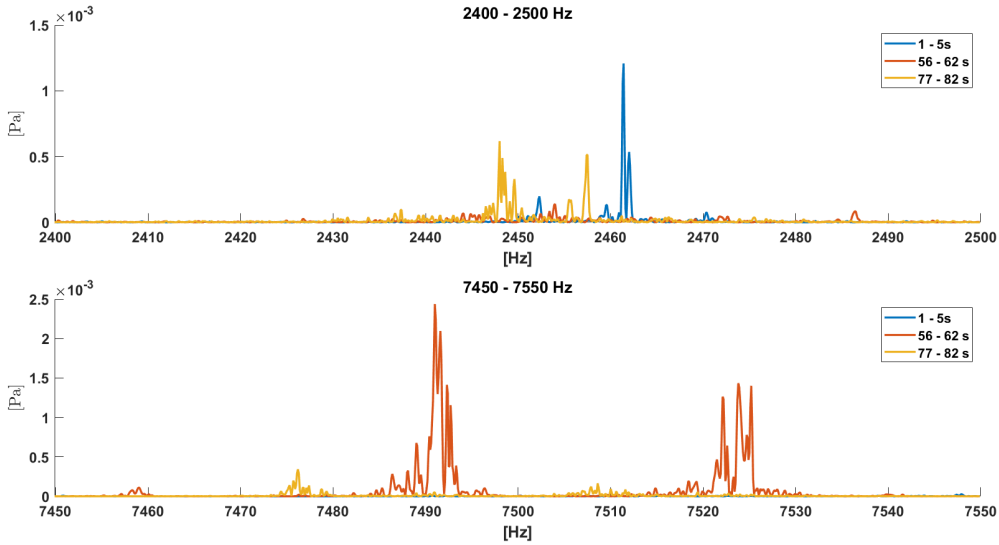


*Figure 4.27: Absolute pressure amplitude with three different time intervals.*

The amplitudes within the frequency range of 2400-2500 Hz, as shown in figure 4.27, exhibit a similar pattern to the results depicted in figure 4.12. As anticipated, the high frequency component is prominent in the initial 5 seconds of the signal, the central frequency $f_0$ of 2454 Hz is most pronounced in the middle of the signal, and the low frequency component becomes more prominent towards the end of the signal. However, for the higher frequencies, this trend is not as clear. The magnitudes in the middle of the signal are considerably larger compared to

the beginning and end for these higher frequencies.
In figure 2.5, one can see that a multiple of 200 Hz is predicted to have destructive interference, while multiples of 100 Hz will have constructive interference. This is a fair prediction while the boat is at the closest distance, discovered in the interval 58-62s. In figure 4.27, one can see that this could be why the orange graph has the lesser magnitude for the interval 2440-2460, which is close to the 20Th multiple of 200, 2400 Hz. The orange graph in the 7450 - 7550 Hz domain is close to the 25Th multiple of 100 Hz, which could explain why the orange graph is greater than the other graphs. To confirm this, the fundamental frequency 2545 and the 3rd, fifth and seventh harmonics were plotted as both waterfall plots and time pressure plots in figure 4.28, 4.29, 4.30, and 4.31,calculated and plotted with WaterfallforHarmoncis.m in Appendix A.

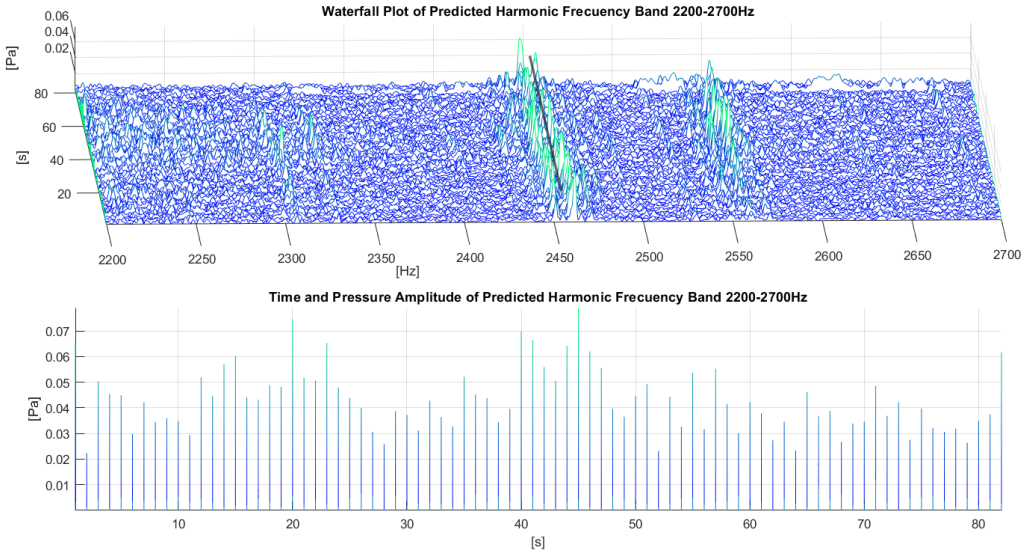


*Figure 4.28: Waterfall Plot of Predicted Harmonic Frequency Band 2200-2700 Hz and Time and Pressure Amplitude of Predicted Harmonic Frequency Band*

Then the predicted Lloyd effect was calculated, based on a single frequency of 2500, 7500, 12500, 17500 and the same method used in figure 2.6, except that the signal is delayed to comply with findings in 4.12. These frequencies are chosen because they are close to the frequency maximums of the above plots. The Lloyd mirror effect will behave similarly for the frequencies within the Doppler shift band, as shown in 2.5, making it satisfactory to use only single frequency components. Spherical loss and absorption are also included to include the distance variations. This result is plotted in figure 4.32.
The absolute response is based on an amplitude of 1, which means that figure 4.32 shows relative scaling values for a signal. All of the plots in figure 4.32 shows an oscillating amplitude with increasing amplitude towards the 60Th second. This do not comply with figure 4.28, 4.29, 4.30, and 4.31. Figure 4.28 shows similar patterns with two early peaks and an increase after the 80 s. However, figure 4.29 and 4.31, all have low amplitude with an increase in the 60Th second. For expected peaks fit well for the 7500 Hz and 17500 Hz prediction, but the 12500 Hz does not match the measured amplitude in figure 4.30, where there is a peak in real-life but destructive interference according to the calculations. One of the reasons for the differences between calculated and measured data could be if the Doppler frequency shift interferes with the Lloyd effect. The Doppler shift is a result of the time derivative of the

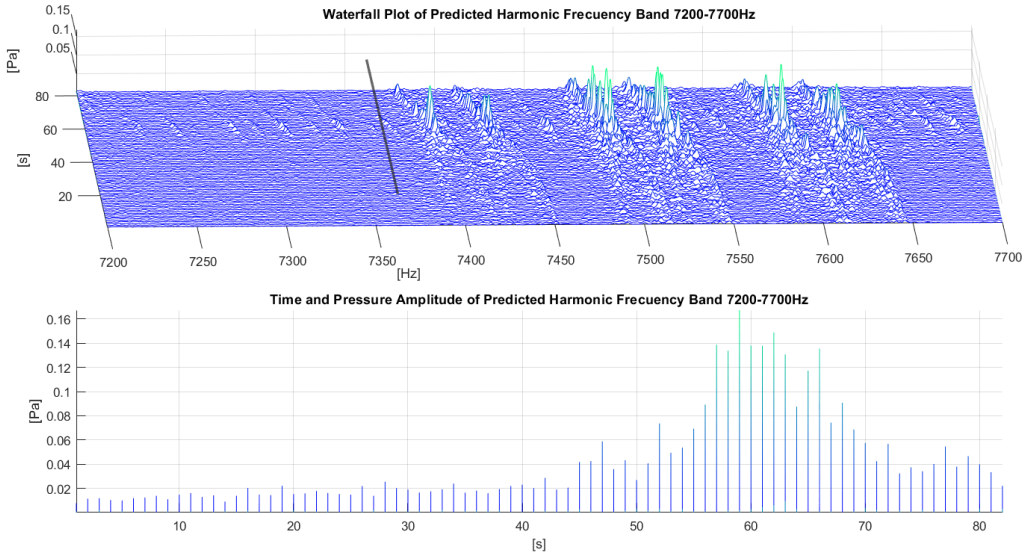


*Figure 4.29: Waterfall Plot of Predicted Harmonic Frequency Band 2200-2700 Hz and Time and Pressure Amplitude of Predicted Harmonic Frequency Band*

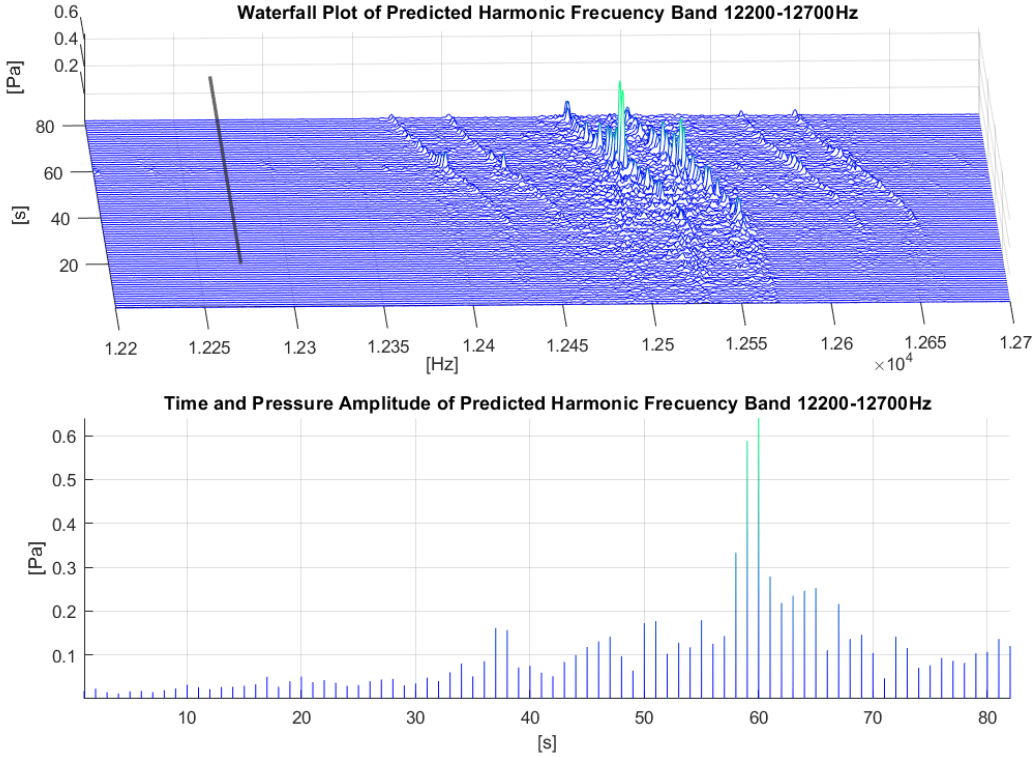


*Figure 4.30: Waterfall Plot of Predicted Harmonic Frequency Band 2200-2700 Hz and Time and Pressure Amplitude of Predicted Harmonic Frequency Band*

propagation path length. The time derivative of the propagation path length for the direct path differs from the reflected path. The Doppler shift for the directed and surface reflected sound wave is calculated to prove this. MATLAB-script LLoydandDoppler.m was used to calculate the difference between the Doppler shift $\Delta f_d$ and $\Delta f_d$ which is the Doppler shifts of the direct

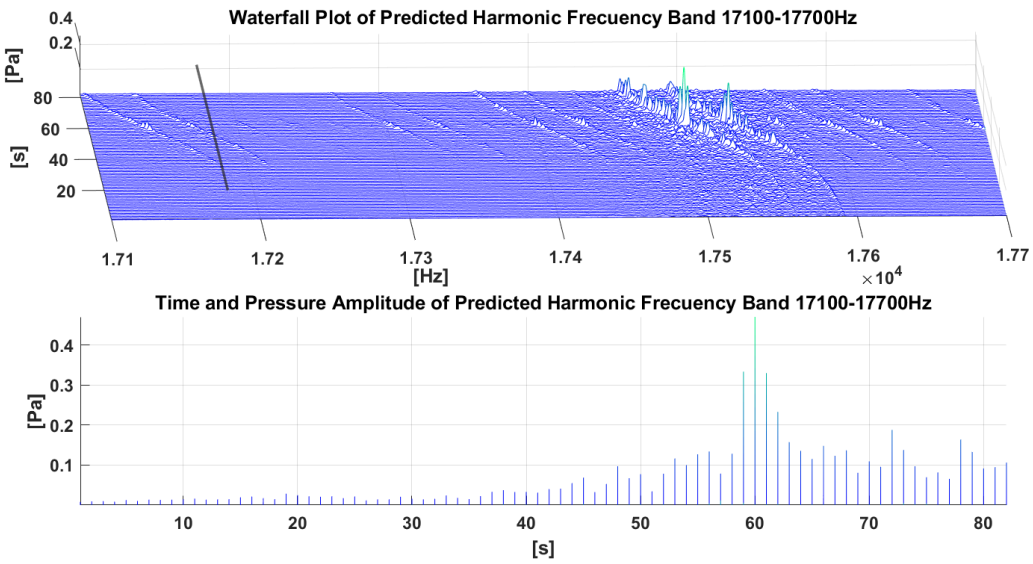


*Figure 4.31: Waterfall Plot of Predicted Harmonic Frequency Band 2200-2700 Hz and Time and Pressure Amplitude of Predicted Harmonic Frequency Band*

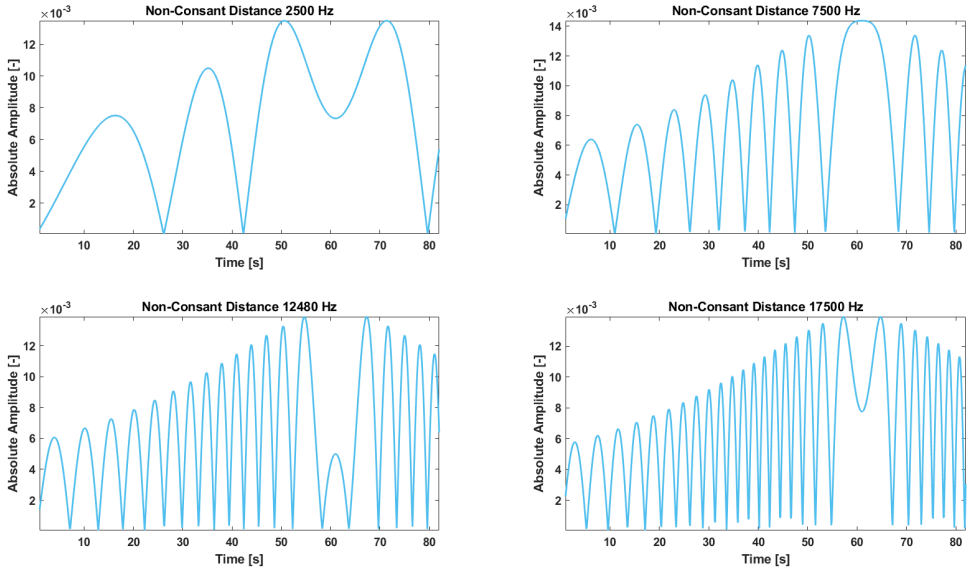


*Figure 4.32: 4 Lloyd mirror predictions based on frequencies 2500, 7500, 12500 and 17500.*

and reflected wave respectfully. This was done by calculating the derivative of the distances, and using the derivative as the velocity eq. 2.29. The result is plotted in figure 4.33.
As seen in figure 4.33, the difference in the Doppler shift is relatively small, it seems unlikely that the Doppler shift interfere with the Lloyd mirror effect.

Instead of using an assumed fundamental frequency to predict the harmonics, the frequency difference between some of the prominent peaks was calculated to see if the frequency difference could equal a fundamental frequency. Again, the 58Th second was used to avoid the Doppler shift as seen in figure 4.12. The reason why only the 58Th second was used, was to remove possible Doppler shift effects, and narrow the frequency peaks. As a result, the Lloyd

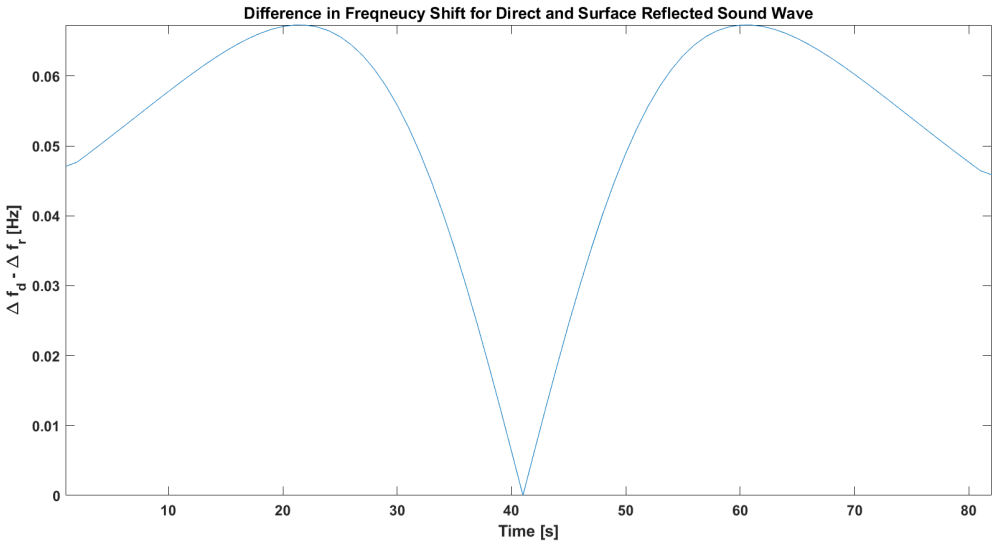


*Figure 4.33: The difference in Doppler shifts for direct wave $\Delta f_d$ and surface reflected wave $\Delta f_r$*

dips from figure 2.5 will apply. The result is shown in figure 4.34.

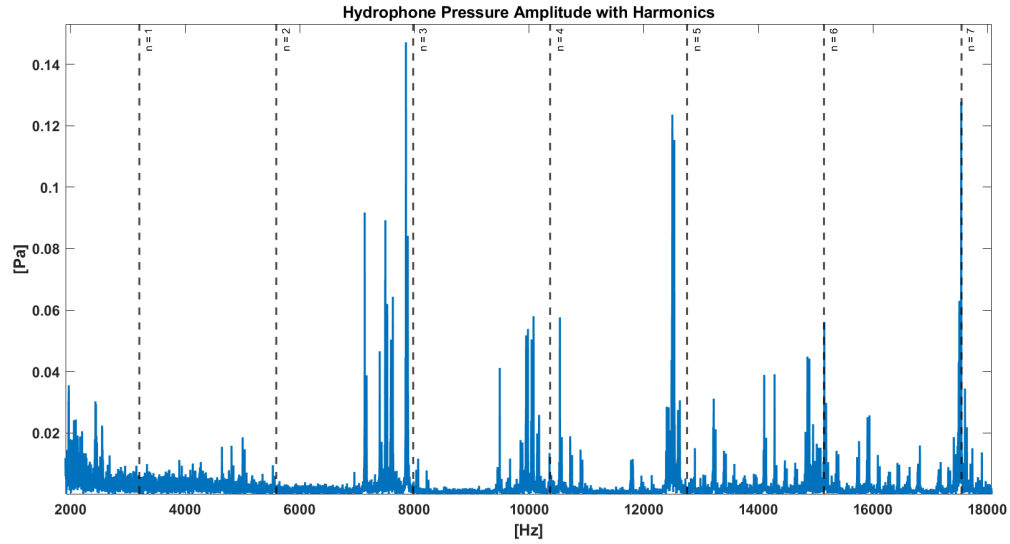


*Figure 4.34: Hydrophone Pressure Amplitude with vertical harmonics lines based on $f_0$ = 23900 Hz based on the frequency difference between peak at 17540 Hz and 15150 Hz.*

As seen in figure 4.34, there are no clear fundamental frequency, and the frequency difference is different between the tonal peaks.
Ripples in the frequency band between 0-300 Hz could also be fundamental frequencies and harmonics. The frequency band from 0-300 Hz was plotted to analyse this. For lower frequencies, the frequencies will have a lesser frequency shift. Therefore, the whole-time signal is used because this will lead to greater SNR. The result is plotted in figure 4.35.
Figure 4.35 shows some clear harmonics with a fundamental frequency of $f_0 = 6$ Hz, even though no peak is visible at 6 Hz. Generally, the fundamental frequency is expected to have a greater amplitude than its harmonics. For example, in figure 4.35, the 12Th harmonic of 72 Hz has a significantly greater amplitude than any of the other frequencies in the band, with the

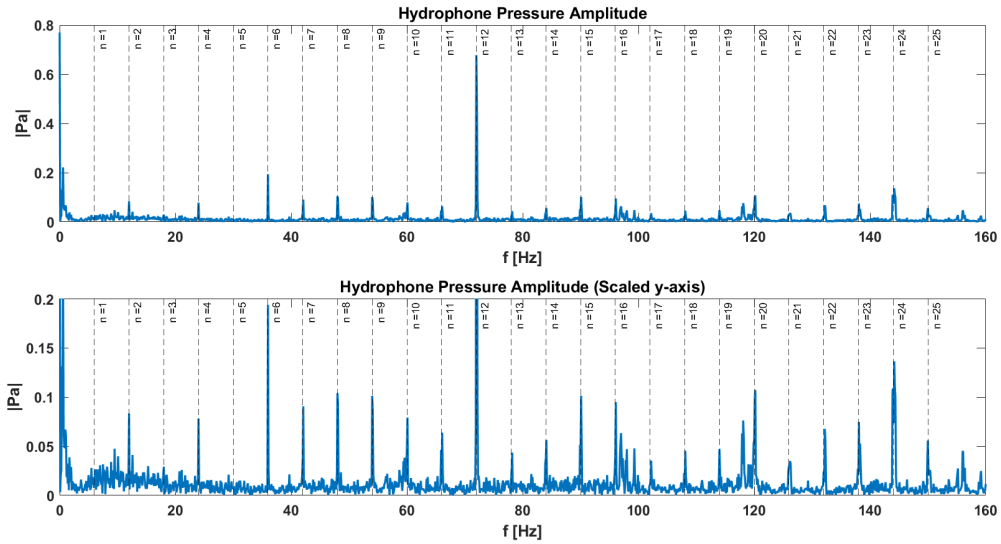


*Figure 4.35: Hydrophone Pressure Amplitude for whole Run nine-time signal, with black vertical 6 Hz harmonics.*

exemption of the DC component in the lowest frequencies.

## 4.3 Final Octave Band Comparison

The proposed model is described in 2.10.5. The general signal processing is shown in figure 3.21. The result is plotted in figure 4.36. All of the comparison in the following were plotted with the MATLAB script FinalComparison.m in Appendix A. Also the background noise (BGN) is plotted. This is measured with the hydrophone, without the ship is the vicinity.

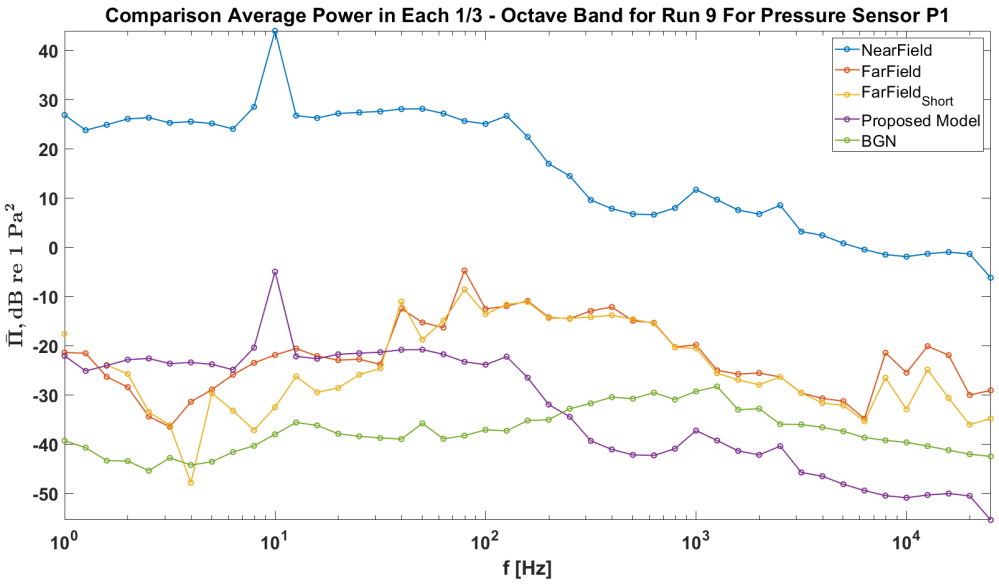


*Figure 4.36: Π for far and near field and model with both the whole time and the 58Th interval for the far field hydrophone.*

igure 4.36 shows how the proposed model compares to the far field measurements together

with a short snippet of the far field measurement. It also shows an example of how a snippet of the far field signal compares to the full far field signal. The proposed model seems to fit better with the hydrophone measurements for frequencies below 20 Hz, expect from the band containing $f_{bp}$ around 10 Hz.
The comparison between the different measurement methodologies of underwater noise from ships was then made. In section 2.1, multiple methods for describing the noise from ships are proposed. The general signal processing is described in 3.21.
All of the methods have slightly different methods of describing the transmission loss TL as seen in table 2.10.6. They differ in which losses they include, how the losses are described, the number of hydrophones and where they defined the acoustical centre location. The biggest difference between the methods is if they measure the far field SPL and use this to backtrack to SL or if they use near field SPL, backtrack to SL and then predict the URN. The same measurements have to be the base of the prediction to be able to compare them. It was therefore decided that the best way to compare them fairly was to use the near field pressure sensor measurements SPL for all the methods. To correct them equally, the SPL was backtracked to $L_s$ by using the distance between the propeller tip and pressure sensor, as described in Section 3.2.6 and figure 3.21. Also a correction of the rigid baffled transducer was implemented as described in Section

$$\mathrm{SL} = \mathrm{SPL} + 20\log_{10}(r_{dc}) - 6, \tag{4.8}$$

Note that this deviates from the acoustical centre of the different methods given in table 2.10.6. Again, this is done to be able to fairly compare the different propagation losses with each other. In reality, only the different TL in 2.10.6 was compared. The pressure sensor data was also corrected with a wav-correction of 111.3 dB as described in section 3.1.3. This value is accounted for in the SL, used in the following. Since all the losses for all the different models are given in pressure values, all of the TL's are converted to magnitude correction factors $L_c$ by

$$L_c = 10^{\frac{\mathrm{TL}}{10}}. \tag{4.9}$$

$L_c$ was then applied to the different power density spectrum S(f) values to apply the predicted loss. The far field measurement is also corrected for the sea bottom reflection, since the hydrophone is mounted close to the sea bottom. The far field hydrophone data $L_{hyd}$ is corrected for the sound that will reflect off the sea bottom, and interfere with the hydrophone signal since the hydrophone is omnidirectional. DNV's Silent E method used a correction factor of 5 dB, which also will be used in the following.
Firstly the ISO-17208 method transmission loss was calculated by $\mathrm{TL}_{\mathrm{ISO}} = \Delta L + 20\log_{10} r$ where $\Delta L$ is defined in eq. 2.38.

$$\mathrm{URN}_{\mathrm{ISO}} = \mathrm{SL} - \mathrm{TL}_{\mathrm{ISO}}. \tag{4.10}$$

The source distance in $\Delta L$ was calculated, in conformity with the ISO standard, the acoustical reference centre to be 0.7 of the ship draught transversely at the ship centre line, longitudinally, a quarter-length forward of the stern and vertically at the height of the sea surface. This model is based on an average of over three hydrophones. There is only one hydrophone in this case, so it is assumed that $L_s = L_{RN}$ from eq. 2.36.

DNV's method is described in section 2.10.2, and was applied as

$$\mathrm{URN}_{\mathrm{DNV}} = \mathrm{SL} - \mathrm{TL}_{\mathrm{DNV}}, \tag{4.11}$$

where $TL_{DNV}$ is

$$TL_{DNV} = 18 \log_{10} d \tag{4.12}$$

The distance d is defined as the same distance for ISO but without including the source depth. The simplified DNV measurement is described in eq. 2.41 and was applied as

$$URN_{DNV_{simp}} = SL + C_d - C_r \tag{4.13}$$

The distance used for the distance correction $C_d$ was defined as the CPA. This method is based on a near-field pressure sensor by default.

BV's model is also based on multiple hydrophones and a distance measurement for every 1 s. The distance to the acoustical centre should have been between the propeller and the motor. Since the ship utilises diesel-electric pod propulsion, the distance between the motor and the propeller is smaller than usual.. The result is

$$URN_{BV} = SL - TL_{BV}, \tag{4.14}$$

with a assumed observer depth of < 100 m, which makes the $TL_{BV} = 19 \log_{10} d$.

The last method uses only spherical spreading with the distance between the Hydropod and the propeller to calculate the SL. The Hydropod is not present in the measurement. For this comparison, the distance between the pressure sensor and the acoustical centre was decided to be the same as the above methods. This is different from the actual Hydropod method. The Hydropod URN was defined as,

$$URN_{Hydropod} = SL - TL_{HP}, \tag{4.15}$$

where $TL_{HP}$ is the hydropod TL, defined as the spherical spreading as defined in eq. 2.47.
The sound speed calculated in 2.6 as $c = 1491$ m/s. The resulting comparison for run 8 and pressure sensor P1, is shown in figure 4.37. As described in 3.2.6, the pressure levels above are converted to power levels for 1/3 - Octave band comparison. The octave levels is the sum of all the average powers of each frequency inside each band.
In the following a similar comparison as in figure 4.36 is done for all of the remaining the different pressure sensor for all the runs. The different runs are described in table 4.1. It is similar to table 3.2, but now also including the CPA and the assumed ship speed.

*Table 4.1: Overview of The Different Runs*

| Run | Hydrophone [s] | P1 [s] | P2 [s] | P3[s] | CPA [m] | Speed [kn] |
|---|---|---|---|---|---|---|
| 1 | 56.000 | 43.652 | 52.603 | 59.107 | 137 | 11 |
| 2 | 85.000 | 54.903 | 56.053 | 54.653 | 132 | 11 |
| 3 | 41.000 | 55.103 | 60.304 | 58.353 | 118 | 20 |
| 4 | 57.000 | 56.903 | 57.560 | 48.954 | 118 | 20 |

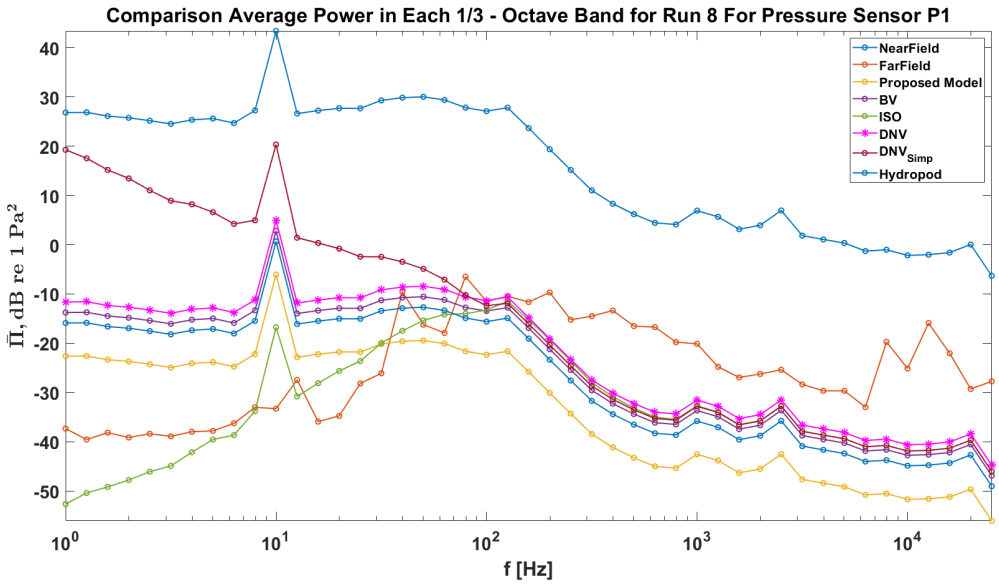


*Figure 4.37: Comparison Average Power in Each 1/3 - Octave Band for Run 8 For Pressure Sensor P1*

Run 8 is the first run, with a speed of 11 knots. Pressure sensor P1 is plotted in figure 4.37. The result for run 8 for P2 is shown in figure 4.38.

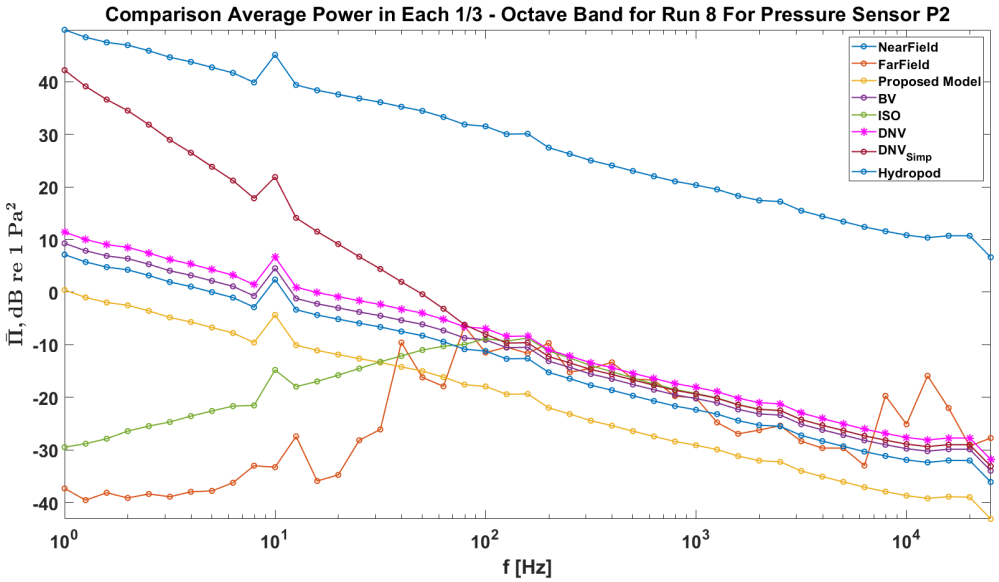


*Figure 4.38: Comparison Average Power in Each 1/3 - Octave Band for Run 8 For Pressure Sensor P2*

Figure 4.38 illustrates that the near field pressure measurements exhibit a considerably higher degree of linearity compared to P1, as observed in figure 4.37. Both figures indicate that the far field pressure sensor displays lower average Π levels, particularly below approximately 30 Hz. Subsequently, the far field hydrophone experiences a gradual increase until around 100 Hz, followed by a decrease at a similar rate as the other models. The disparity between the models in figure 4.37 and figure 4.38 is more pronounced than that between figure 4.37 and figure 4.39. Figure 4.39 represents the plot of Run 8 for pressure P3. In figure 4.39, the

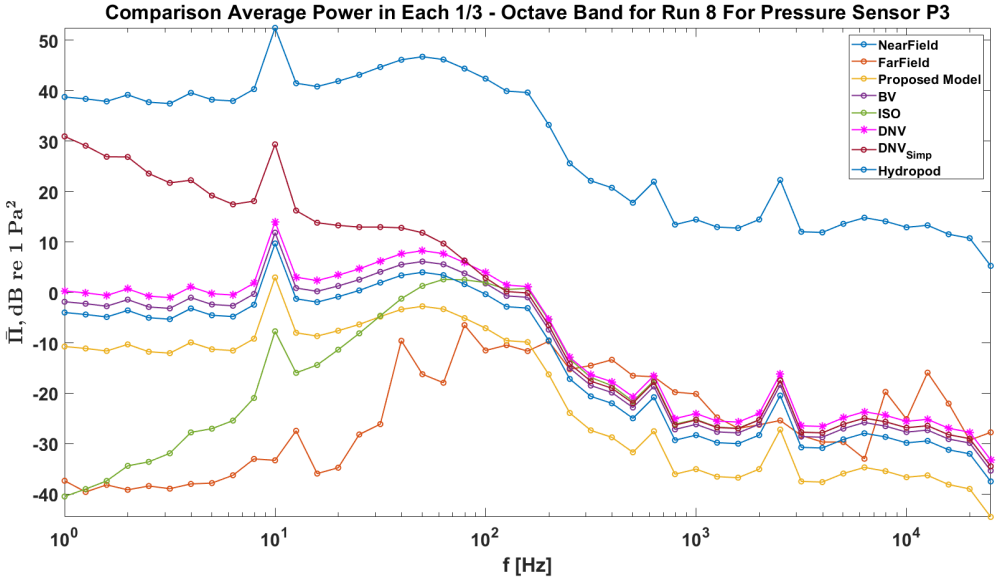


*Figure 4.39: Comparison Average Power in Each 1/3 - Octave Band for Run 8 For Pressure Sensor P3*

hydrophone measurements exhibit lower average power levels in the lower 1/3 - Octave bands.

However, there is an increase around 30 Hz, followed by a gradual rise until approximately 100 Hz. Comparing the near field measurements captured with pressure sensor P3 in figure 4.39 to those in figure 4.37, they appear more similar than the ones in figure 4.38. Additionally, another distinguishing factor between the various pressure sensors is the difference in their maximum power levels.
There are notable trends observed between runs 8-9 and runs 10-11, which are likely attributed to the speed difference during the runs. All of the runs which are not covered here, are plotted in appendix B, because the results are similar for the different runs. Table 4.2 provides details on the highest power levels for the band containing $f_{bp}$ for all the runs, presented in dB values relative to 1 $Pa^2$.

*Table 4.2: Overview of Highest and Average 1/3 - Octave Band Power Levels Given in*

| Run | $Hyd_{maxdB}$ | $P1_{maxdB}$ | $P2_{maxdB}$ | $P3_{maxdB}$ | Units |
|---|---|---|---|---|---|
| 8 | -6.49 | 43.42 | 49.87 | 52.42 | dB re $Pa^2$ |
| 9 | -4.72 | 43.94 | 58.16 | 52.57 | dB re $Pa^2$ |
| 10 | -0.65 | 51.50 | 56.70 | 61.23 | dB re $Pa^2$ |
| 11 | 1.33 | 51.47 | 56.80 | 61.59 | dB re $Pa^2$ |

One significant difference between runs 8-9 and runs 10-11 is the overall power levels. The power levels in runs 8-9 are lower compared to runs 10-11. It is important to note that these values represent the average power in each 1/3-octave band, which is calculated by summing all the PSD values. As explained in section 3.2.4 and illustrated in figure 3.18, the influence of noise becomes more prominent at higher frequencies in the 1/3-octave bands, thus affecting the average power level.
Table 4.2 reveals a similarity between run 8 and run 9, and equal similarity for run 10 and run 11. However, there is an intriguing observation regarding pressure sensor P2 in run 9, as it deviates from the overall trends. It exhibits similar maximum values to run 10-11, while the other sensors in run 9 align with the equivalent sensors in run 8.
Throughout all the runs, pressure sensor P1 consistently demonstrates the lowest maximum pressure levels, followed by either P2 in run 9 or P3 in the remaining runs. Since they are all positioned at the same distance from the source and properly calibrated, the power levels should ideally be closer to each other. Notably, the P2 sensor consistently exhibits significantly higher power levels in the frequency domain of 1 Hz to around 8 Hz. Another noteworthy observation in Table 4.2 is that P1 for runs 8 and 9 has considerably smaller average values compared to the other runs. While a difference in the maximum value can be attributed to the blade pass frequency ($f_{bp}$) and the ship's speed, this alone does not explain the disparity in average levels. It suggests that there may be additional processes associated with the ship's speed, apart from the blade pass.
Furthermore, there is curiosity regarding the peaks observed in the highest frequency 1/3-octave bands. All runs display a power increase at around 2 kHz. However, for the hydrophone, this power increase is noticeable only in runs 8 and 9. Additionally, runs 8 and 9 exhibit significant power increases in the bands around 10 kHz, whereas this increase is not visible in runs 10 and 11.
Another distinction between runs 8-9 and runs 10-11 is the frequency of the first significant peak. In runs 8-9, the first peak occurs around 9 Hz, whereas in runs 10-11, it is around 12 Hz. Furthermore, none of the runs show a consistent matching of the first significant peak between the pressure sensors and the hydrophone. These frequencies are presumed to be

associated with the blade pass frequency ($f_{bp}$). It is evident that $f_{bp}$ cannot be distinguished in the far field measurements. This finding concur with the single frequency analysis discussed in Section 4.1.

# Chapter 5

# Discussion

This thesis aims to propose a model for sound propagation from cruise ships using on-ship transducers pressure sensors and compare this method with a far-field transducer measurements. Additionally, a study of far-field measurements for a passing ship was conducted. Finally, a comparison was made between other similar sound propagation models.
The results indicate several differences between sound fields predicted from on-ship measurements and the observations made using a hydrophone in a fixed location. Furthermore, it highlights numerous considerations that must be considered when conducting ship noise measurements. This Section discusses these results, emphasising the importance of careful considerations in ship noise measurements.

## 5.1 Proposed Model

Results from the proposed model are plotted together with the near field and far field measurements in figure 4.1. The lowest frequency interval shows a significant difference between the proposed model and the far field measurements. This phenomenon can be attributed to the fact that the signal duration is relatively short, making it challenging to accurately resolve the lower frequency components. The limited duration of the signal affects the clarity of the lowest frequencies and may result in difficulties in accurately capturing their characteristics, as described in section 3.2.2 and seen in figure 3.12. Note that there are already declared uncertainty intervals for the pressure sensors and the hydrophones.

### 5.1.1 The blade-pass frequency $f_{\text{bp}}$

The assumed blade pass frequency $f_{\text{bp}}$ is clear for both the near field and also naturally for the proposed model. The blade pass frequency $f_{\text{bp}}$ does not appear clearly for any of the far field measurements, ref figure 4.1 and figure 4.37 - 4.39. As seen in table 3.1 there are uncertainties for the pressure sensor and hydrophone.

One possible explanation for the observed discrepancies could be attributed to the Lloyd mirror effect. In Section 4.1.2, it was unclear which frequencies would be clearly affected by destructive interference. However, according to the analysis in Section 2.5, frequencies up to a phase shift of $\frac{\pi}{2}$ are expected to experience destructive interference.The difference between the expected first Lloyd mirror effect and the observed results may be due to the idealized na-

ture of the Lloyd mirror model. The model assumes perfect interference with artificially sharp dips and a perfectly reflective sea surface. It also relies on a deep water approximation, which is not entirely accurate. However, these simplifications were made to ensure the ease of conducting the propagation model without the need for a detailed seabed description. Moreover, determining a precise distance between the source and the receiver can be challenging since the acoustic recordings are not synchronized with a common clock. While it may be difficult to precisely define the distance, the Doppler shift could have been used to calculate it accurately, as discussed in Section 2.9. Despite the Lloyd mirror effect being calculated based on assumptions and approximations, it is still considered a potential interference factor since the frequency range of interest $f_{bp}$ is relatively low. Although the acoustic measurements may not exhibit sharp minima as predicted by the theoretical Lloyd mirror effect, the effect can still be significant for frequencies lower than the cut-off frequency for destructive interference when the difference between $R_d$ and $R_r$ (the direct and reflected distances) is less than approximately a quarter of a wavelength.

Another reason could be that the proximity of the high and low-pressure regions generated by the propeller to the wavelength of the blade pass frequency hinders its effective propagation as an acoustic wave into the far field.
A last reason why the hydrophone don't experience the $f_{\text{bp}}$ as a sudden amplitude increase is that the hydrophone has low sensitivity for this frequency domain. As seen in [3], the OCVR values are defined from 10 kHz. It is not defined for lower frequencies. The hydrophone receiver sensitivity is shown in figure 3.4
In Figure 3.4, it can be observed that the hydrophone exhibits high sensitivity to frequencies ranging from 10 kHz to 20 kHz. However, whether the hydrophone is sensitive to the low frequencies of $f_{\text{bp}}$ is unclear. According to Ocean Sonics' website [51], the hydrophone is specified to have a frequency band of 10 Hz to 200 kHz, with a $\pm$3 dB bandwidth in the 10 Hz - 200 kHz frequency band. Consequently, the $f_{\text{bp}}$ falls below both the sensitivity frequency band and the manufacturer's claimed cutoff frequency of 10 Hz. A hydrophone sensitivity typically decreases suddenly below the cutoff frequencies, as seen in figure 5.14 in [25]. In short, the hydrophone sensitivity is unknown for under 10 Hz. From 10 Hz - 10 kHz it can be assumed to have a $\pm$3 dB flatness of the frequency response, according to manufacturer specifications. From 10 kHz - 200kHz, the sensitivity is declared in the calibration sheet [3]. This means that it is hard to claim anything about the 9 Hz $f_{\text{bp}}$ condition for run 8-9. For run 10-11, $f_{\text{bp}}$ falls within the manufacturer's frequency band. However, since the uncertainty is not disclosed, it becomes challenging to determine the precise values with certainty.

### 5.1.2 Harmonics

The proposed model, which is based on near field pressure sensor measurements, result deviates from the far field hydrophone in some other frequency domains. In particular, in three areas, harmonics of a fundamental frequency produce peaks in the far field hydrophone, but not for the pressure sensors.

Within the frequency range of 20 Hz to 100 Hz, a notable frequency domain exists where the model deviates from the far field hydrophone measurements. In the comparison plots for 1/3-octave band analysis, peaks are observed on the hydrophone readings. Figure 4.35 illustrates what appears to be harmonics of a 6 Hz fundamental frequency. Notably, significant peaks are observed at 38 Hz and 72 Hz in Figure 4.35, consistent with the 1/3-octave band comparison

plots.

Additionally, the uneven decrease in harmonic amplitudes is noteworthy, with the 38 Hz harmonic being smaller than the 72 Hz harmonic. As previously discussed, this could be attributed to the sensitivity of the hydrophone. The potential existence of a 6 Hz fundamental frequency is challenging to analyse since it lies outside the declared band pass of the hydrophone. The Lloyd mirror effect related to the lowest frequencies could explain why the 6 Hz fundamental frequency cannot be seen, similar to the possible reason why the $f_{bp}$ is not distinguishable in the far field data. Section 2.3 discusses how frequencies begin with destructive interference and gradually increase until reaching a phase difference ($\Delta\phi$) equal to $\pi$, which is around 63 Hz as shown in 2.4. This could explain why the 72 Hz harmonic exhibits a higher amplitude than the 38 Hz harmonic. These harmonics likely cause hydrophone peaks within this frequency range and may also contribute to the deviations between the proposed model and the far field in other frequency bands.
The subsequent frequency domains of interest lie within the range of 2000 Hz to 2500 Hz, as discussed in Section 4.2.1. Small peaks are also observed on the near field pressure sensors in this range. However, for run 8-9, more prominent peaks are present from 6 kHz to 20 kHz, which significantly deviate from the pressure sensor readings. These deviations are considered to be harmonics of the frequencies within the 2 kHz to 2.5 kHz frequency domain.
These frequencies are presumed to be the switching frequencies $f_{sw}$ mentioned in Section 2.2.2. Several reasons support this assumption. Firstly, as depicted in Figures 4.29 to 4.31, there are two dominant frequency amplitudes that clearly undergo a Doppler shift. This indicates that these frequencies originate from a moving source, which is likely the ship itself. Furthermore, two additional pairs of frequencies are observed alongside the main middle pair of frequencies. The difference between the middle peaks and their corresponding side peaks is consistently 100 Hz. Therefore, the author concludes that these side peaks represent the switching frequencies $f_{sw}$, as described in Section 2.4, where the emitted sound consists of the switching frequencies $f_{sw}$ and two times the line frequency ($2\tilde{f} = 100$ Hz) for a DC-motor as shown in eq. 2.4.
Another indication pointing to the correspondence of these peaks with the switching frequencies $f_{sw}$ is the presence of a rectangular pulse, where only odd harmonics should be present [52], as depicted in Figure 4.34. In this figure, the odd harmonics display high amplitudes, although some peaks are visible for even harmonics, which could be attributed to imperfections in the rectangular waveform.
As illustrated in the lower plot of Figure 4.28, the amplitude exhibits variations resembling the predicted Lloyd mirror effect shown in Figure 4.32. However, the resemblance between Figure 4.29 to 4.31 and the predicted Lloyd mirror effect for the corresponding frequencies shown in Figure 4.32 is less clear, and the reasons for this discrepancy are unclear. Additionally, it is noteworthy that the amplitude increases significantly when the ship is assumed to be closest to the observer. This observation further emphasises that calculating an average over the entire duration of an acoustic recording would reduce these amplitudes, regardless of the underlying cause.

It is worth noting, as discussed in Section 4.2.1, that the frequencies do not perfectly align as multiples of each other, as harmonics should do. The reasons for this discrepancy remain unclear. Both the Doppler shift and the Lloyd effect were explored as potential explanations, but they did not provide a definitive answer, except that the amplitudes were stronger when the source was closer. The reason why the switching frequency comes in pairs may be that there is

in fact two propellers on the ship. In all of the other parts of this thesis, the second propeller is ignored in conformity with the other noise measurements methods described in section 2.10. Even tough the switching frequency is not relative to propeller speed for DC-motors [19], it could be that the switching frequencies of the PWM's are slightly different.

### 5.1.3 Overall Comparison

In the 1/3-octave band comparisons, the discrepancy between the model and the far field model is consistent across some frequency domains. However, the specific frequency bands where the similarities occur can vary. For some runs and transducers, it is most similar in the high domains as for example, figure B.9 and figure B.2. For other like figure B.1 or figure B.4, they are most similar for the lower frequencies. In other words the results are not consistent.

Another important aspect for consideration is the type of noise that is of interest. Some could argue that the highest amplitude levels are the most crucial factor. When using a Fourier transform of the entire signal and averaging the results, the highest amplitudes are not reflected since they are attenuated through the averaging process.

## 5.2 Far Field Data Analysis

As shown in Section 4.2, a study of underwater far field measurements was done. This Section is related to only the far field signal itself. The far field data as a larger sampling frequency than the pressure sensor so it also has wider frequency band as seen in figure 4.2. The frequency amplitudes seems to be decreasing for 100 kHz. This is assumed to be a low-pass filter, that decreases the change of aliasing.

### 5.2.1 Doppler Shift

The Doppler shift was discussed in section 4.1.1. This Section, shows multiple exiting results. It started of as a way to find a distance assumption between the source and receiver. After analysing the plot, it turns out that it can be used for many things.

Figure 4.12 shows a theoretical Doppler shift which is intentionally delayed to align with the hydrophone signal. It appears that the Doppler shift can effectively determine the moment when the source is closest to the receiver. This suggests that the Doppler shift can be utilised to locate different sound sources along the length of the ship based on their respective Doppler shifts.
Figure 4.21 demonstrates that the closest point between the source and the receiver occurs at 60 seconds. However, in Figure 4.12, the closest point appears to be around 58 seconds. This discrepancy might indicate that these two signal do not share the same origin, challenging the notion of defining an acoustical centre that assumes all sound originates from a single location.

### 5.2.2 Time Signal Length

The assumed SONAR illustrated in Figure 4.22 exhibits high amplitudes at the beginning of the hydrophone recording, in contrast to the frequencies discussed earlier. This could suggest that either the assumed SONAR is positioned near the bow of the ship or that this phenomenon

is due to the directivity of the source and the hydrophone. It demonstrates the difficulty of relying solely on a small time snippets of hydrophone measurements, as different sources reach their maximum amplitudes at different times.

Using a small snippet of the signal poses another challenge related to vulnerability to mechanical disturbances. Certain hydrophones are sensitive to mechanical impacts that can affect their performance. In Figure 4.21, there is a noticeable broad-band noise component at the 60th second, that behaves differently from the other frequencies. This is likely the result of a mechanical impact on the hydrophone, such as being struck by an object or experiencing a shift in position. If the signal were shortened to, for example, the 58th to 60th second interval, this segment would capture the maximum values of certain frequencies. However, it would also amplify the effects of the assumed mechanical impact, making the noise levels appear significantly higher than they actually were. This highlights the importance of considering for potential mechanical disturbances when working with shortened time signals.
The use of the full-time signal also presents a challenge, as demonstrated in Figure 4.21. It is evident that there are minimal high amplitudes before the halfway point of the signal. If an average were to be calculated over the entire time signal, it would effectively decrease the actual amplitudes since only relatively low amplitudes are detected by the transducer until after the 42nd second.
Furthermore, Figure 4.21 could indicate the presence of either hydrophone or source directivity. It is possible that one of them exhibits a clear directional response, which results in the observed pattern in the spectrogram. Alternatively, it could be attributed to something being activated or turned on during the run, similar to the situation depicted in Figure 3.12 where a signal was introduced halfway through as described in eq. 3.17

## 5.3 Different Methods Comparison

The different methods used in this study, all described in section 2.10. Three methods, namely DNV's, BV's, and the Hydropod method, exhibit similar results with only minor differences in power dB values. When implemented as described in this thesis, they yield highly comparable outcomes. Additionally, $\text{DNV}_{\text{Simp}}$ shows a similar behaviour. All of these methods are considered to be relative similar to the hydrophone measurements in the frequency band from 2 kHz and above. One common characteristic among these methods is that they do not consider frequency-dependent losses. This approach has its own advantages and disadvantages.

On one hand, it is less theoretically accurate compared to methods that incorporate frequency-dependent sound propagation. It is well-established that sound propagation is influenced by the frequency of the sound waves. Frequency-dependent sound propagation in the ocean is a demanding and resource-intensive endeavour due to its reliance on various oceanic attributes. The complex nature of the ocean, including factors such as sound speed profiles, temperature gradients, salinity variations, and seabed characteristics, necessitates extensive data collection and analysis. Acquiring accurate and comprehensive information about these oceanic attributes can be both time-consuming and costly. In Appendix C, the proposed model is plotted with different sound speeds to showcase the varying outcomes associated with each sound speed setting. By plotting the model under different sound speed conditions, the corresponding effect of imprecise sound speed calculations and their implications become evident.
Therefore, conducting frequency-dependent sound propagation studies requires significant resources and expertise to account for the diverse and dynamic nature of the ocean environment.

One of the objectives of this thesis was to develop a simplified model that is more practical to use. In the propagation model, both absorption and the Lloyd mirror effect are frequency-dependent phenomena. To accurately calculate these mechanisms, various attributes of the ocean need to be determined. Since these attributes are assumed in the proposed model, there is a potential for increased uncertainty when incorporating the Lloyd mirror effect and sound absorption, depending on the accuracy of the assumed ocean attributes. This introduces a trade-off between simplicity and accuracy in the model, and it highlights the need to carefully consider the assumed ocean attributes when including these frequency-dependent effects. Arguably, including Lloyd mirror effect might add to the uncertainties rather than reduce them. The proposed model is more similar then the method above in the lower frequency band that the methods above, but is arguably the method with the largest deviation from the far field hydrophone.

The ISO method looks to the method which both follows the hydrophone in the lower frequency whilst behaving similar to the non-frequency dependent sound propagation models. Also since it only uses assumed distances, it removes the complications of assuming to many variables.

In the general, one could argue that there are some assumption already done in this thesis, that makes the comparison between a hydrophone far field and pressure sensors to be challenging. One incorrect assumption made in the analysis is regarding the distances involved. Although the CPA is determined based on laser measurements, it is incorrect to assume that this distance remains constant throughout the entire time signal. In reality, the ship is in motion, and the distance between the source and receiver continuously changes as the ship moves. Failing to account for this dynamic aspect can lead to inaccuracies in the analysis and interpretation of the results. To make a more accurate predicting the sound measurements could be calculated in for example shorter time interval's, with an assumed distance between source and receiver for each time interval.

Another assumed distance is the distance from the on ship pressure sensor to the propeller, denoted as $r_{\mathrm{dc}}$, which are assumed equal for all the pressure sensors. However, as noted in Section 4.2, the pressure sensors provide different readings for the same runs, indicating that the distances may not be the same. One possible explanation for this discrepancy could be the use of different brands of pressure sensors. Based on the analysis of the 1/3-Octave band comparisons discussed in Section 4.3 , it appears that pressure sensor P2 behaves differently from P1 and P3. P1 and P2 are logged as pressure sensors from Kistler, while P3 is from Piezotronics. It is plausible that P2 is actually the pressure sensor from Piezotronics. The varying pressure levels could be attributed to differences in the sensitivity of the pressure sensors. Nevertheless, the primary reason for the discrepancies is assumed to be the difference in distances between the pressure sensors, highlighting the insufficiency of assuming the same distance, $r_{\mathrm{dc}}$, for all sensors.

Another factor that has not been taken into account, as mentioned in Section 5.1 and 5.2, is the influence of other noise sources. The pressure sensor is located in close proximity to the propeller, making it challenging to determine the extent to which various noise sources affect the pressure sensor readings. In Section 4.2, it has already been noted that the assumed switching frequencies' higher harmonics are not visible on the pressure sensor. It is possible that there are additional similar frequencies that are not detected by the pressure sensor. One example

could be the additional noise generated by another propeller. The interference of the ship's other propeller with the hydrophone's signal is not discussed in this thesis. However, it is reasonable to assume that the contribution from another propeller could potentially increase the overall intensity by 3 dB, based on a perfect doubling of the intensity.

In this thesis, the background noise (BGN) is not accounted for. As depicted in Figure 3.18, the comparison method in this study is sensitive to noise. Many of the different methods discussed in Table 2.10.6 utilise multiple hydrophones or multiple runs, and subsequently average the results to reduce the impact of noise. It would have been beneficial to employ a similar approach in this comparison to mitigate the effects of noise.

# Chapter 6

# Conclusions and Future Work

## 6.1 Conclusions

This thesis focuses on the proposal and study for estimating underwater radiated noise using a hull-mounted pressure sensor. The proposed method with use of is then compared to measurements obtained from a far-field hydrophone. Additionally, comparisons are made between the proposed model and similar approaches for predicting far-field noise. Furthermore, the study also includes an investigation of general underwater noise characteristics.

The findings depicted in Figures 4.37 to 4.39 indicate a lack of alignment between the modeled far field near the hydrophone and the actual measurements obtained from the far field hydrophone. As discussed in Section 5.1, this discrepancy could be attributed to inaccurate assumptions and the influence of other noise sources on the hydrophone readings. A precise description of the acoustic field, including factors such as the sea bottom, sea state, and seawater properties, would be required to assess the model's performance.

For a comprehensive comparison across a wide frequency range, using 1/3-octave bands seems to be the most appropriate approach, taking advantage of the properties of Fourier transforms as discussed in Section 3.2.4. As proposed in Section 5.1, one potential method to enhance the comparison is to divide the signal into shorter durations, avoiding the assumption of a constant distance for the entire time signal. For high frequency tones the varying distances could be calculated based on the Doppler shift, such as the assumed $f_{sw}$ discussed in Section 4.1.1. This approach could also be employed to synchronise the different time signals for a more accurate comparison. Another solution could be the use of simple clock to synchronise the different data sets.

As discussed in Section 5.2.2, using the entire time signal has drawbacks. Some noise sources may not persist throughout the entire duration of the recording, but could significantly contribute to underwater noise levels. For instance, a SONAR might disappear when taking an average of the signal. This consideration also brings attention to the bandwidth of the pressure sensors. As demonstrated in Section 4.2, there are noise contributions beyond the bandwidth of the pressure sensors. This indicates the relevance of employing near-field sensors with a wider bandwidth. Moreover, it is evident from Section 4.2.1 that the hydrophones capture strong harmonics, while the pressure sensors do not detect these harmonics.

Finally, a comparison of the different methods was presented. As discussed previously, it is

challenging to determine which method is more "accurate." In addition to the reasons mentioned earlier, another factor contributing to this difficulty is the variation in pressure sensor levels for runs with the same speed.

It appears that for frequencies above 100 Hz, frequency independent models may be adequate. On the other hand, for frequencies below 100 Hz, the frequency-dependent propagation models seem to fit better. This observation could be due to the sensitivity of the hydrophone, as mentioned in Section 5.1. Furthermore, it is possible that the calculated Lloyd mirror effect in the proposed model and ISO's model coincidentally align with the sensitivity of the pressure sensor, thus resulting in a better fit for lower frequencies. In summary, while it is challenging to determine the absolute accuracy of the methods, the analysis suggests that different approaches may be more suitable depending on the frequency range considered.

## 6.2 Further Work

The presence of non-perfect harmonics of the assumed switching frequency ($f_{sw}$) is intriguing, as the Lloyd mirror effect or Doppler shift cannot solely explain it. Investigating the underlying reason behind this phenomenon would be interesting, as it could potentially facilitate the identification and confirmation of different harmonics and their resulting fundamental frequencies. If the fundamental frequencies can be accurately determined, reducing the amplitudes of their harmonics could decrease the underwater noise level. This is particularly important because the harmonics appear to dominate the hydrophone measurements, as shown in Figure 4.35. By targeting the fundamental frequency and implementing suitable noise reduction strategies, it may be possible to effectively mitigate underwater noise originating from the harmonics and its associated environmental impact.

Nevertheless, identifying the fundamental frequencies for harmonics is only sometimes feasible, even when clear harmonic patterns are present. In Figure 4.35, perfect harmonics of a 6 Hz frequency are visible, while the 6 Hz fundamental itself is not distinguishable. Exploring the underlying mechanics that give rise to the 6 Hz frequency and investigating why it is not detectable in the far field hydrophone data could be an intriguing study. Understanding the specific factors and phenomena responsible for this discrepancy could provide valuable insights into the complex nature of underwater noise propagation and measurement. Such investigations may contribute to improving the accuracy and reliability of noise analysis in underwater environments.

By utilising the proposed model, it is possible to develop a depth-dependent model for underwater radiated noise. This model could possible be employed to create a heat map representing the distribution of a ship's noise underwater. In regions with high ship traffic, it becomes feasible to calculate the overall noise intensity by summing up the individual intensities due to each ship. This calculation can be based on depth ranges that are relevant to specific marine ecosystems of interest. Such an approach enables assessing underwater noise levels and their potential impact on marine environments, facilitating informed decision-making and mitigation strategies in areas prone to significant ship noise.

# Bibliography


[1] "Phase diagram for water | ck-12 foundation," 7 2021 Accessed May 2023. https://flexbooks.ck12.org/cbook/ck-12-chemistry-flexbook-2.0/section/13.20/primary/lesson/phase-diagram-for-water-chem/.

[2] DNV, "Class guideline measurement procedures for noise emission," 2022.

[3] C. Ellis, "Certificate of calibration," 2021. Ocean Sonics, Great Village, Nova Scotia.

[4] C. M. Duarte, L. Chapuis, S. P. Collin, D. P. Costa, R. P. Devassy, V. M. Eguiluz, C. Erbe, T. A. Gordon, B. S. Halpern, H. R. Harding, M. N. Havlik, M. Meekan, N. D. Merchant, J. L. Miksis-Olds, M. Parsons, M. Predragovic, A. N. Radford, C. A. Radford, S. D. Simpson, H. Slabbekoorn, E. Staaterman, I. C. V. Opzeeland, J. Winderen, X. Zhang, and F. Juanes, "The soundscape of the anthropocene ocean," *Science*, 2021.

[5] J. Tournadre, "Anthropogenic pressure on the open ocean: The growth of ship traffic revealed by altimeter data analysis," *Geophysical Research Letters*, vol. 41, pp. 7924–7932, 11 2014.

[6] P. G. Brewer and K. Hester, "Ocean acidification and the increasing transparency of the ocean to low-frequency sound," *Oceanography*, vol. 22, pp. 86–93, 2009.

[7] H. B. Blair, N. D. Merchant, A. S. Friedlaender, D. N. Wiley, and S. E. Parks, "Evidence for ship noise impacts on humpback whale foraging behaviour," *Biology Letters*, vol. 12, 8 2016.

[8] K. de Jong, M. C. P. Amorim, P. J. Fonseca, C. J. Fox, and K. U. Heubel, "Noise can affect acoustic communication and subsequent spawning success in fish," *Environmental Pollution*, vol. 237, pp. 814–823, 6 2018.

[9] C. Erbe, S. A. Marley, R. P. Schoeman, J. N. Smith, L. E. Trigg, and C. B. Embling, "The effects of ship noise on marine mammalsa review," *Frontiers in Marine Science*, vol. 6, p. 606, 10 2019.

[10] Ángel Guerra, Ángel F. González, S. Pascual, and E. G. Dawe, "The giant squid architeuthis: An emblematic invertebrate that can represent concern for the conservation of marine biodiversity," *Biological Conservation*, vol. 144, pp. 1989–1997, 7 2011.

[11] A. N. Popper and M. C. Hastings, "The effects of human-generated sound on fish," *Integrative Zoology*, vol. 4, pp. 43–52, 3 2009.

[12] Anon., "Guidelines for the reduction of underwater noise from commercial shipping to address adverse impact on marine life.," 7 April 2014. International Maritime Organization.

[13] Anon., "Zero pollution and biodiversity: First ever eu-wide limits for underwater noise," 11 2022. Directorate General for Environment, EU.

[14] R. M. Heitmeyer, S. C. Wales, and L. A. Pflug, "Shipping noise predictions: Capabilities and limitations," *Marine Technology Society Journal*, vol. 37, pp. 54–65, 2003.

[15] P. Lunde, "Phys273 - marine acoustics syllabus, chapter 4: Noise and signal fluctuations." Department of Physics and Technology at The University of Bergen, 2021.

[16] D. Ross, *Mechanics of underwater noise*. Pergamon Press, 1976.

[17] B. Angell, "Cavitation damage," *Corrosion: Third Edition*, vol. 1, pp. 8:197–8:207, 2013.

[18] D. Wittekind and M. Schuster, "Propeller cavitation noise and background noise in the sea," *Ocean Engineering*, vol. 120, pp. 116–121, 7 2016.

[19] T. Gjestland , Personal Communication, May 2023.

[20] K. Belibassakis and G. Politis, "Generation and propagation of noise from cavitating marine propellers," 2019.

[21] D. A. Russell, J. P. Titlow, and Y.-J. Bemmen, "Acoustic monopoles, dipoles, and quadrupoles: An experiment revisited," *Citation: American Journal of Physics*, vol. 67, p. 660, 1999.

[22] A. O. Pedersen , Personal Communication, May 2023.

[23] P. Lunde, "Phys273 - marine acoustics syllabus, chapter 2: Underwater acoustic wave propagation." Department of Physics and Technology at The University of Bergen, 2021.

[24] L. E. Kinsler, A. R. Frey, A. B. Coppens and J. V. Sanders, *Fundamentals of Acoustics*. New York: J. Wiley & Sons, fourth edi ed., 2000.

[25] Xaiver Lurton, *An introduction to underwater acoustics. Principles and applications*. Springer and Praxis Publsihing, 2nd ed., 2010.

[26] C. C. Leroy, "Development of simple equations for accurate and more realistic calculation of the speed of sound in seawater related content development of metric for seawater quality seawater effects on cavitation noise development of simple equations for accurate and," *Surface Tension of Seawater Journal of Physical and Chemical Reference Data*, vol. 46, pp. 216–226, 1969.

[27] R. E. Francois, G. R. Garrison, J. C. Phys, and R. Francois, "Sound absorption based on ocean measurements. part ii: Boric acid contribution and equation for total absorption," *The Journal of the Acoustical Society of America*, vol. 72, pp. 1879–1890, 12 1982.

[28] M. Allaby, *A Dictionary of Geology and Earth Sciences - entry for Shadow Zone*. Oxford University Press, 5 ed., 1 2020.

[29] Anon., "Bureau veritas: Underwater radiated noise (urn)," 7 2018.

[30] B. Aktas, M. Atlar, S. Leivadaros, N. Sasaki, and P. Fitzsimmons, "Hydropod: An onboard deployed acoustic-visual device for propeller cavitation and noise investigations," 2019.

[31] Anon., "Water temperature in alesund (norway) in november," Accessed: May 2023. https://seatemperature.net/monthly/alesund-more-og-romsdal-norway-sea-temperature-in-november-1166.

[32] E. Jones, M. Chierici, I. Skjelvan, M. Norli, K. Børsheim, H. Lødemel, T. Kutti, K. Sørensen, A. King, K. Jackson, and T. de Lange, "Monitoring ocean acidification in norwegian seas in 2017 project manager for the contractor," 2018.

[33] M. Kartali, "Kistler calibration sheet." Kistler.

[34] J. Wojciechowski, "Pcb piezotronic, calibration certificate," Nov 11 2019.

[35] Anon., "Applying calibration to iclisten hydrophones iclisten background," 2020.

[36] "Fast fourier transform - matlab fft - mathworks nordic." https://se.mathworks.com/help/matlab/ref/fft.html, year = Accessed: May 2023,.

[37] A. M. Kabe and B. H. Sako, "Analysis of continuous and discrete time signals," *Structural Dynamics Fundamentals and Advanced Applications*, pp. 271–427, 2020.

[38] P. Schaldenbrand, "Windows and spectral leakage," Accessed May 2023. https://community.sw.siemens.com/s/article/windows-and-spectral-leakage.

[39] Anon., "Understanding ffts and windowing overview," National Instruments.

[40] K. M. M. Prabhu, *Window Functions and Their Applications in Signal Processing*. CRC Press, 9 2018.

[41] M. Cerna and A. F. Harvey, "The fundamentals of fft-based signal analysis and measurement," 2000.

[42] P. Schaldenbrand, "Window correction factors," 8 2019. Siemens.

[43] Anon., "Fft use in ni diadem." National Instruments Ireland.

[44] M. K. Saini, "Signals and systems energy and power signals," 11 2021 Accessed May.2023. https://www.tutorialspoint.com/signals-and-systems-energy-and-power-signals.

[45] A. N. S. Institute, "Ansi s1.11: Specification for octave, half-octave, and third octave band filter sets,"

[46] P. D. Welch, "The use of fast fourier transform for the estimation of power spectra: A method based on time averaging over short, modified periodograms," *IEEE Transactions on Audio and Electroacoustics*, vol. AU-15, pp. 70–73, 1967.

[47] M. H. M. H. Hayes, *Statistical digital signal processing and modeling*. John Wiley Sons, 1996.

[48] Anon., "Does the pwelch function provide unbiased estimation of the power spectral density? - matlab answers - matlab central," Accessed May 2023. bit.ly/3oI94ij.

[49] G. Wright, "What is the nyquist theorem?," 2022. https://www.techtarget.com/whatis/definition/Nyquist-Theorem.

[50] Anon., "Overlap: What, why and how to use it," Accessed: May 2023. https://community.sw.siemens.com/s/article/Overlap-What-Why-and-How-to-use-it.

[51] Anon., "iclisten rb9 - ocean sonics," Accessed May 2023. https://oceansonics.com/products/iclisten-rb9/.

[52] J. Stolet, "Electronic music interactive, 2nd edition," 5 Accessed May 2023. https://pages.uoregon.edu/emi/14.php.

# Appendix A

# MATLAB scripts

## A.1 LLoydExample

```
%% Signal
ls =1000;                   %Amount of samples
fs = 48000;                 %Sampling frequency
f = 0:1000;                 %Frequency intervall
fd = f./fs;                 %Digital Frequency
n = 0:1/fs:(ls-1)/fs;       %Samples

w = 2*pi*f;
c = 1491;                   %Sound Speed[m/s]
k = w/c;                    %Wavenumber

%Distances
CPA = 132;                      %Direct Distance
zs =  5;                        %Depth Source
zr =  40;                       %Depth Receiver
R_d  =  CPA;
D  =    sqrt(CPA^2+(zr-zs)^2);
R_r  =  sqrt((zr+zs)^2+D^2);    %Surface Reflected Distance

p0 = 1;                       %Amplitude
phase = k*R_d;                  %Phase
phase_reflected = k*R_r;
signal = zeros(length(f),ls);
signal2 = zeros(length(f),ls);

for i = 1:length(f)
signal(i,:) = p0.*exp(1i.*(- phase(i)));
signal2(i,:) = -p0.*exp(1i.*(- phase_reflected(i)));
end

figure(1)
hold on
plot(f,abs(phase-phase_reflected))
```

```
hold off
%%
figure(2)
for i = 1:length(f)
Amp(i) = max(signal(i,:)) + max(signal2(i,:));
end

plot(f,abs(Amp))
```

## A.2 Lloydeffectdistvar

```
%% Signal
f1 = [2500];
for m = 1:4
ls =1000;
fs = 48000;
f = f1(m);
fd = f./fs;
n = 0:1/fs:(ls-1)/fs;
fmax = f*1.2;
fmin = 0;
w = 2*pi*f;
c = 1500;     %[m/s]
k = w/c;

%% LLoyds
S = 35;      %ppt
d = 100;     %Density
T = 20;      %Temperature
%Distances
CPA = 132;                    %Horizontal Distance
zs =  5;                      %Depth Source
zr =  40;                     %Depth Receiver

tid = 1:0.1:82;  %Total Time Run 9
x = abs(205 - tid.* 410/82); %Perpenducular Distance
%%
avs =  sqrt(CPA^2 + x.^2);       %Direct Distance without
   depth
D   =  sqrt(avs.^2+(zr-zs)^2); %Closet Direct Distance with
   depth
D_r =  sqrt((zr+zs)^2+avs.^2);  %Surface Reflected Distance

%%
p0 = 10;
phase = k.*D;
phase_reflected = k*D_r;
```

```
signal = zeros(length(tid),ls);
signal2 = zeros(length(tid),ls);
S = 35;      %ppt
d = 100;     %Depth
T = 20;      %Temperature

alpha = absorption_francois_garrison(f/1e3,S,d,T); %dB/km [
   Francois & Garrison]
gamma = alpha/(8.686*1e3); % Neper/m


for i = 1:length(tid)
signal(i,:) = p0/D(i).*exp(-gamma*D(i))*exp(1i.*(f/fs*2*pi -
    phase(i)));
signal2(i,:) = -p0/D_r(i).*exp(-gamma*D_r(i))*exp(1i.*(f/fs
   *2*pi ...
    - phase_reflected(i)));
end

amp = signal + signal2;
figure(1)
plot(tid,abs(amp))

figure(2)
subplot(2,2,m)
plot(tid,abs(amp))
title(['Non-Consant Distance ',num2str(f),' Hz']);
clear amp
axis tight
xlabel('Time [s]')
ylabel('Absolute Amplitude [-]')

end
```

## A.3 spectralsmearing

```
%% Signal Definition

N =10e6;   %Amount of samles in signal
n = 0:N-1;

%Two different frequencies
f  = 2000;
f2 = 2006;

fmax = f2*1.1;
fmin = f*0.9;
```

```
12
13 fs = 256000;     %Sampling Frequency
14 fd = f./fs;      %Digital Frequencies
15 fd2 = f2./fs;
16
17 %Amplitudes for the sinusoids.
18 A = 1;
19 B = 3;
20
21 %Signal with noise
22 signal = A*sin(fd.*n.*2*pi);% + B*sin(fd2.*n.*2*pi);% + 1*
      randn(size(n));
23
24 fint = fmin:fs/length(signal):fmax;
25
26 %Window w
27 %w = ones(1,length(signal));
28 w = hanning(length(1:140))';
29 signal_snippet = signal(1:140);
30 signal_snippet_w = w.*signal_snippet;
31 signal_snippet_repated = [signal_snippet signal_snippet ...
32     signal_snippet signal_snippet];
33 signal_snippet_repated_w = [signal_snippet_w ...
34     signal_snippet_w signal_snippet_w signal_snippet_w];
35 figure(1)
36 subplot(2,1,1)
37 plot(signal_snippet)
38 xlabel('n')
39 ylabel('s(n)')
40 axis tight
41 subplot(2,1,2)
42 plot(signal_snippet_repated)
43
44 hold on
45 xline(140)
46 xline(280)
47 xline(420)
48 xline(560)
49 xlabel('n')
50 axis tight
51 ylabel('s(n)')
52
53 hold off
54
55 figure(2)
56 subplot(2,1,1)
57 plot(signal_snippet_repated)
58 xline(140)
```

```
59 xline(280)
60 xline(420)
61 xline(560)
62 xlabel('n')
63 ylabel('s(n)')
64 subplot(2,1,2)
65
66 axis tight
67 plot(signal_snippet_repated_w)
68 xlabel('n')
69 ylabel('s(n)')
70 xline(140)
71 xline(280)
72 xline(420)
73 xline(560)
74 axis tight
75
76 [Amp,fn] = DTFT_With_RectWindow(signal(1:3000),1,fs
      ,1600,2400,0.1,0)
77
78 [Amp_hanning,fn_hanning] = DTFT(signal(1:3000),1,fs
      ,1600,2400,0.1,0)
```

## A.4 DTFT

```
1  function [AMP,fn,tid] = DTFT(signal,nft,fs,fmin,fmax,res,
       noverlap)
2  %%
3  fn = fmin:res:fmax;    %Frekvens teller
4
5  df = fn/fs;
6  %Digital frekvens, kommer av omgjøring fra kon til disk tid.
       (nT_s)
7
8  %Gjør alle intervallene like lange ved å fylle på 0.
9  %%
10 %Hanning window over alle samplesene i fften.
11 n =1: round(length(signal)/nft);
12
13 ls = length(n);
14 AMP = zeros(nft,length(fn));
15 if ls < noverlap
16     error('Overlaps to much')
17 end
18 i = 0;
19 figure()
20 while 1
```

```
    i
    i = 1+(i);
    if length(signal((1+(i-1)*(ls-noverlap):end))) < ls
        tid =  (ls-noverlap)/fs: (ls-noverlap)/fs :(1+(i-1)
           ...
            *(ls-noverlap))/fs;
        break
    end
    %Dele på fs, hente ut av p1.
    p1 = signal((1+(i-1)*(ls-noverlap)):(ls+(i-1)*(ls-
       noverlap)));
    subplot(3,1,1)
    plot(p1)
    title('Signal Snippet')
    xlabel('n')
    ylabel('|Pa|')
    axis tight
    wind = hanning(ls);
    %Applying window
    p1 = p1 .* wind';
    %DTFT
    subplot(3,1,2)
    plot(p1)
    title('Applied Window')
    xlabel('n')
    ylabel('|Pa|')
    axis tight
    Amp = zeros(1,length(df));
    for l = 1:length(df)
    Amp(l) = sum( p1.*exp(-1i*2*pi.*df(l).*n))/ls;
    end
    AMP(i,:) = Amp*2*2;
    subplot(3,1,3)
    plot(fn,abs((AMP(i,:))) );
    hold on
    title('Frequency Amplitude Respons')
    xlabel('f [Hz]')
    ylabel('|Pa|')
    axis tight
end
hold off
```

## A.5 SpectrogramDTFT

```
load('Runs_wNearfield_timeseries.mat');
%%

```

```
run = 9;     % Runs between 8-12
Naerfelt = Runs(run).signal; %  Extracts data.

fs = 256000; %Sampling Frequency

nfft =80;     %Number for nfft and how many snippets.
res =1;       %Hz Resolution
fmin = 2400; % fmin and fmax is the dtft frequency band
   width.
fmax = 2520;
noverlap = round(fs/4); %Decides the overlap .
%Runs DTFT2. Output is Amplitudem, Frequency and Time
[Amp,fn,time] = DTFT(Naerfelt,nfft,fs,fmin,fmax,res,noverlap
   );
%%
AmpDB = 20*log10(abs(Amp/sqrt(2))/(10^-6));  %Calculate the
   DB value.

%Optional to find the highest mean amplitude in nearfield.
[maxamp,i] = maxk(mean(AmpDB),1);
%Calculates DopplerShift
[hydfreq,tdp] = Hastighettilskip(2454,time,Runs(run).CPA);
%% Makes Spectogram using pcolor.
figure();
pcolor(time,fn,abs(Amp'));
ylabel('Frequency [Hz]')
xlabel('Time [s]')
shading flat
colormap('jet')

hold on

% plot(hydfreq,'r','linewidth',2
% pause
tdp = tdp +15;
plot(tdp,hydfreq,'r','linewidth',2)
yline(2454,'linewidth',2)
```

## A.6 octavetestpwelch

```
N =10e7;
n = 0:N-1;
f= 1000;
f2 = 2006;
fmax = f2*1.010;
fmin = f*0.990;
fs = 256000;
```

```
fd = f./fs;
fd2 = f2./fs;
A = 2;
B = 3;
signal = A*sin(fd.*n.*2*pi) + B*sin(fd2.*n.*2*pi) + 1*randn(
   size(n));
w = hanning(length(n))';
w = ones(1,N)';
%w = ones(1,N);
%%
time_domain_power = sum(abs(signal).^2) *1/(length(signal))

noverlap = 0;
fref = 10.^(0.1.*[7:55]);
%fref  = 10^3 * (2 .^ ([-23:13]/3))
freq_indx = @(f) floor(f*N/fs +1);

bands_avg_power = zeros(1,length(fref)-1);
[psd,f_psd]= pwelch(signal,w, noverlap,N,fs,'psd');
df = fs/N;
flower = fref(1)/(2^(1/6));
for i = 1:length(fref)
    cf = fref(i);
    fupper = cf * (2^(1/6));
    indx = freq_indx(flower):freq_indx(fupper);
    %Avg I Tidsdomenet.
    try
        bands_avg_power(i) = sum(psd(indx)*df);
    catch
        bands_avg_power(i) = sum(psd(indx(1):end)*df );
    end
    flower = fupper + df;
end

subplot(2,1,1)
plot(fref,bands_avg_power,'o')
subplot(2,1,2)
power_freq_psd = sum(psd)*df
power_freq_psd_oct = sum(bands_avg_power)
```

## A.7 PWRPSDtestfft

```
%% Signal Definition

N =30e6;   %Amount of samles in signal
n = 0:N-1;

```

```
%Two different frequencies
f  = 2000;
f2 = 2006;

fmax = f2*1.1;
fmin = f*0.9;

fs = 256000;    %Sampling Frequency
fd = f./fs;     %Digital Frequencies
fd2 = f2./fs;

%Amplitudes for the sinusoids.
A = 2;
B = 3;

%Signal with noise
signal = A*sin(fd.*n.*2*pi) + B*sin(fd2.*n.*2*pi);% + 1*
   randn(size(n));

fint = fmin:fs/length(signal):fmax;

%Window w
%w = ones(1,length(signal));
w = hanning(length(n))';

signal_win = signal .* w;

%% Periodogram
%Fast Fourier Transform. Return the DFT
xf = fft(signal_win);

%fft.m return the twosided frequncy spectrum.
% Transform to one-sided spectrum.
xf_twosided = abs(xf/N);
xf = xf_twosided(1:N/2+1);
xf(2:end-1) = 2*xf(2:end-1);
xf = xf*2;
df = fs/N;      % fft frequency resolusion df

f = 0:fs/length(signal):fs/2;       %Frequency Vector


psd = abs(xf).^2/2/df;              %PSD
powerspec = abs(xf).^2/2;           %Power Spectrum


xf_dB = 20*log10(xf);
psd_dB = 20*log10(psd);
```

```
53 powerspec_dB = 20*log10(powerspec);
54
55 %% Parsavels
56
57 freq_indx = @(f) floor(f*N/fs +1);
58 duration = length(signal)/fs;
59
60 time_domain_power = sum(abs(signal).^2) *1/(length(signal))
61
62 freq_domain_power = sum(psd)*(fs/length(signal))
63
64 %% Plots
65 indx1 = freq_indx(fmin/0.9*0.9995):freq_indx(fmax
      /1.1*1.0005);
66 indx2 = freq_indx(fmin/0.9*0.995):freq_indx(fmax/1.1*1.005);
67 figure(1)
68 subplot(2,1,1)
69 hold on
70 plot(f(indx1),psd(indx1))
71 xlabel('Frequency [Hz]')
72 ylabel('PSD of S(f) [W/Hz]')
73 grid on
74 axis tight
75 subplot(2,1,2)
76 hold on
77 plot(f(indx1),xf(indx1))
78 xlabel('Frequency [Hz]')
79 ylabel('Magnitude |S(f)|')
80 grid on
81 axis tight
82
83
84 figure(2)
85 subplot(2,1,1)
86 plot(f(indx2),psd_dB(indx2))
87 xlabel('Frequency [Hz]')
88 ylabel('PSD in dB [dB/Hz] |S|')
89 hold on
90 grid on
91 axis tight
92 deltaf = fs/N;
93 subplot(2,1,2)
94 plot(f(indx2),xf_dB(indx2))
95 hold on
96 xlabel('Frequency [Hz]')
97 ylabel('Magnitude |S(f)| [dB] |S|')
98 grid on
99 axis tight
```

## A.8 pwelchtest

```
% Signal. Applies hanning window. pwelch with power and PSD.


N =10e7;
n = 0:N-1;
f= 2000;
f2 = 2006;
fmax = f2*1.010;
fmin = f*0.990;
fs = 256000;
fd = f./fs;
fd2 = f2./fs;
A = 3;
B = 2;
signal = A*sin(fd.*n.*2*pi) + B*sin(fd2.*n.*2*pi);% + 1*
   randn(size(n));
w = hanning(length(n))';
%w = ones(1,N);
%signal_win = signal .* w;
%%


noverlap = 0;
f = 0:fs/length(signal):fs/2;
freq_indx = @(f) floor(f*N/fs +1);

indx = freq_indx(fmin):freq_indx(fmax);
df = fs/N;
[psd,f_psd]= pwelch(signal,w, noverlap,N,fs,'psd');
[power,f_power]= pwelch(signal,w, noverlap,N,fs,'power');
sf = sqrt(power*2);

% In dB
psd_db = 20*log10(psd);
sf_db  = 20*log10(sf);
%%
figure(1)
subplot(2,1,1)
plot(f_psd(indx),psd(indx))
xlabel('Frequency [Hz]')
ylabel('PSD of S(f) [W/Hz]')
grid on
axis tight
subplot(2,1,2)
plot(f_power(indx),sf(indx))
xlabel('Frequency [Hz]')
```

```
ylabel('Magnitude |S(f)|')
grid on
axis tight

figure(2)
subplot(2,1,1)
plot(f_psd,psd_db)
subplot(2,1,2)
plot(f_power,sf_db)



%%
time_domain_power = sum(abs(signal).^2) *1/(length(signal))

freq_domain_power = sum(psd)*(fs/length(signal))
```

## A.9 FinalComparisonAllFreq

```
%% The Data
load Runs_wNearfield_timeseries.mat
%% Run General

run = 9;
psens = 'P1';
NearField =Runs(run).p1;
FarField = Runs(run).signal;
FarField_BGN = Runs(7).signal;
FarField_BGN = FarField_BGN(1:length(FarField));

CPA = Runs(run).CPA;
fs_n  = 48000;
fs_f  = 256000;

noverlap = 0;
ns = 2;          %Number of sample periods.
time_ff = 59;      %Part of signal extraxted in second.

FarField_Short = FarField(fs_f*time_ff:fs_f*time_ff+ns*fs_f)
   ;
FarField_BGN_Short = FarField_BGN(1:length(FarField_Short));

c = 1491;
N_F  = length(FarField);
N_FS = length(FarField_Short);
N_N  = length(NearField);

```

```
wind_n =  hanning(N_N);
wind_f =  hanning(N_F);
wind_fs = hanning(N_FS);

% wind_n =  ones(1,N_N) ;
% wind_f =  ones(1,N_F) ;
% wind_fs = ones(1,N_FS);


[pwr_n, f_n] = pwelch(NearField,wind_n,noverlap,N_N, ...
    fs_n,'power');
[pwr_hydrophone_long, f_f] = pwelch(FarField,wind_f,noverlap
   ,N_F,fs_f ...
    ,'power');
[pwr_hydrophone_short, f_fs] = pwelch(FarField_Short,wind_fs
   , ...
    noverlap,N_FS,fs_f,'power');

TrykkSensorDist = 1.206;

[pwr_hydrophone_BGN] = pwelch(FarField_BGN,wind_fs, ...
    noverlap,N_F,fs_f,'power');
[pwr_hydrophone_BGN_short] = pwelch(FarField_BGN_Short,
   wind_fs, ...
    noverlap,N_FS,fs_f,'power');

% psd_hydrophone_long = psd_hydrophone_long -
   psd_hydrophone_BGN;
% psd_hydrophone_short = psd_hydrophone_short -
   psd_hydrophone_BGN_short;

df_n = fs_n/N_N;
df_f = fs_f/N_F;
df_fs = fs_f/N_FS;


%20 lg because SPL
nearfieldSPL = 20*log10(sqrt(pwr_n*2)/10^-6) + 111.9 - 6;

farfieldSPL = 20*log10(sqrt(pwr_hydrophone_long*2)/10^-6)
%%
[power_corrected,spherical,absorp] = FarFieldModel_ampinput(
    ...
    sqrt(2*pwr_n),f_n,TrykkSensorDist ,Runs(run).CPA);
%Return corrected PSD values

URN = 20*log10(power_corrected ...
    /10^-6) + 111.9 - 6 ;
```

```
%10 log because of power, wav correction and rigig
   transducer correction

%%
figure(1)
semilogx(fn,nearfieldSPL)
hold on
semilogx(ff,farfieldSPL)
semilogx(fn,URN)
```

## A.10 SpectogramDTFT

```
load('Runs_wNearfield_timeseries.mat');
%%

run = 9;     % Runs between 8-12
Naerfelt = Runs(run).signal; %  Extracts data.

fs = 256000; %Sampling Frequency

nfft =80;     %Number for nfft and how many snippets.
res =1;       %Hz Resolution
fmin = 2400; % fmin and fmax is the dtft frequency band
   width.
fmax = 2520;
noverlap = round(fs/4); %Decides the overlap .
%Runs DTFT2. Output is Amplitudem, Frequency and Time
[Amp,fn,time] = DTFT(Naerfelt,nfft,fs,fmin,fmax,res,noverlap
   );
%%
AmpDB = 20*log10(abs(Amp/sqrt(2))/(10^-6));  %Calculate the
   DB value.

%Optional to find the highest mean amplitude in nearfield.
[maxamp,i] = maxk(mean(AmpDB),1);
%Calculates DopplerShift
[hydfreq,tdp] = Hastighettilskip(2454,time,Runs(run).CPA);
%% Makes Spectogram using pcolor.
figure();
pcolor(time,fn,abs(Amp'));
ylabel('Frequency [Hz]')
xlabel('Time [s]')
shading flat
colormap('jet')

hold on

```

```
% plot(hydfreq,'r','linewidth',2
% pause
tdp = tdp +15;
plot(tdp,hydfreq,'r','linewidth',2)
yline(2454,'linewidth',2)
```

## A.11 DopplerShift

```
function [freqfjernfelt,doptid] = Hastighettilskip(f,
   tidslengde,cpa)
dt = tidslengde(2)-tidslengde(1);
%t = tidslengde(1:floor(end/2));
%x = 205 - t * 0.514444*11/(t(2)-t(1));
%x = 205 - t *205/t(end);
x = abs(205 - tidslengde .* 410/84);
%Dette blir litt kæza siden tidsaxksen er weird
%x = [205 x fliplr(x(1:end-1))];
figure()
avs  = sqrt(cpa^2 + x.^2);
subplot(3,1,1)
plot(tidslengde(1:length(x)),avs)
xlabel('Time [s]')
ylabel('D [m]')
axis tight
subplot(3,1,2)
vd = -gradient(avs);
vd = vd/(dt);
plot(tidslengde(1:length(x)),vd)
xlabel('Time [s]')
ylabel('v_d [m/s]')
axis tight
c = 1500;
df = zeros(length(f),length(x));
for i = 1:length(x)
    df(i) = f * vd(i)/c;
end
freqfjernfelt = f + df;
subplot(3,1,3)
plot(tidslengde(1:length(x)),freqfjernfelt)
xlabel('Time [s]')
ylabel('f[Hz]')
axis tight

doptid = tidslengde(1:length(x));
end
```

## A.12 WaterfallforHarmonics

```
load('Runs_wNearfield_timeseries.mat');
%%
Run = 9;
hydrofon = Runs(Run).signal;
n = 5;
gf = 70;
f = 5:0.1:200;
Amp_Matrix = zeros(82,length(f));

for i = 1 : 82
    i
hydrofonshort = hydrofon(1*i*256000:1*i*256000+256000);
CPA = Runs(Run).CPA; %Closest Point of Approach.
fs = 256000;
noverlap = 0;
w = hanning(length(hydrofonshort));

[Power_avg_f, f] = pwelch(hydrofonshort,w,noverlap,f,fs,'
   power');

pDB_fs = 20*log10(sqrt(abs(Power_avg_f*2*2))/(10^-6));

Amp_Matrix(i,:) = sqrt(abs(Power_avg_f*2*2));
end
%%
figure(1)
subplot(2,1,1)

waterfall(f,(1:height(Amp_Matrix)),Amp_Matrix)
title(['Waterfall Plot of Predicted Harmonic Frecuency Band
   ' , ...
    num2str(f(1)),'-',num2str(f(end)),'Hz']);
colormap winter
set(gca,'CLim',[0 0.5]);
xlabel('[Hz]')
ylabel('[s]')
zlabel('[Pa]')
axis tight
x = gf*n;
xline(x,'LineWidth',2)
view(-2,65)
subplot(2,1,2)

waterfall(f,(1:height(Amp_Matrix)),Amp_Matrix)
title(['Time and Pressure Amplitude of ' ...
```

```
    ' Predicted Harmonic Frecuency Band ' ,num2str(f(1)),'-'
       ,num2str(f(end)),'Hz']);
xlabel('[Hz]')
ylabel('[s]')
zlabel('[Pa]')
view(90,0)
axis tight
% shading flat
% set(gca,'color',[0.7 0.7 0.7]);
```

## A.13 FinalComparison

```
%% The Data
load Runs_wNearfield_timeseries.mat
%% Run General

run = 11;
psens = 'P2';
NearField =Runs(run).p2;
FarField = Runs(run).signal;
FarField_BGN = Runs(7).signal;
FarField_BGN = FarField_BGN(1:length(FarField));

CPA = Runs(run).CPA;
fs_n  = 48000;
fs_f  = 256000;

noverlap = 0;
ns = 1;            %Number of sample periods.
time_ff = 40;      %Part of signal extraxted in second.

FarField_Short = FarField(fs_f*time_ff:fs_f*time_ff+ns*fs_f)
   ;
FarField_BGN_Short = FarField_BGN(1:length(FarField_Short));

c = 1491;
N_F  = length(FarField);
N_FS = length(FarField_Short);
N_N  = length(NearField);

% wind_n =  hanning(N_N);
% wind_f =  hanning(N_F);
% wind_fs = hanning(N_FS);

wind_n =  ones(1,N_N) ;
wind_f =  ones(1,N_F) ;
wind_fs = ones(1,N_FS);
```

```
35 TrykkSensorDist = 1.206;
36
37
38 [psd_n, f_n] = pwelch(NearField,wind_n,noverlap,N_N,fs_n,'
      psd');
39 [psd_hydrophone_long, f_f] = pwelch( ...
40     FarField,wind_f,noverlap,N_F,fs_f,'psd');
41 %[psd_hydrophone_short, f_fs] = pwelch(
42 % FarField_Short,wind_fs,noverlap,N_FS,fs_f,'psd');
43
44
45 [psd_hydrophone_BGN] = pwelch(FarField_BGN,wind_fs,noverlap,
      N_F,fs_f, ...
46     'psd');
47 [psd_hydrophone_BGN_short] = pwelch(FarField_BGN_Short, ...
48     wind_fs,noverlap,N_FS,fs_f,'psd');
49
50 % psd_hydrophone_long = psd_hydrophone_long -
      psd_hydrophone_BGN;
51 % psd_hydrophone_short = psd_hydrophone_short -
      psd_hydrophone_BGN_short;
52
53
54 psd_n = psd_n * (10^(20*log10(TrykkSensorDist)/10))
      /10^(6/10);
55
56 df_n = fs_n/N_N;
57 df_f = fs_f/N_F;
58 df_fs = fs_f/N_FS;
59
60
61
62 %%
63 [cf ,nearfield_psd_oct] = Oct_Band(psd_n,f_n,fs_n,N_N);
64 %Sum all power values inside bands (psd*df) for pressure
      values.
65
66 nearfield_psd_oct_dB = 10*log10(nearfield_psd_oct) + 111.3;
67 %10 lg because power.
68
69
70 binx = find(cf == 1):find( abs(cf - 25118) < 1);
71 %%
72 [psd_corrected,spherical,absorp] = FarField_psdinput( ...
73     psd_n,f_n,0,Runs(run).CPA); %Return corrected PSD values
74
75 [cf1,psd_corrected_oct] = Oct_Band(psd_corrected,f_n,fs_n,
      N_N);
```

```
76 %Sum all power values inside bands (psd*df)
77
78 psd_corrected_oct_dB = 10*log10(psd_corrected_oct) + 111.3 ;
79 %10 log because of power, wav correction and rigig
      transducer correction
80
81
82 %%
83 [cf2 ,farfield_psd_oct] = Oct_Band(psd_hydrophone_long,f_f,
      fs_f,N_F);
84 %Sum all power values inside bands (psd*df) for pressure
      values.
85
86 farfield_psd_oct_dB = 10*log10(farfield_psd_oct) - 5;
87 %10 lg because p
88
89
90 %[cf10 ,farfield_short_psd_oct] = Oct_Band(
      psd_hydrophone_short,
91 % f_fs,fs_f,N_FS); %Sum all power values inside bands (psd*
      df)
92 % for pressure values.
93
94 %farfield_short_psd_oct_dB = 10*log10(farfield_short
95 % _psd_oct);     %10 lg because p
96 %% Bureau Veritas
97 %Foreløpig bruker jeg bare CPA, men egentlig er det
      distansen mellom motor
98 %og propell.
99 D_Bv   = CPA;
100 TL_BV  = 19*log10(D_Bv);
101
102 loss_BV = 10^(TL_BV/10);
103
104 BV_psd_corrected = psd_n/(loss_BV);
105 [cf3 ,BV_psd_oct] = Oct_Band(BV_psd_corrected,f_n,fs_n,N_N);
106 BV_psd_corrected_dB = 10*log10(BV_psd_oct) + 111.3;
107
108 %% ISO 17208-1
109 %Transmission Loss Defined By ISO 17208-1
110
111 shipDraught = 5;
112 d_s = 0.7 * shipDraught;                                    %
      Source Depth
113 k = f_n * 2*pi/c;
114 kds = k.*d_s;
115
```

```
116 TL_ISO = -10*log10((2*(kds).^4+14*(kds).^2)./((kds).^4+2.*(
       kds).^2+14))
117  + 20*log10(CPA);
118 
119 loss_ISO =10.^(TL_ISO/10);
120 
121 ISO_psd_corrected = psd_n./(loss_ISO);
122 
123 [cf4 ,ISO_psd_oct] = Oct_Band(ISO_psd_corrected,f_n,fs_n,N_N
       );
124 
125 ISO_psd_corrected_dB = 10*log10(ISO_psd_oct) + 111.3;
126 
127 %% DNV
128 %Her brukes også CPA
129 D_dnv = CPA;
130 TL_dnv = 18*log10(D_dnv) ;
131 loss_DNV = 10.^(TL_dnv/10);
132 
133 
134 DNV_psd_corrected= psd_n/(loss_DNV);
135 [cf5 ,DNV_psd_oct] = Oct_Band(DNV_psd_corrected,f_n,fs_n,N_N
       );
136 DNV_psd_corrected_dB = 10*log10(DNV_psd_oct) + 111.3;
137 %% DNV Forenklet
138 
139 C_d = 20*log10(D_dnv);      %Distance Correction
140 %LLoyd Mirror Correction is different for different
       frequencies.
141 C_r = zeros(1,length(f_n));
142 freq_indx = @(f) floor(f*N_N/fs_n +1);
143 %Function that finds nearest frequency index.
144 freq_indx100 = freq_indx(100);
145 for i = 1: length(C_r)
146     if i <= freq_indx100
147         C_r(i) = 29 - 16 *log10(f_n(i));
148     else
149         C_r(i:end) = -3;
150         break
151     end
152 end
153 TL_DNV_f = - C_d + C_r + 6;
154 loss_DNV_f = 10.^(TL_DNV_f./10);
155 DNV_f = psd_n.*loss_DNV_f';
156 [cf5 ,DNV_f_psd_oct] = Oct_Band(DNV_f,f_n,fs_n,N_N);
157 DNV_f_psd_corrected_dB = 10*log10(DNV_f_psd_oct) + 111.3;
158 
159 %% Hydropod
```

```
r = CPA;
loss_Hydropod = 10^(20*log10(r)/10);
Hydropod = psd_n/(loss_Hydropod);
[cf6 ,Hydropod_psd_oct] = Oct_Band(Hydropod,f_n,fs_n,N_N);
Hydropod_psd_oct_dB = 10*log10(Hydropod_psd_oct) + 111.3;

%% Average and Max
 maxnearfield = max(nearfield_psd_oct_dB(binx))
 avgnearfield = mean(nearfield_psd_oct_dB(binx))
 maxfarfield = max(farfield_psd_oct_dB(binx))
 avgfarfield = mean(farfield_psd_oct_dB(binx))

%%
figure(3)
semilogx(cf(binx),nearfield_psd_oct_dB(binx),'o-','LineWidth
   ',1.5)
hold on

semilogx(cf(binx),farfield_psd_oct_dB(binx),'o-','LineWidth'
   ,1.5)
semilogx(cf(binx),psd_corrected_oct_dB(binx),'o-','LineWidth
   ',1.5)
semilogx(cf(binx),BV_psd_corrected_dB(binx),'o-','LineWidth'
   ,1.5 )
semilogx(cf(binx),ISO_psd_corrected_dB(binx),'o-','LineWidth
   ',1.5 )
semilogx(cf(binx),DNV_psd_corrected_dB(binx) ,'*m-','
   LineWidth' ...
    ,1.5,'MarkerSize',10)
semilogx(cf(binx),DNV_f_psd_corrected_dB(binx) ,'o-','
   LineWidth',1.5)
semilogx(cf(binx),Hydropod_psd_oct_dB(binx)  ,'o-','
   LineWidth',1.5)
l = legend('NearField','FarField','Proposed Model','BV','ISO
   ', ...
    'DNV','DNV_{Simp}','Hydropod');
l.FontSize = 16;
l.FontWeight = "bold";
title(['Comparison Average Power in Each 1/3 - Octave Band
   for Run '
num2str(run) ' For Pressure Sensor ' psens ])
xlabel('f [Hz]','FontWeight','bold')
ylabel(['\boldmath ${\bar{\Pi_B}}, \textbf{dB} \  \textbf{re
   }\ ' ...
    ' 1\ \textbf{W}$'],'Interpreter','latex','FontWeight','
       bold')
set(get(gca, 'XAxis'), 'FontWeight', 'bold');
set(get(gca, 'YAxis'), 'FontWeight', 'bold');
```

```
196 set(gca,'FontSize',22)
197
198 axis tight
199 hold off
```

## A.14 Octaveband3

```
1  function [fTO,sTO_dB] = Octaveband3(freq,spectrum_dB)
2
3
4      %First the db input values is transformed into regular
           values.
5      spectrum = 10.^(spectrum_dB/20);
6      %  Centerfrequencies
7          fref = [10, 12.5 16 20, 25 31.5 40, 50 63 80, 100
               125 160, ...
8              200 250 315, ...
9          400 500 630, 800 1000 1250, 1600 2000 2500, 3150
               4000 5000, ...
10         6300 8000 10000, 12500 16000 20000];
11     % Exact center freq.
12     ff = (1000).*((2^(1/3)).^[-20:13]);
13     a = sqrt(2^(1/3));
14     f_lower_bound = ff./a;
15     f_higher_bound = ff.*a;
16
17     %Defines the lower and upper bound pr octave band
18     ind1 = find (f_higher_bound>min(freq));  ind1 = ind1(1);
19     ind2 = find (f_lower_bound<max(freq));  ind2 = ind2(end)
           ;
20     ind3 = (ind1:ind2);
21
22     %Calculates the sum of the spectrum inside each octave
           band
23     for ci = 1:length(ind3)
24         ind4 = (freq>=f_lower_bound(ind3(ci)) & ...
25             freq<=f_higher_bound(ind3(ci)));
26         %sTO_dB(ci) = 10*log10(sum(spectrum(ind4).^2));
27         sTO_dB(ci) = 10*log10(mean(spectrum(ind4).^2));
28  %#ok<AGROW> %  1/3 octave value = RMS sum of spectrum
       inside 1/3
29  % octave band
30         fTO(ci) = fref(ind3(ci));
31 %#ok<AGROW> % valid central frequency   1/3 octave
32     end
33
34 end
```

## A.15 Absorption

```
function alpha = absorption_francois_garrison(f,S,D,T);

% Fancois & Garrison
% kHz,ppt,m,degC
% dB/km
% assumed: pH, sound speed according to NN

pH = 8.1;
theta = 273 + T;
c = 1412 + 3.21*T + 1.19*S + 0.0167*D;

A1 = 8.86./c*10^(0.78*pH - 5);  % dB / km kHz
P1 = 1;
f1 = 2.8*sqrt(S/35).*10.^(4-1245./theta); %kHz

A2 = 21.44*S./c.*(1 + 0.025*T); % dB / km kHz
P2 = 1 - 1.37e-4*D + 6.2e-9*D.^2;
f2 = 8.17*10.^(8-1990./theta)./(1 + 0.0018*(S-35)); % kHz

if T <= 20
    A3 = 4.937e-4 - 2.59e-5*T + 9.11e-7*T.^2 - 1.5e-8*T.^3;
       % dB / km kHz^2
else
    A3 = 3.964e-4 - 1.146e-5*T + 1.45e-7*T.^2 - 6.5e-10*T
       .^3; % dB / km kHz^2
end
P3 = 1 - 3.83e-5*D + 4.9e-10*D.^2;

alpha = A1.*P1.*f1.*f.^2./(f.^2 + f1.^2) + A2.*P2.*f2.*f
   .^2./(f.^2 + f2.^2) + A3.*P3*f.^2;
```

## A.16 SpeedofSound

```
d = 5;
d_km =d*0.001;


P = 99.5*(1-0.00263*cos(2*62))*d_km+0.239*(d_km)^2;
T = 11;
S = 33.11;
```

```
8 C = 1449.08 + 4.57*T*exp(-(T/86.9+(T/360)^2))+1.33*(S-35)*
    exp(-T/120)+0.1522*P*exp(T/1200+(S-35)/400) +1.46*(10^-5)
    *P^2*exp(-(T/20+(S-35)/10))
```

# Appendix B

# Remaining 1/3 - Octave Band Comparisons

## B.1 Run 9

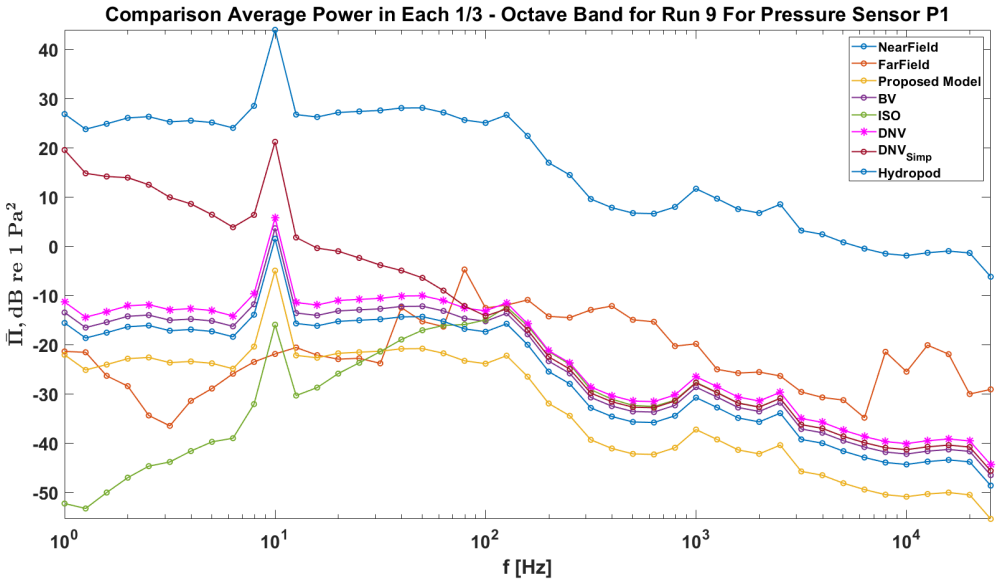


*Figure B.1: Comparison Average Power in Each 1/3 - Octave Band for Run 9 For Pressure Sensor P1*

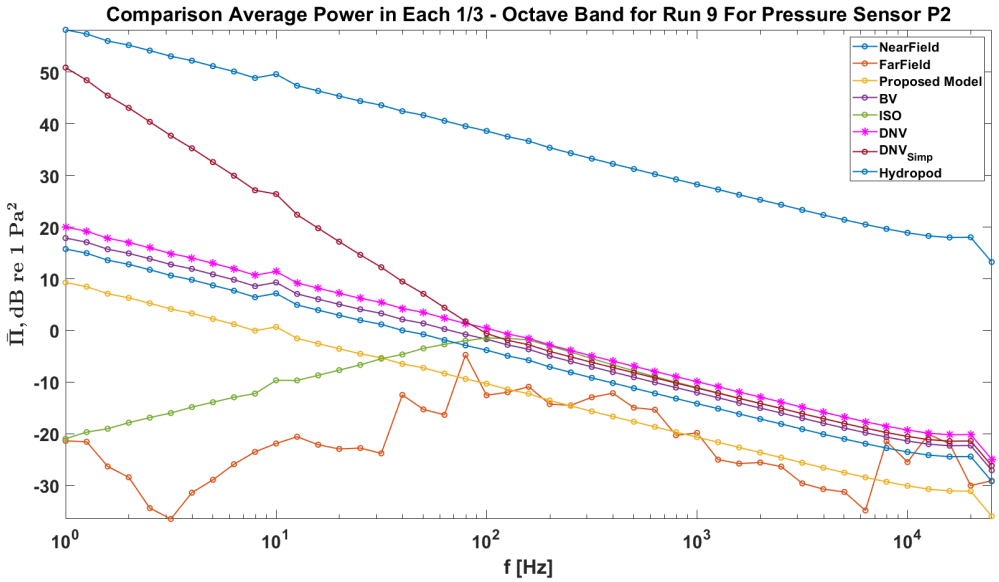


*Figure B.2: Comparison Average Power in Each 1/3 - Octave Band for Run 9 For Pressure Sensor P2*

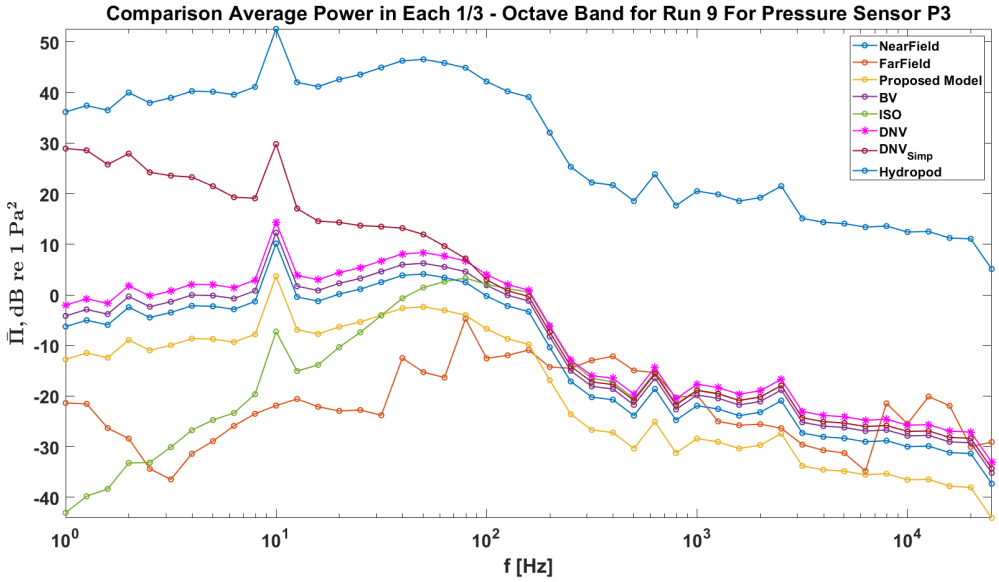


*Figure B.3: Comparison Average Power in Each 1/3 - Octave Band for Run 9 For Pressure Sensor P3*

# B.2 Run 10

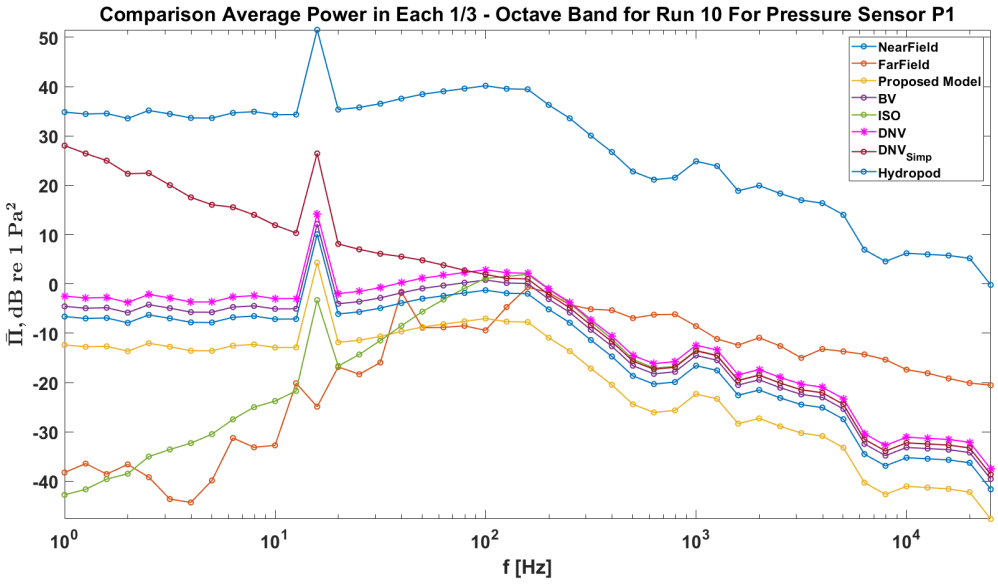


*Figure B.4: Comparison Average Power in Each 1/3 - Octave Band for Run 10 For Pressure Sensor P1*

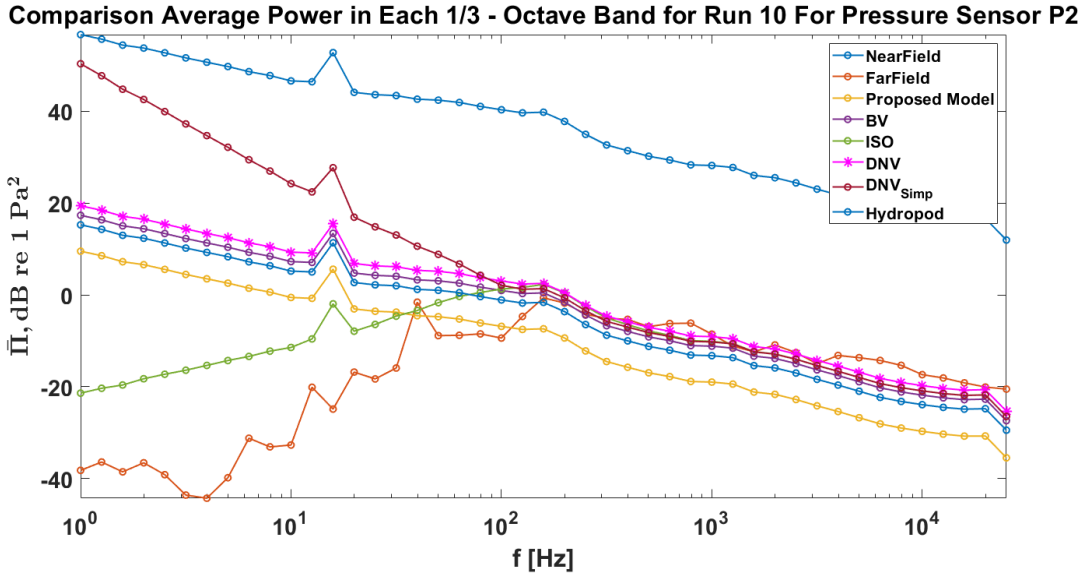


*Figure B.5: Comparison Average Power in Each 1/3 - Octave Band for Run 10 For Pressure Sensor P2*

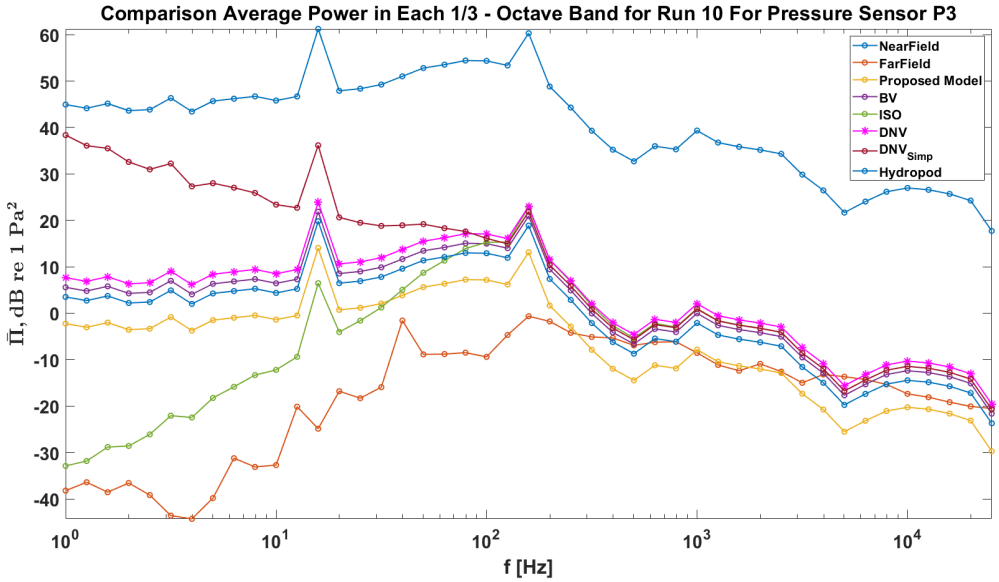


*Figure B.6: Comparison Average Power in Each 1/3 - Octave Band for Run 10 For Pressure Sensor P3*

# B.3 Run 11

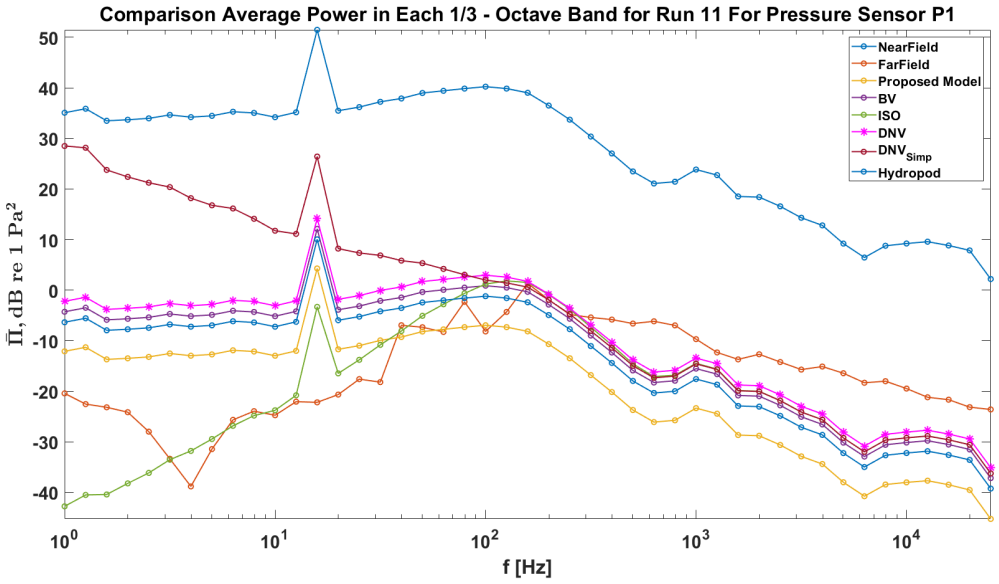


*Figure B.7: Comparison Average Power in Each 1/3 - Octave Band for Run 11 For Pressure Sensor P1*

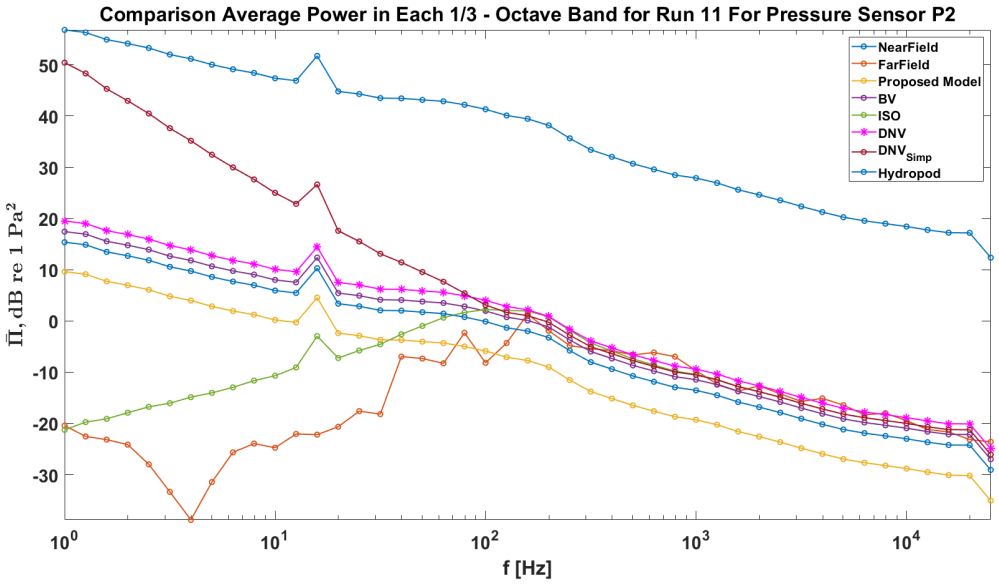


*Figure B.8: Comparison Average Power in Each 1/3 - Octave Band for Run 11 For Pressure Sensor P2*

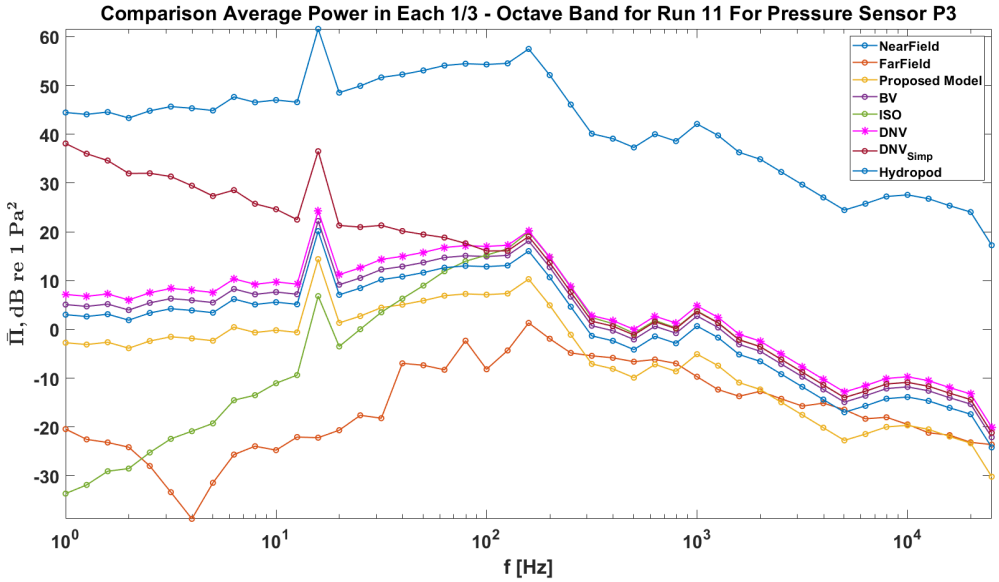


*Figure B.9: Comparison Average Power in Each 1/3 - Octave Band for Run 11 For Pressure Sensor P3*

# Appendix C

# Effect of Different Speed of Sounds.

In figure C.1 , figure C.3 and figure C.2 , it is seen how different sounds speeds affect the proposed calculated URN in different frequency bands.

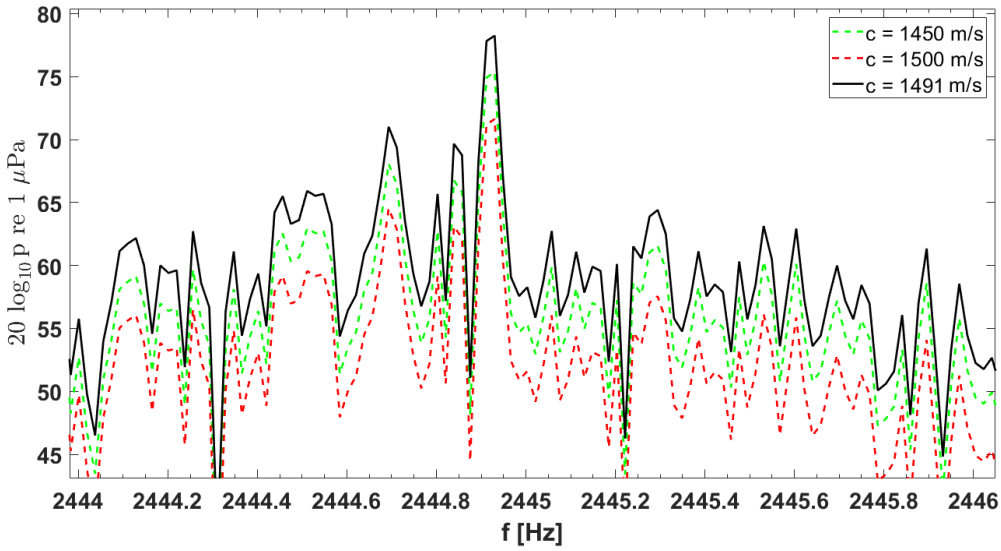


*Figure C.1: Different Sounds Speed for f = 2445 Hz*

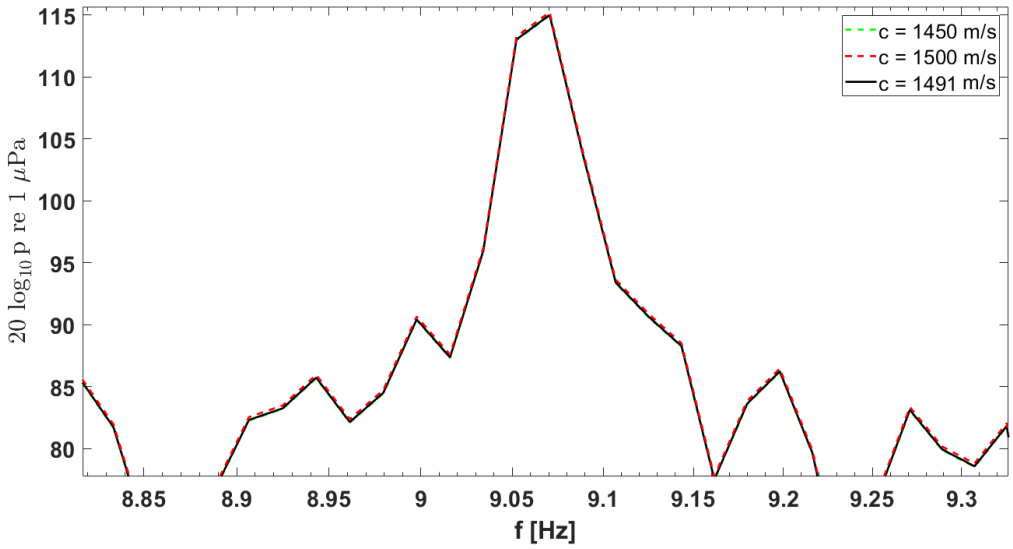


*Figure C.2: Different Sounds Speed for f = 9 Hz*

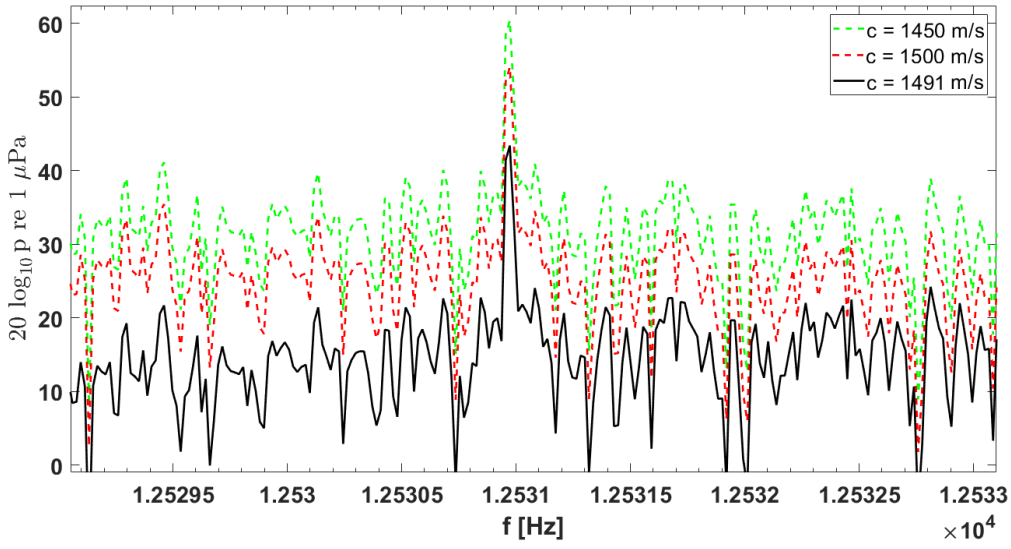


*Figure C.3: Different Sounds Speed for f = 12 kHz*